IChF
Institute of Physical Chemistry PAS

PhD thesis

Application of Fluorescence Correlation Spectroscopy to biology and medicine: structural studies of the biological matter

MARTA PILZ

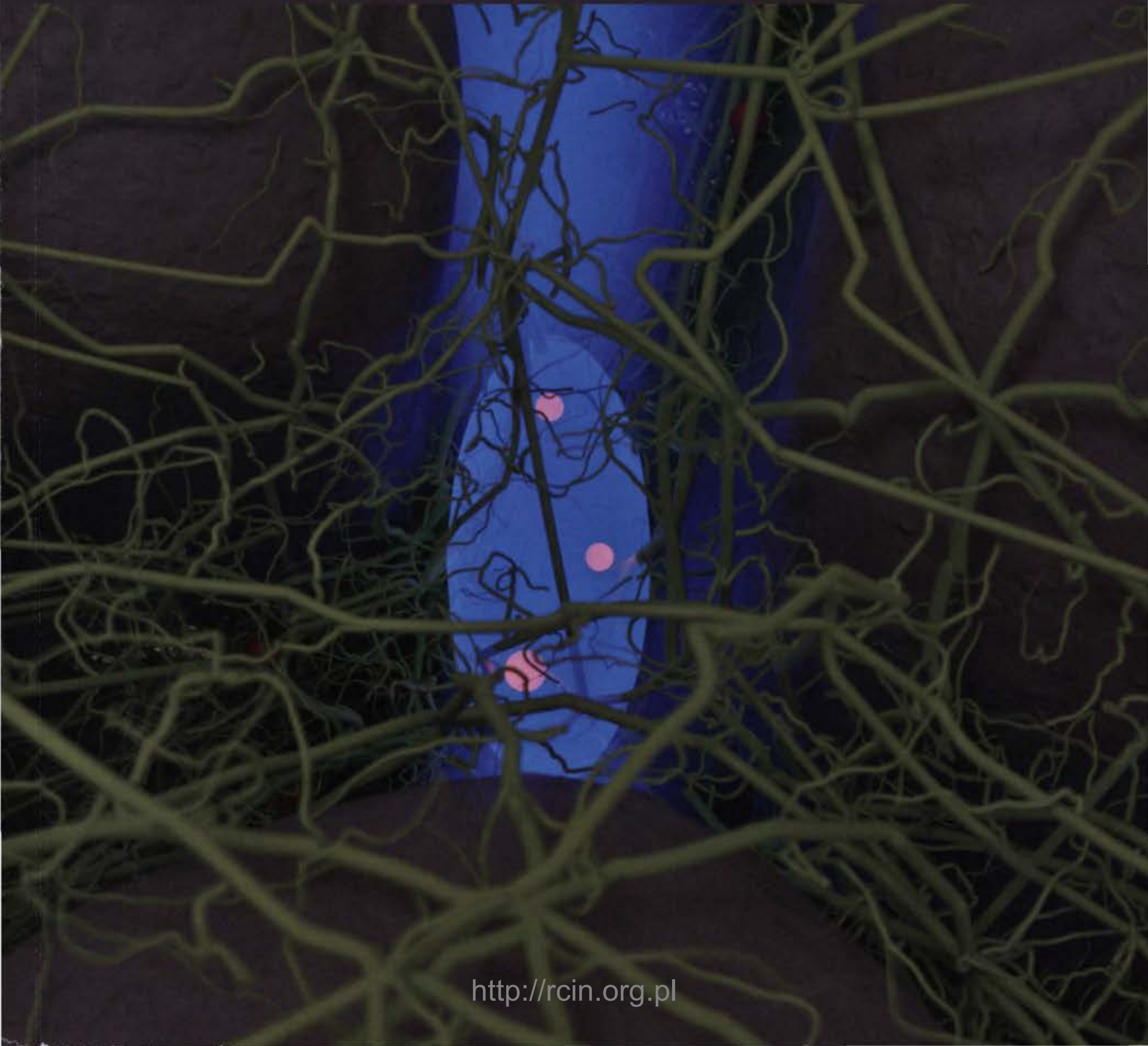

Application of Fluorescence Correlation Spectroscopy to biology and medicine: structural studies of the biological matter

PhD thesis by

Marta Pilz

prepared under supervision of

prof. dr hab. Robert Hołyst

and auxiliary supervision of

dr Karina Kwapiszewska

within the International PhD Studies at the

Institute of Physical Chemistry
of the Polish Academy of Sciences
Department of Soft Condensed Matter
Kasprzaka 44/52, 01-224 Warsaw

Warsaw, July 2021

Acknowledgements

Without the help and guidance of a few exceptional individuals for whom the impossible does not exist, I would never have gotten along my scientific path to this point.

First and foremost, I would like to express my gratitude to **prof. Robert Hołyst**, who was always available to help for all these years.

From the bottom of my heart, I would also like to say a big thank you to **dr Karina Kwapiszewska**, who always encouraged me to aim higher than I could imagine.

I also gratefully acknowledge **dr Tomasz Kalwarczyk** for his support with data analysis, especially in writing Python scripts, and for his assistance in dealing with equipment.

A special thank you goes out to all of my colleagues from the **Soft Matter Group**, **Laboratory of Microfabrication**, and **Microfluidics and Complex Fluids Research Group**, who have provided me with invaluable support during my PhD studies and have made this time of my life enjoyable and full of many memorable experiences.

I was extremely lucky to meet and work with such wonderful people.

This work was supported by

the National Science Centre
within the Maestro Grant 2016/22/A/ST4/00017

NATIONAL SCIENCE CENTRE
POLAND

and by the National Centre for Research and Development
within the Lider Grant LIDER/10/0033/L-9/17/NCBR/2018

The National Centre
for Research and Development

List of publications

Publications related to the thesis:

1. **Pilz M.**, Kwapiszewska K., Kalwarczyk T., Bubak G., Nowis D., Hołyst R. Transport of nanoprobes in multicellular spheroids. ***Nanoscale***, 2020, **12**, 19880-19887.

   The article has been selected by Professor Yves Dufrêne to feature in an Editor's Choice web collection focussing on **recent breakthroughs in nanobiotechnology**.

2. Jaworska K., Hering D., Mosieniak G., Bielak-Zmijewska A., **Pilz M.**, Konwerski M., Gasecka A., Kapłon-Cieślicka A., Filipiak K., Sikora E., Hołyst R., Ufnal M. TMA, A Forgotten Uremic Toxin, but Not TMAO, Is Involved in Cardiovascular Pathology. ***Toxins***, 2019, **11**, 490.

3. Konop M., Jaworska K., Bielinska K., Bielak-Zmijewska A., Mosieniak G., Sikora E., **Pilz M.**, Derzsi L., Sozański K., Hołyst R., Ufnal M. Abstract P3021: Trimethylamine but Not Trimethylamine N-Oxide Increases Blood Pressure in Rats, Affects Viability of Vascular Smooth Muscle Cells and Degrades Protein Structure. Hypertension, 2019, **74**, AP3021.

4. Karpińska A., **Pilz M.**, Buczkowska J., Żuk P., Kucharska K., Magiera G., Kwapiszewska K., Hołyst R. Interactions of anticancer drug olaparib with PARP1 (DNA repair protein) in living cells studied at a single-molecule level. 2021, submitted.

Other publications:

5. Gawrys-Kopczynska M., Konop M., Maksymiuk K., Kraszewska K., Derzsi L., Sozanski K., Hołyst R., **Pilz M.**, Samborowska E., Dobrowolski L., Jaworska K., Mogilnicka I., Ufnal M. TMAO, a seafood-derived molecule, produces diuresis and reduces mortality in heart failure rats. ***eLife***, 2020, **9**, e57028.

6. Kucharska K., **Pilz M.**, Bielec K., Kalwarczyk T., Kuźma P., Hołyst R. Two intercalation mechanisms of oxazole yellow dimer (YOYO-1) into DNA. ***Molecules***, 2021, **26**, 3748.

Patents:

1. **Pilz M.**, Nalin F., Kwapiszewska K., Makuch K., Derzsi L., Hołyst R. *Układ mikroprzepływowy oraz sposób pomiaru wnikania cząstek do komórek adherentnych.* 2021, with attorney.

Abstract

A close connection exists between the structure of biological matter (e.g. biomolecules, cells, and tissues) and their function. Structural studies can hardly be overestimated as they influence all aspects of biology (and medicine), from understanding fundamental cellular processes to the development of therapeutic agents.

Nowadays, numerous advanced methods and approaches are applied to determine structures. My thesis presents that a spatial architecture can be revealed, quite unobvious, by analysing the molecules' motion. Studying the processes associated with changes in the mobility of the molecules gave me insight into their structure or the architecture of the microenvironment in which they diffuse. The diffusion was examined by fluorescence correlation spectroscopy (FCS). FCS is a method of analysing the fluctuations in the fluorescence signal from a small detection volume, providing quantitative information about, e.g. the diffusion properties, concentration, and interactions of analytes. A wealth of information is gained from these parameters, which I used to determine the structure of biological matter with varying complexity levels, as I demonstrated in the following examples:

1. Proteins (chapter 3). Measuring the diffusion of proteins can reveal factors influencing their conformation and, as a result, identify agents which can be treated as disease markers. Using the example of trimethylamine, I showed that it is a factor causing protein degradation. Since proteins play a central role in virtually all biological processes, defining the disturbing effect of factors on proteins can explain their toxic effect on humans.

2. The cytoplasm of cells cultured in a tissue-like architecture (chapter 4). I established a procedure for FCS measurements inside the cells in a three-dimensional tissue model. Based on the mobility measurements, I determined cytoplasmic viscosity, an essential structural parameter that governs intracellular reaction rates and strongly affects intracellular transport. Furthermore, by using FCS inside cells in a tissue model, I demonstrated the increased accumulation of olaparib, an anticancer drug, compared to adherent cells. As a result, I noted some differences in the intracellular structure between cells cultured on the flat surface and tissue-like architecture.

3. The extracellular matrix (ECM) within tumour models (chapter 5). I proved that FCS is a method that permits exploring the tumour environment – its extracellular space. The application of FCS provided information about the architecture of the main physical barrier that inhibits the penetration of anticancer drugs into the tissue and, consequently, their effectiveness. The study of vary-sizing nanoprobes mobility in the ECM has led to the discovery of the length-dependent viscosity of the ECM. As a result, the probes with a radius of up to 10 nm freely diffuse in the complex network of the extracellular areas - a few times faster than it would appear from the Stokes-Einstein relation.

The presented applications of FCS, first and foremost, prove that FCS is a powerful tool that enables the probing of complex systems in terms of their structural studies, revealing valuable information in biological or medical research.

Streszczenie

Struktura układów biologicznych (np. biomolekuł, komórek, tkanek) ściśle oddziałuje na ich funkcjonalność. Stąd badania strukturalne wpływają na wszystkie aspekty biologii (oraz medycyny) - od zrozumienia podstawowych procesów komórkowych po opracowanie środków terapeutycznych. Istnieje wiele metod wykorzystywanych do badań strukturalnych. W mojej pracy pokazuję, że architekturę przestrzenną można wyznaczyć, dość nieintuicyjnie, analizując ruch molekuł. Charakteryzując mobilność cząsteczek mogę opisać ich strukturę lub środowisko, w którym się poruszają. Do badania mobilności molekuł zastosowałam spektroskopię korelacji fluorescencji (ang. *fluorescence correlation spectroscopy*, FCS). FCS jest metodą, która opiera się na analizie fluktuacji sygnału fluorescencyjnego pochodzącego z bardzo małej objętości detekcji, dostarczającą informacji ilościowych o m. in. dyfuzji, stężeniu i oddziaływaniach analitów. Otrzymywane parametry za pomocą FCS wykorzystałam do określenia struktury materii biologicznej o różnym stopniu złożoności, co pokazałam na poniższych przykładach:

1. Białka (rozdział 3). Pomiar dyfuzji białek może ujawnić czynniki, które wpływają negatywnie na ich konformację, a w rezultacie określić je jako markery chorób. Na przykładzie trimetyloaminy pokazałam, że jest czynnikiem degradującym białka. Ponieważ białka odgrywają kluczową rolę w praktycznie wszystkich procesach biologicznych, określenie czynników zaburzających strukturę białek może wyjaśnić ich toksyczny efekt na organizm człowieka.

2. Cytoplazma komórek w trójwymiarowych hodowlach, stanowiących model tkanki (rozdział 4). Opracowana przeze mnie procedura pomiarów FCS wewnątrz komórek w trójwymiarowym modelu tkanki

umożliwiła wyznaczenie lepkości cytoplazmy, która jest kluczowym parametrem strukturalnym kontrolującym szybkość reakcji wewnątrzkomórkowych oraz proces transportu we wnętrzu komórki. Ponadto, stosując FCS w komórkach modelu tkankowego wykazałam zwiększone stężenie olaparibu (leku przeciwnowotworowego) w porównaniu do komórek hodowanych na podłożu płaskim. Rezultatem moich prac jest wskazanie kilku różnic w strukturze wewnątrzkomórkowej pomiędzy komórkami adherentnymi a komórkami w architekturze tkankowej.

3. Macierz zewnątrzkomórkowa (ang. *extracellular matrix*, ECM) w modelach guzów nowotworowych (rozdział 5). Udowodniłam, że FCS jest metodą pozwalającą na badanie środowiska guza - jego przestrzeni pozakomórkowych. Zastosowanie FCS do badań ECM dostarczyło informacji na temat struktury głównej bariery fizycznej, hamującej wnikanie leków przeciwnowotworowych do tkanek, a w konsekwencji ich skuteczności. Badanie mobilności próbników o różnej wielkości w ECM doprowadziło do odkrycia lepkości macierzy zależnej od skali, przez co cząsteczki o promieniu do 10 nm niemal nie odczuwają lepkości macierzy zewnątrzkomórkowej i poruszają się kilka razy szybciej niż wynikałoby to z równania Stokesa-Einsteina.

Przedstawione zastosowania FCS przede wszystkim dowodzą, że metoda ta jest potężnym narzędziem, umożliwiającym badanie struktury złożonych układów, dostarczając cennych informacji w badaniach biologicznych czy medycznych.

Contents

Appendices

1

Introduction

All living organisms, even the simplest ones, have a hierarchical structure. This hierarchical organization can be remarked on many scales. In humans, biomolecules join together to form cellular components, and next, organelles constitute cells, which self-assemble into tissues - building blocks of organs. The result is a body. The consequence of a hierarchical organization is that the disturbance in basic units affects the functioning of the entire organism. By studying particular biological systems (i.e. biomolecules, cells, tissues), we can comprehend the processes responsible for the function of living organisms as a whole.

The application of nanoscale techniques for analysing biological system is instrumental in progress in biology and medicine. Probing biosystems provides details on macromolecules structure and function. Structural studies can hardly be overestimated as they influence all aspects of biology, from the understanding of fundamental cellular processes to the development of therapeutic agents.

In the present work, I demonstrate the potential of fluorescence correlation spectroscopy (FCS) in structural studies of biological matter.

More precisely, I focus my research on examine the structure of proteins, intracellular and extracellular spaces within three-dimensional cell cultures.

Conformation of protein

Proteins are the most universal nanosized molecules in living systems and play a central role in virtually all biological processes. The function of protein is determined by its structure. The conformational changes in the process of denaturation or degradation rapidly lead to loss of protein functionality. Monitoring the structural changes of protein exposed to harmful factors can offer insight into the molecular mechanism of toxicity.

One of the compounds of which the mechanism of toxicity was obscure is trimethylamine-N-oxide (TMAO). Nevertheless, the lack of a toxicity mechanism did not prevent TMAO from being identified as a marker and mediator of cardiovascular diseases [1]. Some clinical studies have shown that increased levels of TMAO in plasma are associated with an increased risk of adverse cardiovascular events. Noteworthy, the role of trimethylamine (TMA), the precursor of TMAO, has not called attention in cardiovascular studies [2–4]. Only a multilevel, comparative analysis of the effects exerted by TMA and TMAO has emerged which of them is toxic [5].

The role of FCS in the study on the effects of TMA and TMAO was to assess the impact of their exposition on proteins structure. The use of correlation technique allowed, with a sub-nanometer resolution, for following the changes in proteins size exposed to TMA and TMAO.

Structure of intracellular and extracellular spaces within 3D cell cultures

The *in vitro* cell cultures are extensively used in medical, biochemical and molecular research, and most importantly, they provide easy access to biological material. Cells are usually grown as a monolayer of cells on a flat surface in the presence of a culture medium. Despite being an excellent research material, such two-dimensional cell culture creates many limitations as a tissue model. In response to these limitations, numerous methods of three-dimensional cell culture have been developed [6, 7]. One of the significant differences observed when comparing cells in 2D and 3D cell cultures is cell morphology. Cells have flat or three-dimensional shape, as shown in Fig. 1.1. The clear morphological difference raises the question: is the internal cell structure in two types of culture also so distinct?

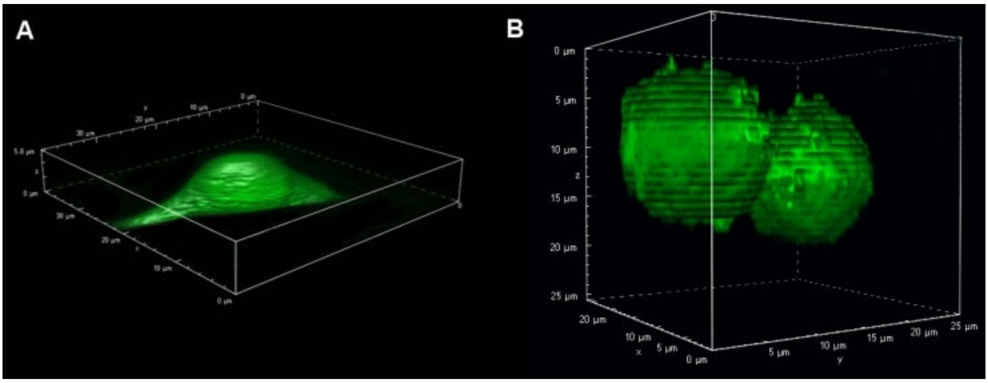

Figure 1.1: The confocal images of HeLa cells with GFP expression in (A) two-dimensional and (B) three-dimensional cell culture. The excitation wavelength was 488 nm.

To address this question, I applied fluorescence correlation spectroscopy to probe the cytoplasm of cells within 3D culture and compare with the results obtained for cells cultured as monolayer [8]. This comparative analysis I supported with high-resolution confocal imaging.

The 3D cell cultures, contrary to a monolayer of cells, produce the extracellular matrix (ECM) - a main physical barrier that inhibits the penetration of the anticancer drug into the tissue and, consequently, their effectiveness [9]. My mobility studies [10] of nanoprobes in the ECM provide insight into the impact of the tumour environment architecture on extracellular transport. Thereby, as a first, I have provided the description of the nanostructure of extracellular spaces.

The outcome of the study on extracellular transport can be used for an advanced modelling of drug administration through tissues.

2

Fluorescence Correlation Spectroscopy

Contents

Fluorescence correlation spectroscopy (FCS) is a non-invasive method that I applied to explore biomolecules' motion in systems of increasing complexity, ranging from solutions, live cells, and tissues. Studying the process associated with changes in the mobility of the molecules gave me insight into their structure or the architecture of the microenvironment in which they diffuse. Understanding my research outcomes is not possible without prior knowledge of the FCS method's basis, which I am introducing in this chapter.

2.1 Fluorescence Correlation Spectroscopy

Fluorescence correlation spectroscopy is a method of analysing the fluctuations in the fluorescence signal. These signal variations result from molecular processes such as particle movements, molecule conformational changes, and chemical or photophysical reactions. FCS quantifies those processes and provides single molecule sensitivity since it is based on fluorescence detection.

Fluorescence

Electromagnetic radiation interacts with matter during propagation through it, and its study is known as spectroscopy.
After the absorption of light, molecules use several different pathways to lose the absorbed energy and return to the ground state. The two primary mechanisms for the loss of excess energy are the non-radiative and radiative transfer of energy to the environment. Non-radiative energy transfer occurs by the collisions of molecules. After a certain time at an excited electronic level, the radial mechanism occurs when a molecule emits the absorbed photon. This light emission phenomenon is called luminescence, which is divided into two categories, fluorescence and phosphorescence, depending on the nature of the excited state. Fluorescence occurs within nanoseconds after the absorption of light that is typical of a shorter wavelength. The difference between the exciting and emitted wavelengths is known as the Stokes shift. This phenomenon makes it possible to distinguish between absorption and emission of light. By completely filtering out the exciting light without blocking the emitted fluorescence, it is possible to detect only fluorescence.
A helpful approach to understanding the absorption and emission process is depicted in the Jablonski diagram (Fig. 2.1) [11, 12].

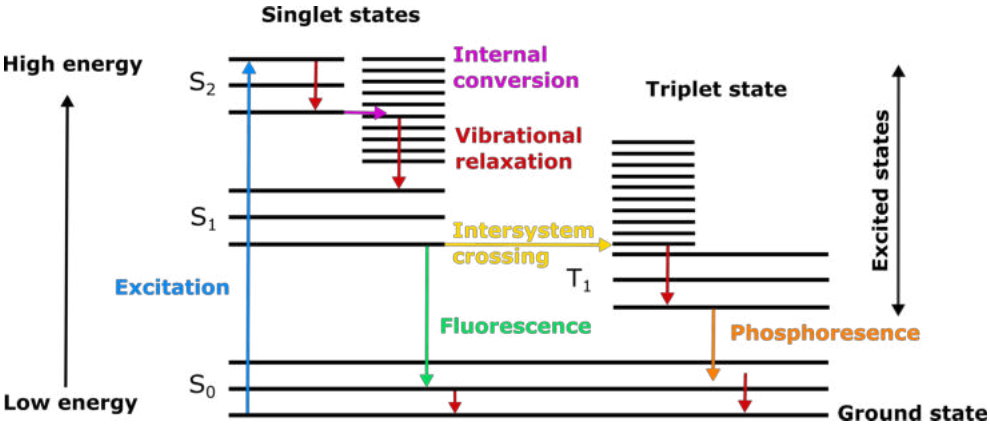

Figure 2.1: The Jablonski diagram illustrates the energy states of a molecule along with the radiative and non-radiative transitions that can occur between them. Based on [11].

However, how does fluorescence lead to obtaining measurable parameters such as diffusion coefficient or concentration?

Correlation

The principle of FCS is based on measuring the fluctuation of fluorescence inside the definite detection volume. The fluorescence photons are recorded by the ultrasensitive detector and processed by the correlator. The correlator unit computes the correlation function. The autocorrelation function describes the probability of detecting a photon from the molecule at a given time τ if a photon is detected from the same molecule at time zero. The decay of the correlation can be related to diffusion or chemical reaction.

Consider the process of diffusion. The diffusion of a fluorescent molecule into or out of the detection volume will generate intensity fluctuations, $I(t)$, as shown in Fig. 2.2. The average timescale of the fluctuation depends on the time a molecule needs to cross the detection volume, called diffusion time τ_D. On timescales shorter than or equal to τ_D, there is a high probability of detecting photons coming from one molecule, and the fluorescence signal remains similar (is highly correlated). On longer timescales, molecules can leave the detection volume, and the probability of detecting the fluorescence decreases and the correlation is completely lost. As a result, the correlation function decays at times longer than τ_D [13, 14].

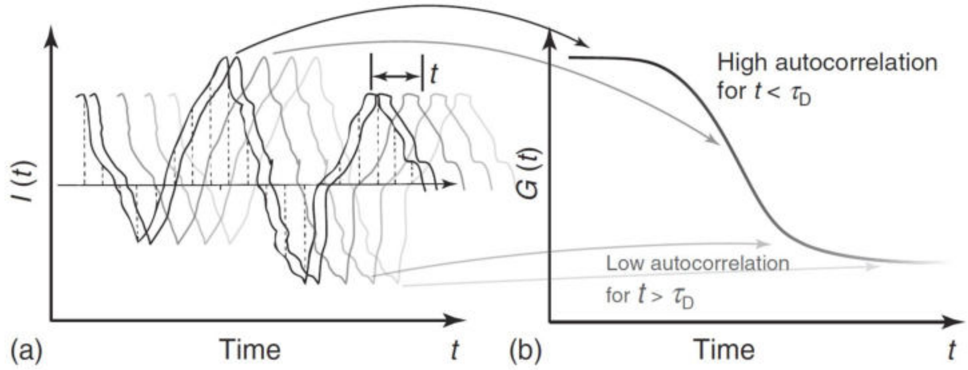

Figure 2.2: Determination of the autocorrelation function. (a) Schematic signal of the fluorescence fluctuation around the mean value (marked with the horizontal line) and (b) the resulting autocorrelation function [14].

Summarising, fluorescence correlation spectroscopy is based on the measurement and correlation analysis of fluorescence intensity fluctuations. It sounds inconspicuous, but the advanced technology used in the FCS makes it a single-molecule technique.

2.2 Experimental realization

Because of the coupling of a confocal microscope system with a single photon detector and a stable light source, the FCS gained single molecule sensitivity.

Confocal microscope system

The confocal microscope provides one of the smallest detection volumes in optics through the application of a pinhole. The pinhole excludes the fluorescence generated outside of the focal plane, as is shown in Fig. 2.3.

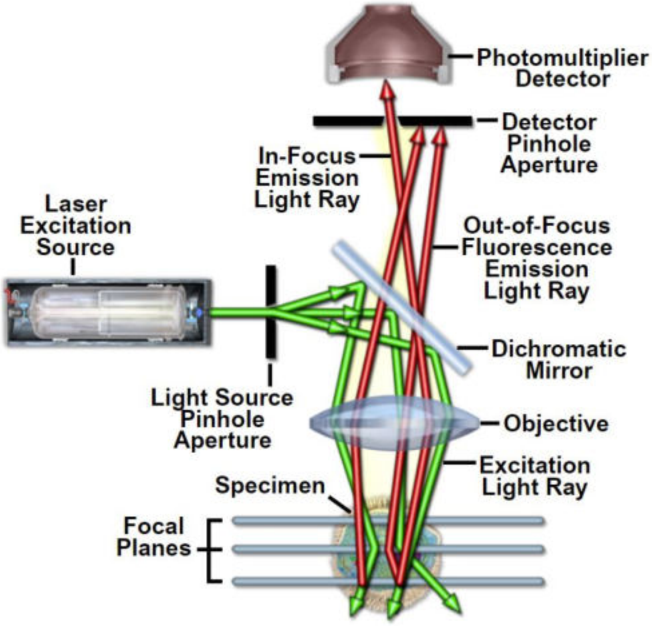

Figure 2.3: A scheme of light pathways in confocal microscopy. A pinhole reduces out of focus light and is responsible for spatial resolution. Another essential element of the confocal microscope is the dichroic mirror, which separates the fluorescence signal (red) from the excitation light (green) [15].

The presence of focal volume in the FCS set-up allows for fluorescence detection from a volume in the order of femtoliters. The signal from FCS is inversely proportional to the number of fluorescent molecules in the observation volume. Hence, a small detection volume increases the signal amplitude and enables performance measurements even at the fluorophore's picomolar concentration. The amplitude of fluctuations relative to the average signal will decrease as the molecule's concentration rises. Thus, the FCS has a maximum concentration regime above which there is not a sufficiently strong fluctuation in the fluorescence signal. Consequently, FCS works within a limited concentration range: from picomolar up to a sub-micromolar concentration [13, 16].

Moreover, the application of a confocal system in an FCS set-up enables using the imaging mode of a microscope, which allows for the precise location of the confocal volume inside a specific point of a sample, e.g. in the cytoplasm of a living cell. Nonetheless, without an extremely sensitive detection technique, the study of individual macromolecules in their native environment [17] would be impossible.

Single photon detector

The FCS set-up utilises a time-correlated single-photon counting (TCSPC) system. By definition, it uses only a single quanta of light, and, therefore, it matches the requirements of an application where the fluorescence signal is faint. The TCSPC system includes a silicon single-photon avalanche diode (SPAD) detector. The operation of the SPAD detector is based on the internal photoelectric effect. The detector features an excellent photon detection efficiency of up to 48% at 550 nm wavelength and picosecond timing resolution.

TCSPC collects photon arrival times - the delay between excitation and emission, and enables fluorescence lifetime correlation spectroscopy (FLCS) measurements. For this purpose, pulse excitation is needed with a pulse shorter than 200 ps [13, 18].

Laser

The excitation light is compulsory to obtain a fluorescence signal. The laser must meet a fundamental requirement: the light source must have stable power and frequency. The fluctuations arising from varying laser illumination will affect the outcome of the FCS experiments.

Additionally, application of a pulsed laser instead of continuous reduces the photobleaching, which causes a deviation in the correlation signal [13, 16].

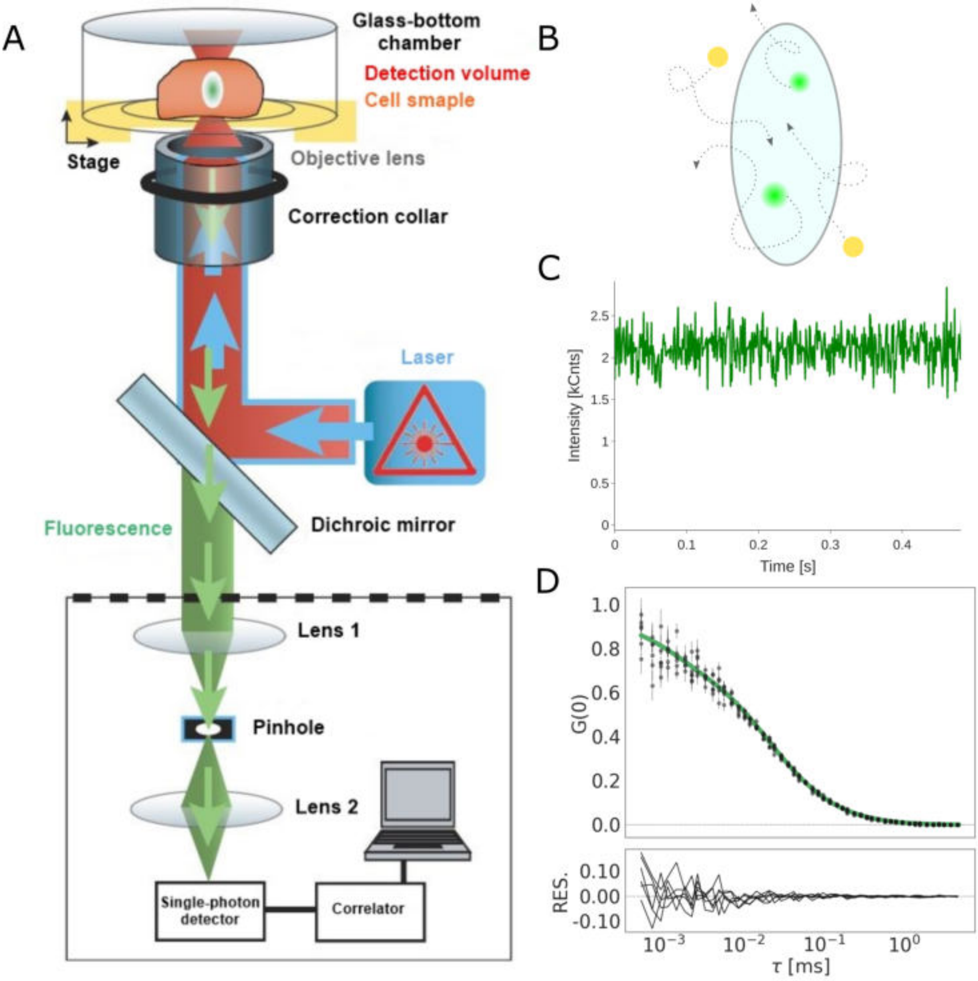

Figure 2.4: A scheme of FCS set-up [19] (A) and the basic concepts of FCS (B-D). (A) The emission light, excited in the detection volume, is collected via an objective lens. Then, it passes through the dichroic mirror, reduced by a pinhole and recorded by an ultrasensitive detector. (B) Diffusing molecules through the confocal volume gives rise to fluorescence fluctuations (C), from which the autocorrelation function is calculated (D).

A brief introduction to the basic principles of FCS together with the aforementioned essential components of the FCS system (Fig. 2.4) facilitates understanding the work of the technique. However, the potential of FCS can be found in an ever-increasing number of autocorrelation function models, which have made FCS suitable for a wide range of applications.

2.3 Theoretical concepts

As was already mentioned, FCS analysis is performed using the autocorrelation function (ACF) - the experiment measures the correlation of fluorescence intensity fluctuations over time. Correlation is an averaging process, so even if a signal from one molecule is crucial to generating fluctuations, a correlation curve does not provide information about a particular molecule, but only about the ensemble average.
The analytical form of the autocorrelation function $G(t)$ for a certain time lag t derived from one fraction of diffusing molecules is [20]:

$$G(t) = \left(1 + \frac{T}{1-T} \cdot e^{-t/\tau_T}\right)\left(\frac{1}{N}\right)\frac{1}{\left(1+\left(\frac{t}{\tau_d}\right)^{\alpha}\right)\left(1+\frac{1}{\kappa^2}\left(\frac{t}{\tau_d}\right)^{\alpha}\right)^{1/2}} \tag{2.1}$$

wherein T is the amplitude of the triplet component, τ_T is the triplet state decay time, N corresponds to the average number of fluorescent particles within the confocal volume, τ_d is translational diffusion time, α is anomality parameter, and κ is beam waist ratio - a parameter describing the shape of detection volume determined during the calibration procedure.
When in the probed volume, there are several types of diffusing objects (e.g. free fluorescent dye and protein labelled with dye or free fluorescent drug and drug bounded to a target) - the multicomponent diffusion autocorrelation function takes the following form:

$$G(t) = \left(1 + \frac{T}{1-T} \cdot e^{-t/\tau_T}\right)\left(\frac{1}{N}\right)\sum_{i=1}^{n}\frac{A_i}{\left(1+\left(\frac{t}{\tau_{d_i}}\right)\right)\left(1+\frac{1}{\kappa^2}\left(\frac{t}{\tau_{d_i}}\right)\right)^{1/2}} \tag{2.2}$$

wherein A_i is the fraction of the i-th component, n is the number of diffusion species ($n = 2$ in the case of free fluorescent dye and protein labelled with dye), and τ_{d_i} is translational diffusion time of the i-th component.

A two-component diffusion model is an excellent tool for studying binding interactions. Free, fast diffusing dye, upon binding to a much larger molecule, will diffuse significantly slower. The fractions of the fast and slow diffusing components correspond to the fractions of free and bound molecules. The diffusion coefficients, as well as their radius, are calculated by the following analysis.

The terms of expression 2.1 and 2.2 are used to extract from fitted value, e.g. the diffusion coefficient. Knowing the value of the semi-minor axis of the confocal volume ω_0 ($\kappa = z_0/\omega_0$, please see Fig. 2.5), the diffusion coefficient is calculated from the following formula:

$$D = \frac{\omega_0^2}{4\tau_d} \tag{2.3}$$

where τ_d is the translational diffusion time derived from the autocorrelation function (Eq. 2.1).

The diffusion coefficient, D of molecule is inversely proportional to its radius r, as it results from the Stokes-Einstein relation [21]:

$$r = \frac{kT}{6\pi\eta D} \tag{2.4}$$

where k is Boltzmann constant, T is temperature, and η stands to viscosity.

It is essential to understand the meaning of the diffusion time obtained from the autocorrelation function.

The diffusion coefficient is a molecular property and does not depend on any instrumental parameters. Since τ_d depends on D, it can be considered that diffusion time is also a molecular parameter and independent of the instrument. However, the diffusion time depends on the confocal volume axis. This means that to determine the absolute value of the diffusion coefficient, there is a necessity for exact knowledge of the shape of the confocal volume. For this reason, FCS systems are calibrated by measuring the diffusion time of molecules with a well-known diffusion coefficient.

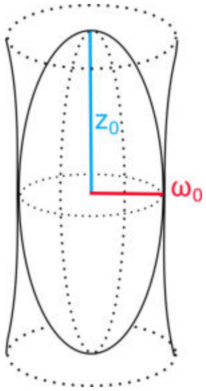

Figure 2.5: Ellipsoidal shape of confocal volume. The volume is characterized by parameters z_0 and ω_0.

The knowledge about the efficient detection volume (from the FCS calibration procedure) and the number of fluorescent molecules, N, present in the detection volume (readout parameter of the fit, Eq. 2.1 or 2.2) allows the concentration of fluorescent particles in the sample to be determined:

$$c = \frac{N_A V_0}{N} = \frac{N_A \pi^{3/2} \omega_0 z_0}{N} \tag{2.5}$$

where N_A is Avogadro constant and V_0 is efficient detection volume.

So far, I presented that FCS analysis can deliver a large number of system properties. Starting from the diffusion coefficient and size of studied molecules to viscosity, binding interaction, and concentration of fluorescent particles. Besides those structural parameters, the FCS experiments reveal the reaction rates.

Altogether, the broad range of determined parameters and the sensitivity have made FCS suitable for an ample scope of applications.

2.4 FCS in biological application

In FCS, the confocal volume is in the order of femtoliters. Such a tiny detection volume is particularly advantageous for the study of small systems such as living cells. FCS application in cells enables the measurement of molecular interactions at physiological concentration and in a native environment. Because of those attractive features, FCS experiments have already been performed in many of the cellular components, such as the nucleus, the cytoplasm and also the cell membrane [22, 23].

Structural studies

Fluorescence correlation spectroscopy is an established tool for conformational studies of biomolecules. There are, in principle, two types of application of FCS in protein biophysics. Foremost, the diffusion coefficient and hence the hydrodynamic radius of a protein can be determined precisely. Second, FCS can be utilized to detect protein folding intermediates in the unfolding pathway or to study their conformational dynamics [24, 25].

Moreover, the application of FCS has been extended to examine protein aggregation and protein-protein interaction. Most importantly, all studies of proteins using FCS can be done in a solution, or in their native cellular environment [26, 27].

The FCS analysis of molecular diffusion extracts information about the structures, which is not readily available through more direct methods. The intracellular mobility studies of nanoprobes using FCS revealed the nanostructure of the cell's cytoplasm and nucleus [8, 28].

Probing the cytoplasm by varying sized molecules gave insight into its gel-like structure of the mesh size ∼100 nm filled with a liquid phase. Whereas probing the nucleus with nanoparticles proved its ∼150 nm wide interchromosomal channels filled with the diluted protein solution.

Molecular interactions

The FCS study of intermolecular interactions uses the differences in mobility between free and bound molecules. The complex formation manifests itself in FCS measurements as a significant decrease in the diffusion coefficient value. This dependence is used to research protein-protein interaction, binding drugs to their targets, and protein oligomerization studies [17].
Moreover, FCS employed inside living cells gives insight into the interaction of macromolecules in their native environment. Examining the interaction of molecules in the cytoplasm can produce radically different outcomes than *in vitro* [29].

Transport

As I have already mentioned, the most apparent use of FCS measures molecules mobility, even inside living cells. Research utilising FCS in cellular transport can measure the motility of biomolecules within precisely located cellular regions with the distinction between diffusion and active transport. Studies on transport not only assess the rate of biological processes but also its dependence on location, providing a much more accurate and quantitative image of molecular mechanisms [30].

The examples I have mentioned above present the potential of fluorescence correlation spectroscopy as a tool with broad applicability to life sciences. However, FCS, like every other technique, is not free from limitations.

2.5 Limitation of FCS

FCS not only works in a concentration regime, but also in a time regime. FCS is applied to measure the diffusion time of molecules through a confocal volume - a microsecond process. The lower limit of the FCS

timescales is limited (apart from the capabilities of electronic detectors) by the quantum nature of the fluorescent molecule, i.e. by the time of the excitation process and subsequent photon emission - in the range of nanoseconds [13].
Another troublesome feature of the method is related to the data analysis. The interpretation of autocorrelation curves is usually challenging because it necessitates prior knowledge of the examined system in order to choose an appropriate model [20]. Furthermore, it may turn out that an analytical formula for autocorrelation analysis of the studied system necessitates a modification or utterly new form.

Technical issues

There are also diverse factors that are not so much limiting as they interfere with the correct measurements and, consequently, data analysis. Since the quantitative FCS experiments rely on the calibration of the detection volume, the calibration procedure affects the outcome of measurements. The parameters influencing the detection volume are optical aberration due to incorrect coverslip thickness or incorrect positioning of the coverslip, refractive index mismatch, or astigmatism, which can easily lead to a 50% error in diffusion and even higher errors in concentration measurements [31]. Other factors that can affect measurements include background light, photobleaching, improper laser power, and the presence of bright aggregates in the sample [20].

The way to reduce the impact of optical and photophysical factors that influence FCS is the scrupulously performed calibration procedure of FCS set-up (described in A.2). The calibration process relies on measurements of ACF of a standard dye with a well-known value of diffusion coefficient (determined by other methods) and the same excitation wavelength as the fluorophore in the examined system. As long as all parameters like cover glass thickness, refractive index, and beam astigmatism are the same between the reference and the examined system, determining sample diffusion coefficient and concentration will yield correct results [31].

The negative effect of the occurrence of bright aggregates in samples can be minimized by taking several short measurements instead of one long data acquisition or manually discarding distorted autocorrelation curves [32].

Limitations of FCS in complex systems

Following the successful application of FCS to living cells, it began to be used in more complex biological systems, such as tissues, gels, or biofilms [33–35].

Fluorescence correlation spectroscopy applied to complex, optically dense systems can complicate measurements and data interpretation. A possible source of error is the distortion of the laser beam profile, resulting in the deformation of the confocal volume and a weak fluorescence signal. By increasing the laser power, a weak emission can be eliminated. However, too high laser power can cause other adverse effects such as increased autofluorescence, photobleaching, and photodamage. Besides, an increased laser power does not address the problem of confocal volume deformation. Should we be concerned about it?

A study by Zustiak [36] provides an insight into the effect of scattering on FCS measurements. It has been shown that the scattering of the laser beam causes up to a twofold increase in the effective confocal volume. The volume expands axially (elongation of the longer axis, z_0, Fig. 2.5), while changes in the focus's shorter half-axis, ω_0, are insignificant. In consequence, only a slight (up to 10%) elongation of the molecules diffusion time was observed. The increase in volume has led to a higher number of molecules detected inside the detection volume, with a decrease in their brightness.

Another crucial issue is the impact of the positioning depth within a biological sample on the outcome of FCS experiments. The analysis of FCS measurements at different depths of the detection volume in multicellular spheroids is presented in the work of Leroux [37]. It has been shown that in spheroids, the number of detected molecules in the confocal volume is independent of the positioning depth. On the other hand, an exponential decay in the number of recorded photons, typical for a scattering medium, was observed. The loss of photons results in a weak signal to noise ratio for FCS measurements deeper than 50 μm.

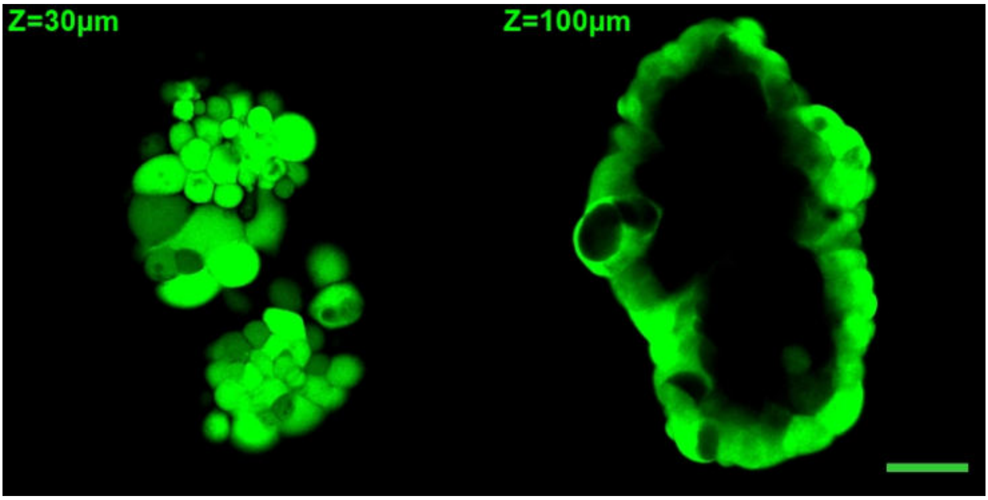

Figure 2.6: Confocal images of MCF-7 spheroids stained with calcein-AM at two different depths. At a depth of $Z = 30\ \mu m$ from the bottom of the glass, we obtain a strong fluorescence signal from the second layer of MCF-7 cells forming spheroid. At a depth of $Z = 100\ \mu m$, we do not obtain a fluorescence image from the interior of the spheroid caused by the laser beam scattering through successive layers of cells. Excitation wavelength 488 nm. Scale 50 μm.

To draw a conclusion, the FCS can be implemented in studies of biological complex systems. We should not observe the adverse consequences related to the widening of the shorter axis, ω_0 of the focal volume. However, we should be cautious with concentration analysis. A well-chosen laser power should yield a strong fluorescence. Unfortunately, it is impossible to perform mobility analysis within the entire volume of spheroids, which is clearly depicted in Fig. 2.6.

3

Structural studies of proteins

Contents

FCS has been used in diverse studies aimed to monitor the changes in protein conformation [25, 38, 39]. The conformational changes are assessed by the measurement of the diffusion coefficient of a protein. Changes in the diffusion coefficient can be induced by processes causing the changes in the hydrodynamic radius r_h.

In this part of my work, I am presenting the fluorescence correlation spectroscopy application in studies on the effects of TMA and TMAO on the structure of proteins.

3.1 Introduction

Trimethylamine N-oxide (TMAO), one of the dietary choline metabolites, has been correlated with cardiovascular diseases in hundreds of publications. The leading and most cited ones are [1–4]. Based on them, choline is taken from the diet, and the gut microbiota transforms it into trimethylamine (TMA). Then, TMA is absorbed by the intestine and delivered to the liver, where TMA is metabolised into TMAO. Finally, TMAO is distributed throughout the body, affecting lipid and hormonal homeostasis, which may suggest a contribution of TMAO to the development of cardiovascular diseases, which is schematically shown in Fig. 3.1.

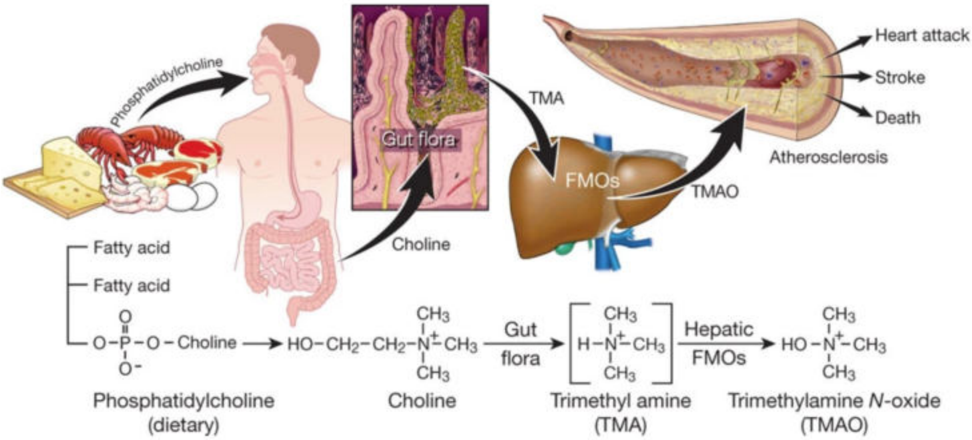

Figure 3.1: Gut-flora-dependent metabolism of dietary phosphatidylcholine had been suggested as related to the cardiovascular events [1].

Nonetheless, the molecular mechanisms connecting increased plasma levels of TMAO to cardiovascular diseases are still unclear [40, 41]. At the same time, contradictory results about TMAO impact on living organisms exist [42–44].

Noteworthy, the role of TMA, the precursor of TMAO, has not gained attention in cardiovascular studies, even though it is defined as a uremic toxin.

To find out which of them, TMA or TMAO, exerts harmful effects and can be treated as a marker of cardiovascular risk, we perform a multilevel comparison analysis [5, 45]. Foremost, we examined the plasma levels of TMA and TMAO in healthy humans and cardiovascular patients. Furthermore, we studied the effect of TMA and TMAO on cardiac muscle cells (cardiomyocytes) and proteins: cardiac lactate dehydrogenase (LDH) and bovine serum albumin (BSA).

3.2 FCS in structural studies of proteins

This research aimed to show that the use of FCS provided information about changes incurred by proteins exposed to TMA and TMAO.

Proteins that are exposed to these factors may get denatured or degraded (Fig. 3.2). The loss of tertiary (and often secondary) protein structure not involving covalent bond cleavage is known as denaturation. The protein's hydrodynamic radius, R_h gradually increases during the denaturation process, and protein reaches a highly open conformation. Hence, unfolded proteins may interact with the exposed hydrophobic sequences and form aggregates [46].

Degradation, on the other hand, is the loss of primary structure with associated covalent bond cleavage [47]. Upon degradation, the protein breaks up into smaller polypeptides or single amino acids.

According to the Stokes-Einstein equation (2.4), the protein's hydrodynamic radius, R_h is inversely proportional to diffusion coefficient, D. Hence, analysing the diffusion coefficients of proteins measured with

FCS yields valuable data on structural changes in proteins exposed to toxic substances.

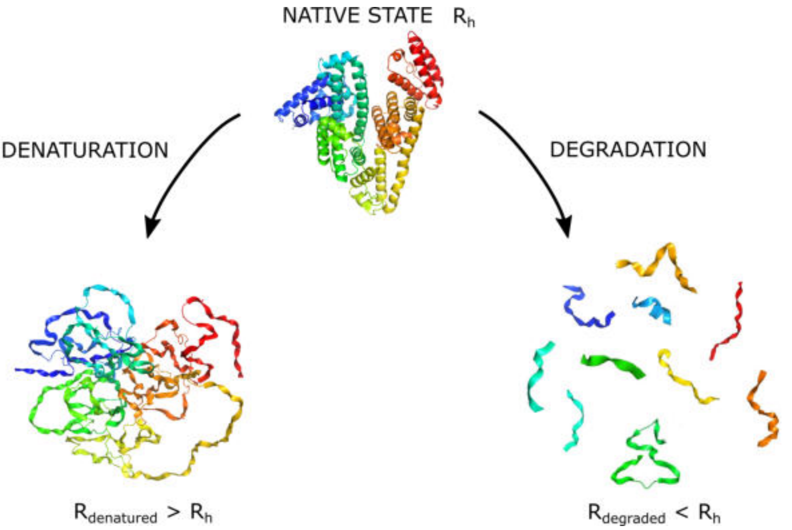

Figure 3.2: Proteins exposed to chemical agents can denature or degrade. Denaturation of protein leads to an increase in the radius, while degradation results in protein breakdown into fragments, characterised by a smaller radius than protein in the native state.

3.3 The effect of TMA and TMAO on protein structure

According to the protein labelling protocol (A.4), I conjugated the ATTO 488 dye to bovine serum albumin (BSA) and cardiac lactic dehydrogenase (LDH). Subsequently, I incubated around 4 μM proteins solution with TMAO and TMA at a series of concentrations at 20 °C for 24 h. After the incubation time, I diluted proteins in PBS buffer[1] to nanomolar concentration and performed FCS measurements (using the FCS set-up

---

[1] The content of TMA or TMAO in the final solution was lower than 0.5%. The dilution allowed me to eliminate the influence of different viscosity values of TMA or TMAO solutions on the measured diffusion coefficient values. I assumed that every solution had the same viscosity of the PBS buffer.

described in A.1), starting from a calibration procedure A.2. I analysed the experimental results by fitting the raw data with the autocorrelation function describing a two-component diffusion model (Eq. 2.2). Even though I purified protein in the protein labelling procedure, dye molecules ATTO 488 (around 10% of all detected particles) were still present in the sample as a fast diffusing fraction[2]. The second fraction of molecules in the model corresponded to fluorescently labelled proteins.

In experiments, proteins in PBS buffer served as a control. I determined diffusion coefficients of proteins in a native state to be equal to $D = 55.16 \pm 1.08\ \mu m^2/s$ for BSA, and $D = 54.76 \pm 2.01\ \mu m^2/s$ for LDH, which are in a good agreement with reported values [48, 49]. Only comparing results obtained in the control measurements and protein exposed to TMA or TMAO allows me to draw the correct conclusions.

Twenty-four-hour incubation with TMA induced the degradation of both examined proteins manifested as a significant shortening of the diffusion time (Fig. 3.3). Precisely, there was a six-fold and three-fold increase in the diffusion coefficient, D, for albumin and LDH, respectively, at TMA concentration of 100 and 200 mM (Fig. 3.4). In contrast, strikingly, incubation with TMAO did not affect the diffusion coefficient of the studied proteins [5].

Given that TMA degraded both proteins within only 24 hours, it is most likely that TMA, but not TMAO, has adverse effects on cells, tissues, organs, and consequently a whole organism. That is why TMA, but not TMAO, should be considered as a marker of cardiovascular risk.

---

[2] The diffusion coefficients estimated in a separate experiment for ATTO 488 dye in PBS buffer had the same value, $D = 359.68 \pm 7.58\ \mu m^2/s$, as the fast diffusing fraction in the protein sample.

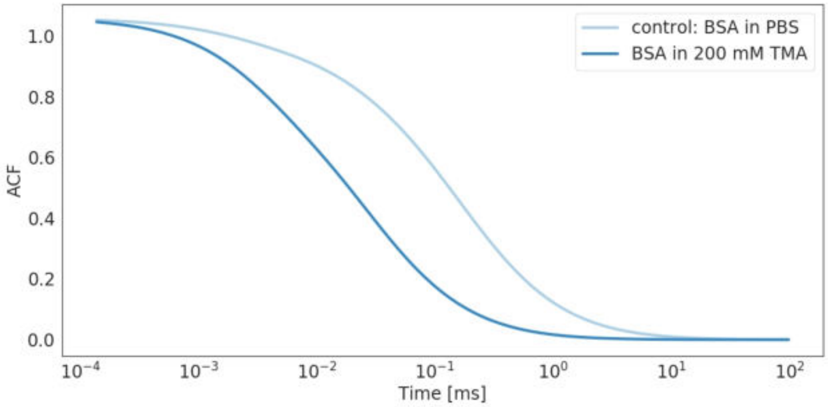

Figure 3.3: The difference in measured FCS curves described by the equation 2.2 for bovine serum albumin (BSA) in PBS buffer (control) and BSA exposed to 200 mM TMA for 24 h. The diffusion time of protein in the native state is longer than for fast diffusing fragments of degraded protein, which influences the shape of the ACF curves.

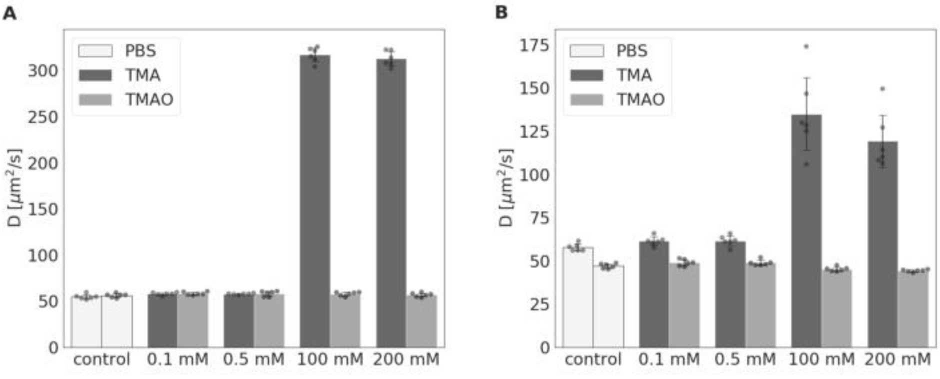

Figure 3.4: Diffusion coefficient, D, obtained for (A) albumin and (B) LDH after 24-hour incubation with either PBS buffer (control), TMA, or TMAO at increasing concentrations (n = 6) [5].

In my research, I observed a harmful effect of TMA on proteins at 100 mM and higher concentrations. Nevertheless, the measured plasma level of TMA was in the range of micromoles [5]. This observation raises the question of whether a long time of protein exposure to TMA at a concentration of micromoles would also reveal the harmful effect on its structure.

3.4 Long term protein exposition to TMA

I studied the long-time impact of trimethylamine in a concentration range of 20 μM - 100 mM on the structure of human serum albumin (HSA)[3]. Firstly, I made a series of trimethylamine solutions of various concentrations by dissolving 45wt. % TMA in H2O (Sigma-Aldrich, USA) in PBS buffer. Then I measured the pH value of the prepared solutions with a pH-meter (HI 3221-02 Model, Hanna Instruments$^{\text{TM}}$, USA). The concentration range of TMA solutions, as well as their pH, are presented in Tab.3.1.

Table 3.1: Concentrations, C, of TMA solutions and their pH. I also include a control solution - a PBS buffer without TMA.

C	0	20 μM	50 μM	100 μM	500 μM	1 mM	10 mM	100 mM
pH	7.41	7.41	7.46	7.52	8.42	9.85	10.93	11.66

To the prepared TMA solutions, I added the labelled HSA (A.4) at a final concentration of 4 μM. Subsequently, HSA solutions with different TMA concentrations were incubated at the temperature of 20 °C, protecting the samples from the light.

On selected days of incubation, I performed FCS measurements of HSA in PBS buffer (control) and HSA exposed to TMA at a concentration range of 20 µM – 100 mM. Because the HSA lifetime is 28-36 days, I chose not to extend the experiment beyond 29 days. The results are shown in Fig. 3.5.

---

[3] I decided to change the examined protein from BSA to HSA. BSA presents 76% sequence identity with HSA; however, HSA has higher thermal and chemical stability [50]. Furthermore, most importantly, I want to relate the results of my studies to a human being.

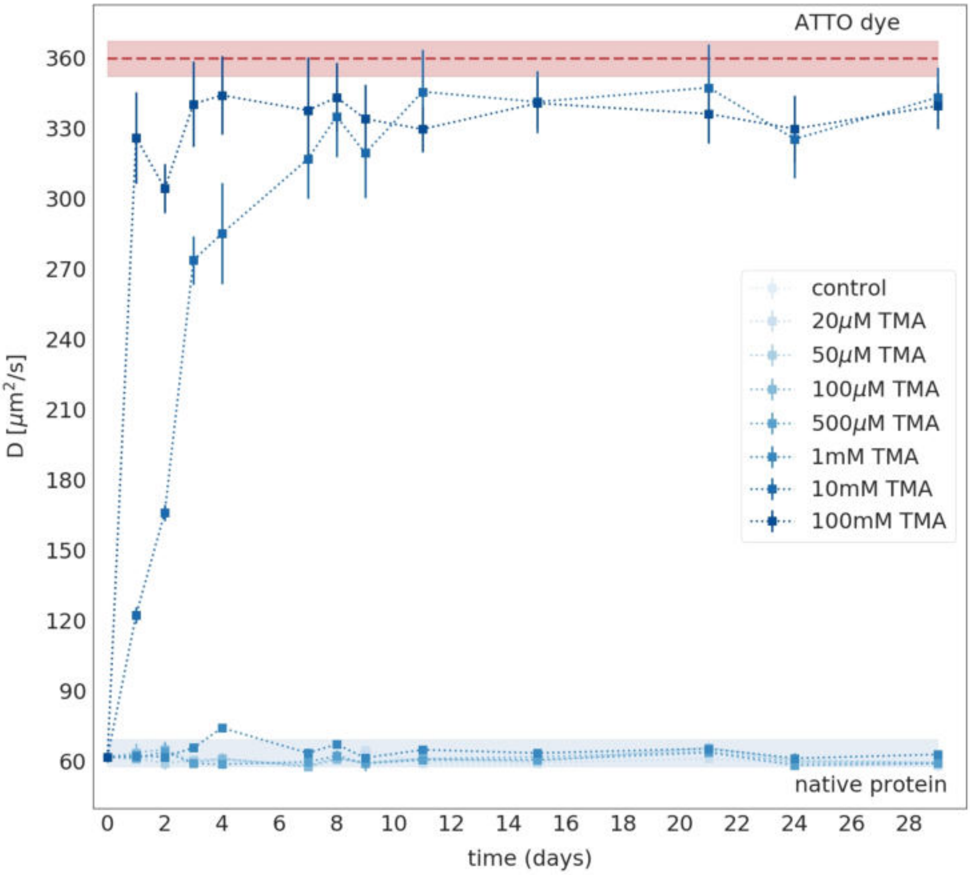

Figure 3.5: Changes in diffusion coefficients D of human serum albumin exposed to different concentrations of TMA from 20 μM to 100 mM for 29 days. According to the presented data, the maximum tested concentration of TMA, which does not influence protein structure, is 1 mM. Each point corresponds to 30 independent data acquisitions using FCS. Blue field presents D value ± SD calculated for protein size in its native state. The red field presents measured D value ± SD for ATTO 488 dye. Control corresponds to HSA in PBS buffer.

According to obtained data, HSA after exposition to TMA at a concentration above 10 mM is degraded, revealed as an increase in diffusion coefficient compared to the control. The maximum tested concentration of TMA, which does not influence the HSA structure, even for 29 days of incubation, is 1 mM.

One might wonder if TMA cleaves the dye-protein bond and thus has no effect on the protein structure. However, in Fig. 3.5, we can notice, that HSA is degraded gradually. In the case of 10 mM TMA concentration, there is no sudden increase in the diffusion coefficient from the value corresponding to the native structure to the value corresponding to the diffusion coefficient of the dye. To affirm this outcome, I also monitored for 3 hours the change in the diffusion coefficient of HSA treated with 1 M TMA, from the point of adding TMA to the protein solution. Results are presented in Fig. 3.6.
After 5 minutes from adding TMA, HSA is denatured (decrease in the diffusion coefficient value with reference to D for protein in the native state). I base my interpretation on theoretical calculation. According to Wilkins [51], the empirical relationship between the hydrodynamic radius, R_h, and the number of residues in the polypeptide chain, N, for highly denatured states is:

$$R_h = 2.21 N^{0.57} [\text{Å}] \tag{3.1}$$

The hydrodynamic radius of denatured HSA is equal to $R_h = 8.35$ nm since it has 585 amino acid residues [52]. Using the Stokes-Einstein relation (Eq. 2.4), we can easily calculate that diffusion coefficient of denatured HSA is around $D = 29.35\ \mu m^2/s$, which has been appropriately marked in Fig. 3.6. As we can see, the estimated value of the denatured state of HSA equates with the experimentally measured values.

By following further changes in the protein diffusion coefficient, the unfolded peptide chain, after around 20 minutes of adding TMA, is degraded into smaller and smaller polypeptide chains, as evidenced by the increasing value of the measured D.

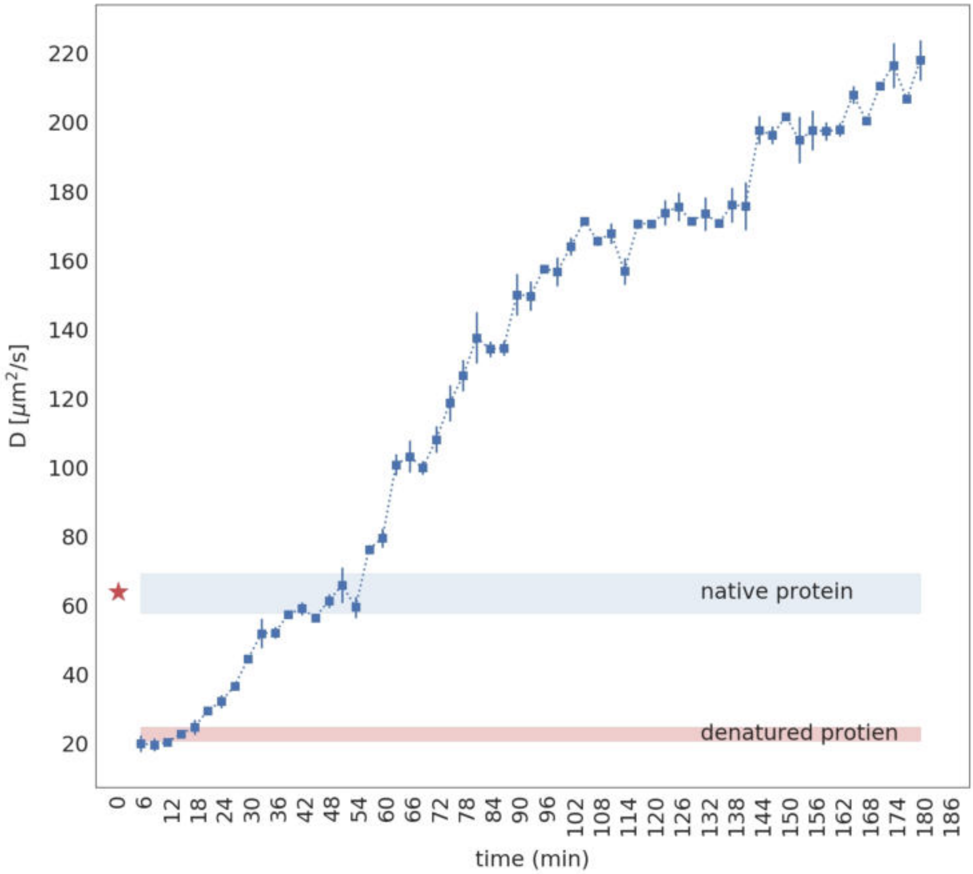

Figure 3.6: Changes in diffusion coefficients D of human serum albumin (HSA) exposed to 1 M TMA followed for 3 hours. The red star represents D value for protein in a native state, before adding TMA. HSA in the presence of TMA is first denatured and then gradually degraded. Each point corresponds to 3 independent data acquisitions by means of the FCS.

3.5 SDS-PAGE study supports FCS results

In addition to FCS experiments, I performed sodium dodecyl sulfate polyacrylamide gel electrophoresis (SDS-PAGE) to prove the HSA degradation by TMA.

SDS-PAGE is a method for resolving proteins by size and charge. Sample preparation for SDS-PAGE analysis consists of denaturing proteins with heat in the presence of SDS and a reducing agent such as mercaptoethanol. Additionally, SDS coats proteins, providing them with a negative charge proportional to their length. When the coated sample is run on a gel in response to an electrical field, the proteins separated by charge and the gel sieving matrix effect. The higher the acrylamide concentration, the smaller the pore size in the gel matrix. Mobility through the gel is affected by the size of the protein. Small proteins move through the resolving gels more quickly than the large ones. For this reason, the application of SDS-PAGE in research allows direct visualization of protein degradation, isolation, or to estimate molecular weights for unknown proteins [53, 54].

In my work, I used SDS-PAGE as an attractive approach to protein degradation characteristics, similarly to how it has been presented in the study by Sadeghi [55].

Protein solutions for SDS-PAGE analysis were prepared in the same way as for FCS experiments - by dissolving HSA in PBS buffer, omitting fluorescent labelling. The HSA was added to the prepared TMA solutions at a final concentration of 4 μM. Then, HSA solutions with different TMA concentrations were incubated at the temperature of 20 °C, protecting the samples from the light. In selected days of incubation, I performed SDS-PAGE according to the protocol described in A.5.

Electrophoresis analysis of HSA (Fig. 3.7) incubated in TMA solutions at different concentrations revealed that protein in the presence of TMA at 100 mM and 1 M was entirely degraded within 2 days (Fig. 3.7.A). The degradation led to protein breakdown into fragments smaller than 10 kDa, which were not detectable in 12 % Bis-Tris gel.

The elongation of exposure time of HSA to TMA reveals similar results obtained by FCS - protein was stable [4] with TMA in concentrations up to

---

[4] The molecular mass of unimpaired human serum albumin is 66.5 kDa [52], as it has been detected in the SDS-PAGE pattern (Fig. 3.7).

1 mM (Fig. 3.7.B). Higher tested concentrations of TMA led to protein degradation into smaller polypeptides than 10 kDa.

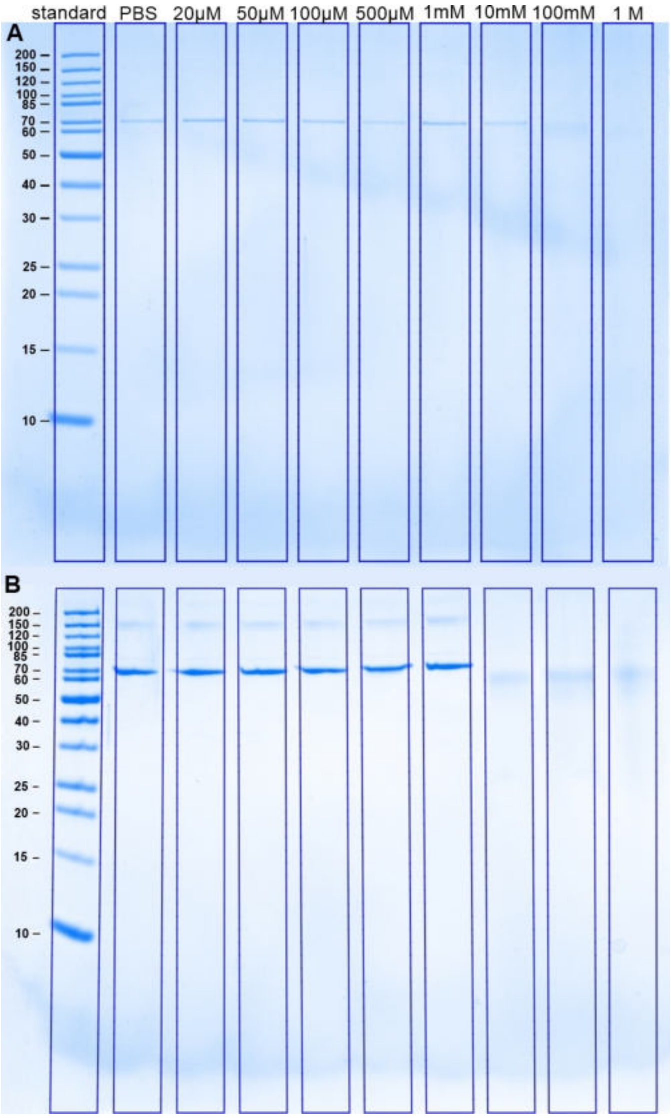

Figure 3.7: SDS-PAGE pattern of human serum albumin exposed for (A) 2 days and (B) 28 days to various concentration (20 μM - 1 M) of trimethylamine (TMA) on 12 % Bis-Tris gel. The first lane from the left shows the molecular weight of the standard in kilodaltons. The difference in band brightness between the two gels is due to the B gel's longer destaining time.

One may presume that these barely visible bands detected in lanes '10 mM', '100 mM'or '1 M'(Fig. 3.7) correspond to the unimpaired HSA. To address these doubts, I compared the intensity of bands captured for HSA in PBS buffer and HSA in the presence of 10 mM of TMA (Fig. 3.8). The detected band for control has an intensity of more than 1 000 units higher than the intensity of the band captured in a lane loaded with HSA exposed to 10 mM of TMA. Based on the band intensity analysis, I have assumed that the weak signals observed in the lanes mentioned above comprise the background. Similar patterns for degraded proteins are presented in work by Sadeghi [55].

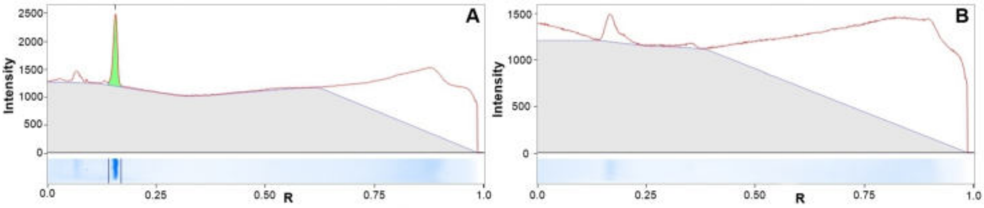

Figure 3.8: The lane profiles of (A) HSA in PBS buffer and (B) HSA exposed to 10 mM of TMA. The lane profile shows a cross-section view of a single lane rotated 90°. The Y-axis of the lane profile represents intensity, while X-axis the relative migration, *R* (the distance migrated by a band divided by the distance migrated by the dye front). The detected band for control (A) is much brighter than the band of the background.

3.6 Possible mechanism of protein degradation by TMA

So far, I have provided an extensive study corroborating the disturbing effect of trimethylamine on protein structure. The missing part of this research is the explanation of the mechanism of protein degradation by TMA. I deem that this mechanism is well-known in life science and it is the process of the alkaline hydrolysis of peptide bond [56, 57].

The increase in TMA concentration is related to the increase in pH solution, as shown in Tab. 3.1. In aqueous solutions, trimethylamine ionises since it is a weak base (pKb = 4.2):

$$(CH_3)_3N + H_2O \rightleftarrows CH_3NH^+ + OH^-$$

In the presence of OH^- ions, the alkaline hydrolysis of peptide bonds can occur [58].
Another weak base, ammonia (pKb = 4.7), undergoes a similar reaction:

$$H_3N + H_2O \rightleftarrows H_3NH^+ + OH^-$$

Hence, I decided to conduct an experiment to verify the effect of ammonia on protein structure. When protein exposure to ammonia would also lead to its breakdown, as in the instance of TMA, it is reasonable to conclude that the mechanism of protein degradation is linked to the alkaline hydrolysis of the peptide bond.

In the conducted experiment, I followed for 3 hours the changes in the diffusion coefficient of HSA protein exposed to 1 M ammonia, from the point of adding ammonia to the protein solution. The results are presented in Fig. 3.9 and compared with the obtained data in a similar experiment when I was using TMA.
After 60 minutes from adding ammonia, HSA is gradually degraded into smaller and smaller polypeptide chains, as evidenced by the increasing value of the measured diffusion coefficient. However, the protein exposition to ammonia did not result in its denaturation. Furthermore, unlike TMA, the process of protein breakdown is much markedly slower.

My observations of ammonia's disrupting effect on protein structure are consistent with Tarelli's research findings [59]. His work demonstrated that ammonia cleaves polypeptides at asparagine proline (Asn-Pro) bonds. Human serum albumin possesses an Asn-Pro sequence in the domain I [60].

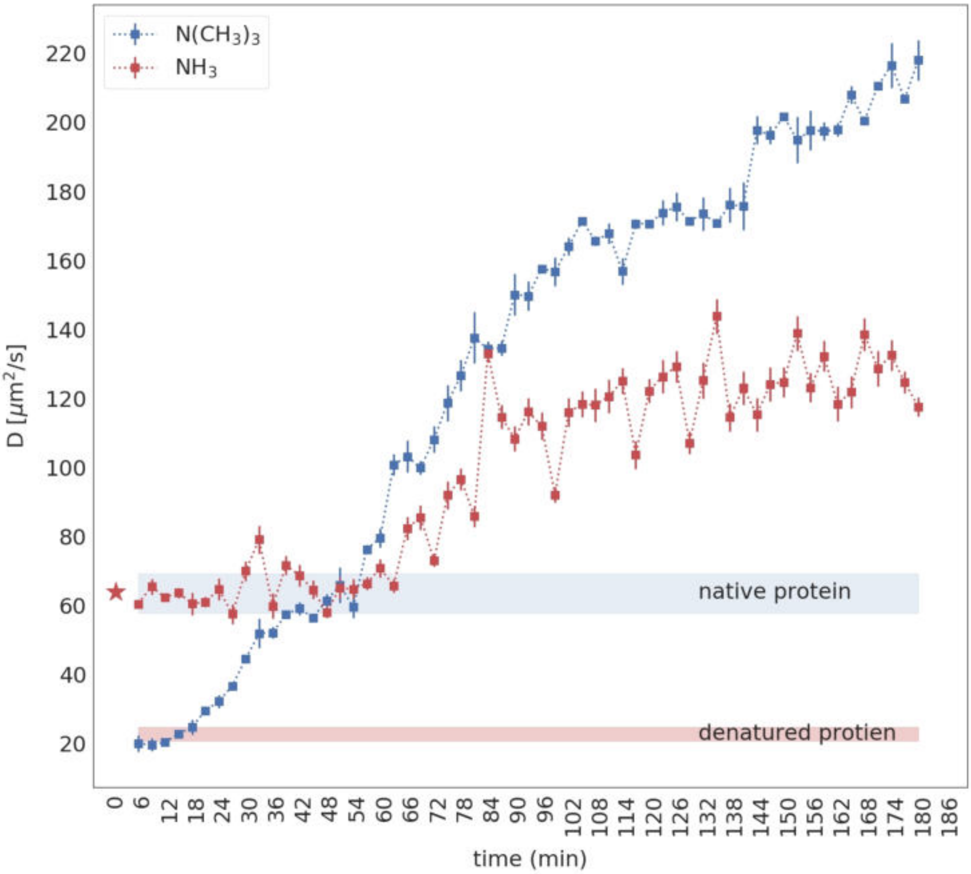

Figure 3.9: Changes in diffusion coefficients *D* of human serum albumin exposed to 1 M TMA ($N(CH_3)_3$) and 1 M ammonia (NH_3) followed for 3 hours. The red star represents *D* value for protein in a native state, prior to the addition of tested compounds. HSA in the presence of TMA as well as ammonia is gradually degraded. Each point corresponds to 3 independent data acquisitions by means of the FCS.

3.7 Conclusions

My work contributed to the findings, which seem to challenge the current thinking on TMAO as a cardiovascular risk factor. We proposed that TMA but not TMAO may be a marker of cardiovascular risk. First of all, cardiovascular patients demonstrated increased plasm TMA level.

Additionally, increased dietary TMAO in rats, which elevated plasma TMAO level 3-5-fold, did not cause the difference between control and TMAO treated rats in survival rate. Besides, TMA but not TMAO exerts adverse effects on cells, very likely due to TMA disturbing effect on proteins [5, 45].

Those conclusions would not be reached without utilizing a variety of approaches. Aside from the critical, descriptive data reported in medical research, we provided the mechanism by which TMA exerts negative effects on living organisms. In this case, a valid tool appeared to be fluorescence correlation spectroscopy.
By applying FCS, I proved that TMA impaired proteins structure irreversibly - caused their breakdown into small fragments, detected by FCS with sub-nanometer resolution. Interestingly, the SDS-PAGE method commonly used in protein degradation studies was not sensitive enough to capture protein degradation products. An increase in acrylamide concentration would probably increase the separation resolution; nevertheless, this reveals a drawback of the technique. Application of SDS-PAGE seems not convenient when we do not know the expected molecular weights of the products in the degradation process. Furthermore, by using electrophoresis analysis, it is not possible to resolve proteins in a wide range of sizes.

In the carried out long term experiment of protein exposure to TMA, I found that protein exposition to TMA at a concentration of 1 mM did not influence HSA structure even for 29 days of incubation. This result is likely due to the low concentration of OH^- ions present in a 1 mM TMA solution.

To summarise, the described findings reveal a clear understanding of the negative role of TMA on living organisms. To some extent, it was due to FCS, which appears to be an excellent tool in medical research. The structural studies of proteins exposed to TMA and TMAO allowed assessing which of them exhibits a negative impact at a molecule level.

4

Structural studies of cell interior

Contents

The cell is the smallest building block of all living organisms. An accurate depiction of intracellular structure has been challenging for scientists worldwide for almost a hundred years [61, 62]. A clear understanding of the cell structure provides not only knowledge about the basic properties of a cell. Moreover, it allows for the design of new therapies that target intracellular components.

In this chapter, I am giving a comparative analysis of the cytoplasm structure in the 2D and 3D culture of cells. Furthermore, I demonstrate that the method of cell culture (2D and 3D) influences the cytoplasm organization and expression of a protein, PARP1, that is targeted in anti-cancer therapy.

4.1 Introduction

The cytoplasm fills the inside of a cell. The aqueous phase of the cell contains a wide variety of solutes, including inorganic ions, building blocks of major organic constituents, intermediates in metabolic pathways, carbohydrate and lipid energy stores, and a high concentration of proteins and RNA. In addition, the cytoplasm constitutes an entangled network of cytoskeletal fibres. The high concentration of macromolecules, organelles, and the network of cytoskeletal polymers make the cytoplasm an extremely complex system, as shown in Fig. 4.1 [63, 64].

The interior of such a complex environment is supposed to have a gel-like composition with a far higher macroscopic viscosity than water. Intracellular viscosity is a fundamental physical parameter that plays an essential role in maintaining cell structure and function. Most notably, the viscosity of the cytoplasm has a direct effect on diffusion and interaction between biomolecules, and, consequently, it affects all biochemical reactions in living cells [65].

Several studies demonstrate that the viscosity of the cytoplasm is not constant. When the interior of a cell is probed using small particles, the measured viscosity decreases rapidly with the probe size [8, 17, 66, 67]. The length-scale viscosity model has been developed to describe the mobility of nanoprobes in the cytoplasm based on their hydrodynamic radii and cytoplasmic viscosity. According to the theory, nanosized biomolecules (with hydrodynamic radii r_p in the range of 1-5 nm) diffuse in the cytoplasm orders of magnitudes faster than those predicted by the

Stokes-Einstein equation $D = kT/6\pi\eta_{macro}r_p$ based on the macroscopic viscosity η_{macro}, since they experience nanoviscosity. The model has been confirmed in several studies [8, 28, 67, 68].

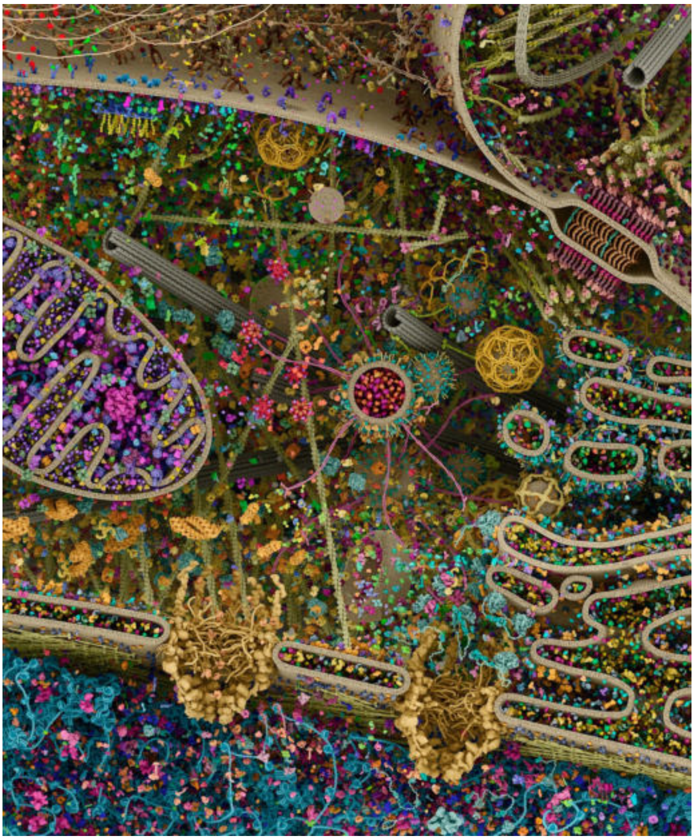

Figure 4.1: The scheme of the cell's interior. All of the cellular components, along with the aqueous phase of the cell, produce an incredibly complex environment [69].

Recently published studies [8, 68] have demonstrated that nanoviscosity is conserved in human cells, regardless of the cell cycle and cell line origin. However, the research was limited to monolayer cultured cells, which have a significantly different morphology than cells in tissues. As has been shown [70], the differences between the 2D and 3D-organized cells can be identified not only in cell morphology but also in intracellular structure.

These differences include endoplasmic reticulum content, cytoskeletal filament organization, and protein expression - all of which can have a significant impact on intracellular viscosity.

In view of the aforementioned, it is appropriate to measure cytoplasm viscosity in 3D cultures and compare the findings with those obtained in 2D cultures. Nonetheless, before proceeding to intracellular studies, it is essential to be familiar with the methodology of cell cultures.

4.2 Cell cultures

In vitro cell cultures are widely used in medical, biochemical and molecular research, and they provide easy access to biological materials. Cell culture allows cells to be manipulated and investigated for a variety of purposes, including (i) studies of cell structure and function; (ii) measuring the effects of chemical compounds on specific cell type; (iii) cell engineering to produce artificial tissues; (iv) large-scale synthesis of biological materials (therapeutic proteins and viruses).

The *in vitro* culture environment must meet the fundamental physiological requirements of the cell to promote cell survival and proliferation. Components that one can control include factors associated with the medium, such as its composition, pH, and osmolarity. In addition, incubation conditions such as temperature, relative humidity and gas composition can be regulated, as can the form and composition of the substrate for cell attachment [71].

Cell culture most commonly involves the growth of cells on a substrate (usually plastic). Cells are seeded in a liquid medium into a culture flask, the cells attach and proliferate and can be subcultured following release from the substrate by a short exposure to a solution containing trypsin and EDTA as I described the procedure in A.6.

The majority of cell experiments are carried out with the cells of interest cultured on the surface in a 2D monolayer. This method of cell culturing is the most popular because it is simple and convenient. Monolayer cultured cells have a well-controlled and homogeneous cell environment, which facilitates microscopic analysis and sustains most cell types to proliferate. The conventional 2D culture has enabled an understanding of the complex cellular physiology of how cells function and respond to stimuli. Additionally, it has been an invaluable method providing fundamental knowledge as models of various diseases. However, this is generally not considered as the natural microenvironment of the cells. The cells cultured as a monolayer do not mimic the three-dimensional architecture of tissues or tumours [72, 73].

2D cell cultures and their inability to form more natural tissue-like structures have a significant effect on cell performance and, as a result, biological assay outcomes. Monolayers of cultured cells, for example, are thought to be more vulnerable to therapeutic agents [74]. Furthermore, cell culture on surfaces can promote cell proliferation but inhibit cell differentiation due to the cell interactions. A better engineered cell culture environment may help understand tissue morphogenesis and improve the predictive accuracy of the drug discovery process. Because of the numerous drawbacks of 2D cultures, researchers needed to find alternative models that could better simulate a natural environment, such as a 3D culture of cells [75, 76].

Over recent years, numerous methods of three-dimensional cell culture have been developed. Three-dimensional cultures are excellent *in vitro* models, mimicking the *in vivo* processes: cell-to-cell and cell-to-matrix interaction in conjunction with cell morphology. In contrast, cell growth on the surface results in cell flattening (Fig. 4.2) and remodelling of its cytoskeleton. The cell culture condition has been shown to alert gene expression and protein synthesis [70, 73].

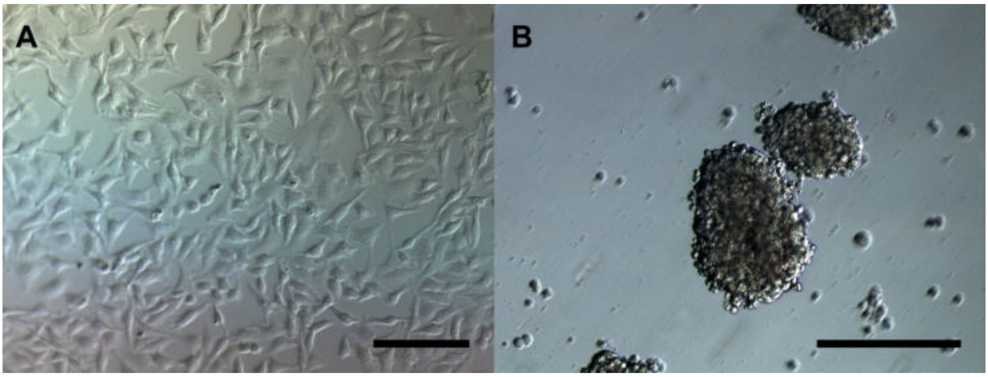

Figure 4.2: Impact of the method of cell culture on their shape in the example of the HeLa cell line. **A** In 2D culture, cells grow as monolayer are flat, scale bar 50 μm. **B** In contrast, cells cultured in a 3D model have a spherical and more natural structure, scale bar 250 μm.

Three-dimensional cultures have morphological features corresponding to tissues *in vivo* [77]. They are also considered a tumour model since they have many characteristics of *in vivo* tumours that are usually not present in cancer cell lines cultured as a monolayer, including structural organization, cellular layered assembling, hypoxia, and nutrient gradients [78]. Spheroids display higher resistance to chemo- and radiotherapy than individual tumour-derived cells, making them a more predictive model of in vivo therapeutic efficacy [79].

The formation of 3D cell cultures is an example of the self-assembly process. In the absence of an attachment surface, cells aggregate - monodispersed cells create 3D models - multicellular spheroids. In more detail, it has been stated that spheroid formation has three critical steps, presented in Fig. 4.3. In the initial stage, dispersed cells in suspension create aggregates through cell-surface integrins and the extracellular matrix proteins (collagen, fibronectin, and laminin). After the preliminary aggregation, there is a 2-4 hour delay phase when E-cadherin expression is upregulated. Finally, cadherin-cadherin binding between two adjacent cells leads to the formation of strong cell-cell contacts and compaction of the spheroids within 16-22 h [80–83].

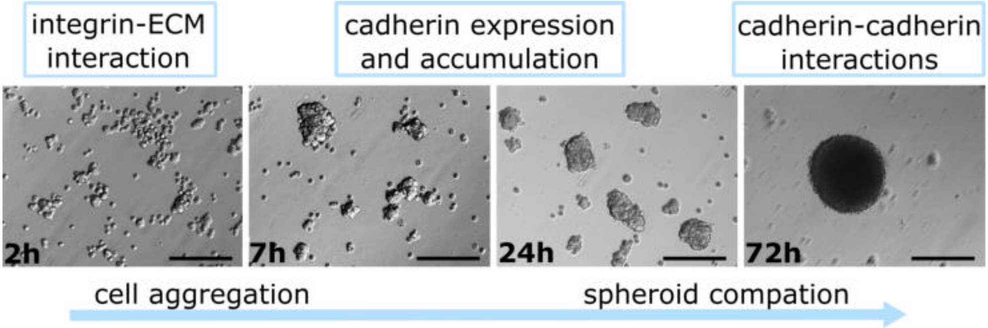

Figure 4.3: The spheroid formation process is displayed on the example of fibroblasts. The phase contrast images were taken 2, 7, 24 and 72 hours after cells seeding. Integrin-ECM interactions are involved in the process of cell aggregation. Then, cadherin is expressed at the membrane surface. Cadherin-cadherin interactions are responsible for compact spheroid formation. Scale bars 100 μm.

The relative ease of obtaining 3D cell cultures and their advantage over traditional ones make spheroids frequently used in numerous applications like differentiation studies, drug discovery and pharmacological applications, cancer research, gene and protein expression studies [6]. Surprisingly, the utilized diverse methodologies to study spheroids do not include the FCS technique.

4.3 FCS in 3D cell culture

Fluorescence correlation spectroscopy has been successfully applied to living cells [8, 19, 22, 23, 30]. Despite this interest, no one has employed FCS in intracellular studies within spheroids to the best of my knowledge. To address this gap, I established the following procedure for FCS experiments in 3D cell cultures.

Introduction of nanoprobes into cells

Prior to spheroid formation, the fluorescent nanoprobes have to be introduced into the cells. Several methods have been developed for this purpose: microinjection (molecules are injected directly into cell cytoplasm), a fusion of liposomes with cells, and osmotic lysis of pinocytic vesicles. Microinjection is not a method of choice. Since spheroids are made of thousands of cells, every single one of them has to be injected. Using liposomes requires their preparation and incorporation of nanoprobes inside vesicles. Moreover, the endocytosis or fusion of vesicles into cells takes hours [84]. The best alternative seems to be introducing molecules into the cell by osmotic lysis of pinocytic vesicles [85]. The cells are exposed to a hypertonic medium that contains molecules that must be loaded. Pinocytic vesicles form in this medium, and when the cells are transferred into a hypotonic culture medium, they break due to the increased internal osmotic pressure (Fig. 4.4). The method allows for loading a huge number of cells within around 30 minutes. However, it works only for small molecules up to about 10 nm in radius. A detailed protocol of nanoprobes introduction to cells I presented in A.7.

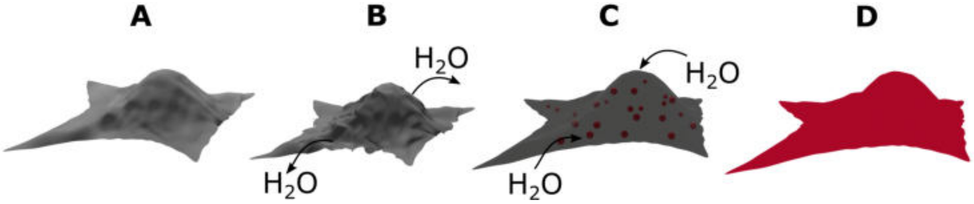

Figure 4.4: Principle of the osmotic lysis of pinocytic vesicles. (A) Cells are exposed to a hypertonic loading medium containing fluorescent probes. (B) When cells are exposed to a hypertonic medium, they lose water and shrink. The pinocytic vesicles are formed. (C) When the cells are placed in hypotonic lysis medium, the pinocytic vesicles burst, releasing their contents into the cytosol (D).

Culture of spheroids

In general, we can classify three types of 3D cultures based on their preparation methods: (i) suspension cultures on non-adherent plates; (ii) cultures in concentrated medium or in gel-like substances; and (iii) cultures on a scaffold [72]. In my studies, I generated spheroids using ultra-low attachment plates with a hydrophilic polymer coated surface, NunclonSphera™. The polymer coating prevents the binding of extracellular matrix proteins (collagen type I and fibronectin) to the surface and, as a result, inhibits the adhesion of cells to the bottom of the dish. Suspended cells aggregate and form three-dimensional spheroids, as explained in Fig. 4.3, which after 4 days of cultivation, reach several hundred micrometres in diameter. Spheroids cultures generated on non-adherent plates characterize non-uniform shape and size. Images of the obtained spheroids with the use of three different cell lines are shown in Fig. 4.5.

The procedure describing how to obtain such spheroids to study intracellular mobility of fluorescent probes is schematically depicted in Fig. 4.6. First, cells previously loaded with fluorescent nanoparticles are seeded on NunclonSphera™ dish in proper complete cell medium without phenol red (to eliminate the background fluorescence of phenol red). On the third day of spheroid culture, 50% of the medium was replaced. On the following day, spheroids were carefully transferred onto the 8-chamber cover glass Cellvis (Cellvis, USA) slide. The overnight incubation of spheroids attached to the glass ensured their immobility - the subsidence of spheroids on the glass surface during measurements could introduce undesirable effects related to the change in the location of the detection volume. FCS measurements were carried out five days after cell seeding.

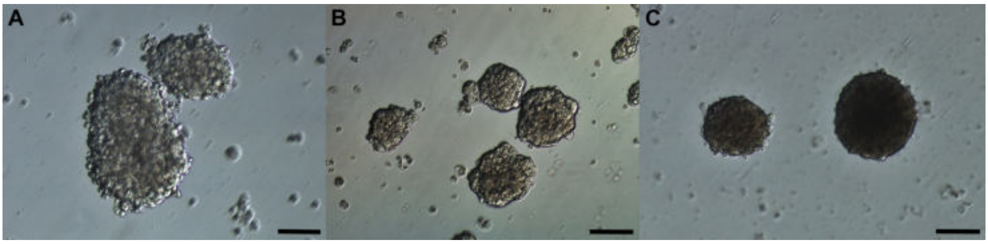

Figure 4.5: Spheroids are formed by three different cell lines: (A) HeLa, (B) MCF-7, and (C) fibroblasts. Phase contrast images were taken on the 5th day of culture on NunconSphera™ dishes. Scale bars 100 μm.

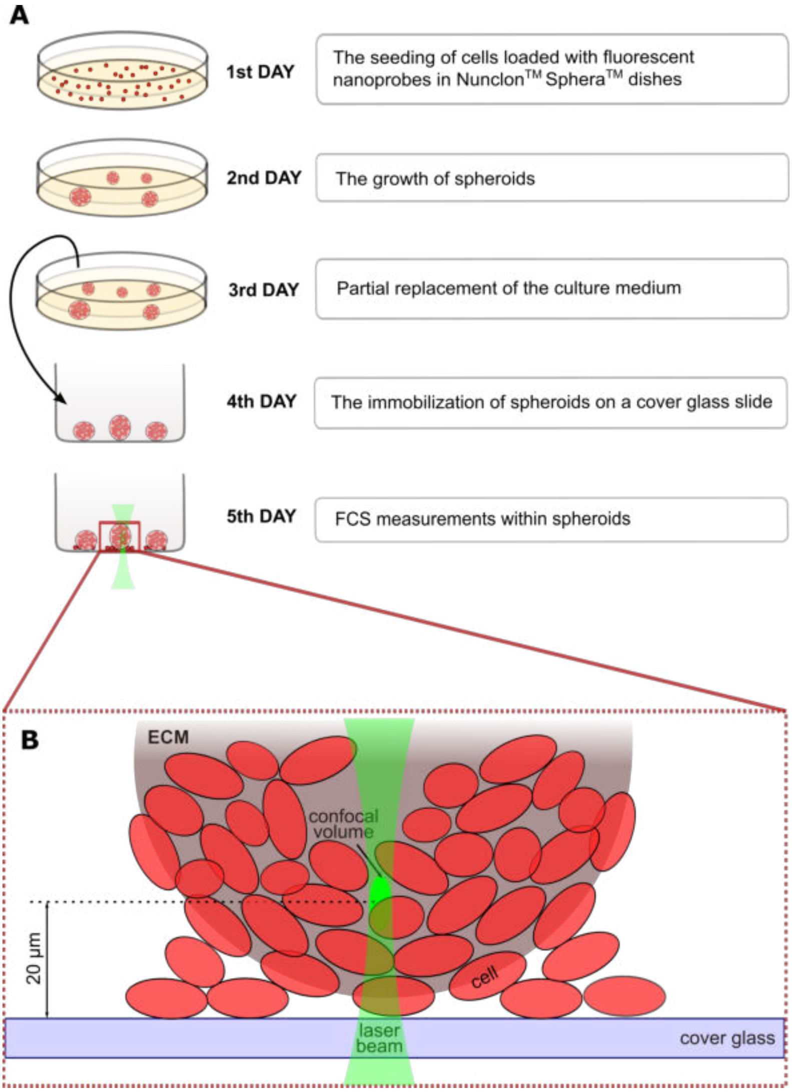

Figure 4.6: **A**. Scheme of the procedure for spheroid culture and their preparation for the measurements. Experiments were carried out with 5 day-old spheroids when they reached 400–600 µm in diameter. **B**. The confocal volume is positioned within a spheroid, and FCS measurements are performed.

FCS experiments in spheroids

FCS experiments were performed using the setup described in A.1. As a calibration solution, I used a nanomolar solution of rhodamine B in

2.5% glucose in PBS [86].

An essential step in the FCS experiments is the positioning of the detection volume along all three axes. The precise volume positioning allows measurements in the subcellular structures, i.e. the cytoplasm or nucleus. The location of the detection volume inside the spheroid is performed using the imaging mode of the confocal microscope. Fig. 4.7 depicts an example image of a cross-section of a spheroid to illustrate the positioning procedure. Due to the reported scattering of light by successive layers of cells within spheroids (2.5), I positioned the confocal volume at the maximum depth of 30 μm inside spheroids (corresponding to the third layer of cells).

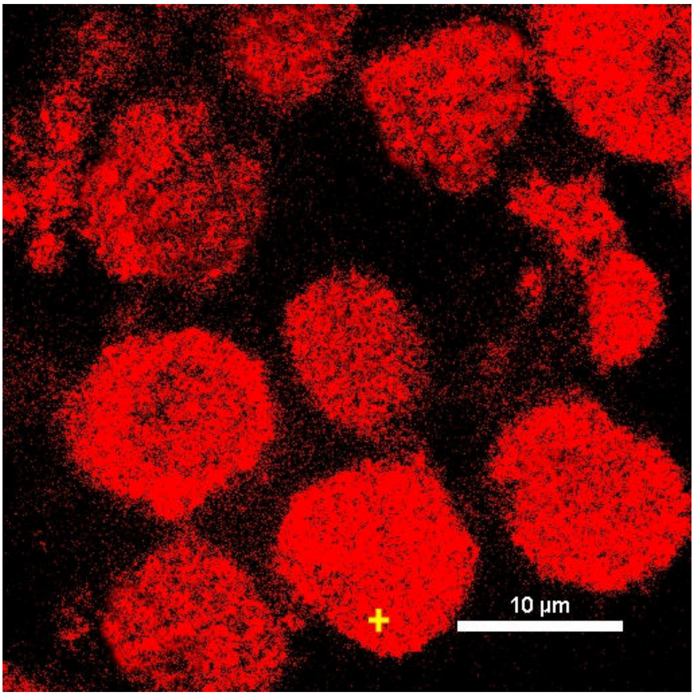

Figure 4.7: The positioning of the confocal volume within the cell of spheroids at 20 μm depth. The red fluorescence signal originates from TRITC-dextran 155 kDa loaded into cells. The yellow cross depicts an exemplary region of the cell chosen for FCS measurements. I avoided bright spots (corresponding to aggregates of molecules or dye enclosed in vesicles) and nuclei - the centre region of cells.

After setting the appropriate location for the confocal volume in the imaging mode, I switched the detection path from directed at the confocal detector to directed at the FCS detector.

I always applied the highest possible laser power, which did not photobleach the dye, ranging from 20-30 μW. During the measurements, the photobleaching manifests as a rapid decrease in the recording fluorescence signal, so it was easy to see (and eliminate) undesirable photophysical effects.
The exemplary results of the FCS experiment conducted for TRITC-dextran 155 kDa inside cells forming spheroid, I set together with results for the same nanoprobe diffusing in PBS buffer. All collected data was fitted using the model of single component anomalous diffusion (Eq. 2.1) since dextran is a polydisperse probe [86].

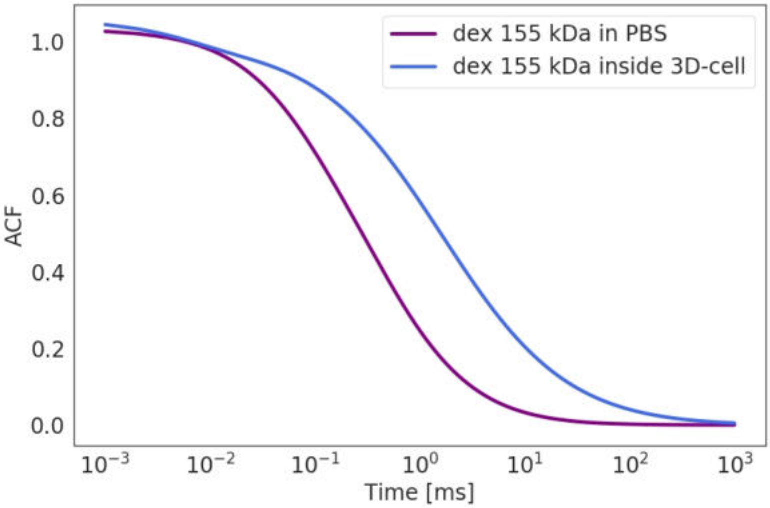

Figure 4.8: The differences in measured FCS curves defined by the Eq. 2.1 for TRITC-dextran 155 kDa in PBS buffer and inside cells of spheroids. The diffusion time of nanoprobes increases more than 4.5 times inside cells in comparison to the diffusion in PBS. Compared to the value obtained in PBS, the anomalous exponent acquired in intracellular experiments is reduced by 20%. Each of the curves is traced on the basis of the average from at least 20 measurements.

As expected, the estimated value of dextran 155 kDa diffusion time is slower inside the cells than in PBS buffer since cytoplasm viscosity is higher than the solvent. Dextran diffusion takes over 4.5 times longer in cells than in buffer. I also found that the anomalous exponent value decreases from 0.92 in the buffer to 0.72 in cells. A similar relationship has been reported by Kalwarczyk [86]. The reduced anomality parameter value is due to the length-scale dependence of hydrodynamic drag in the cytoplasm, which broadens the distribution of polydisperse probe diffusion times.

The observation suggests that the use of fluorescence correlation spectroscopy inside three-dimensional cell cultures produces correct results. Because of this consideration, I applied FCS to investigate the structure of cell interiors in spheroids.

4.4 Nanoviscosity of cytoplasm in 2D and 3D cells is conserved

I utilised fluorescence correlation spectroscopy to probe the cytoplasm of cells within a 3D culture and compared the results with those obtained for cells cultured as a monolayer [8].

The cell interior is a complex liquid composed of variously sized components. As a result, different intracellular constituents impede the diffusion of probes with varying radii. In the first step, the experiment involved the introduction of biologically inert tracers of different sizes: TRITC-dextrans [1] 4.4 kDa or TRITC-dextrans 155 kDa into HeLa cells (according to the procedure described in A.7) and generation of spheroids (as depicted in Fig. 4.6). I also used spheroids made of HeLa cell line expressing GFP protein, in which the introduction of fluorescence probes is redundant. Once the spheroids were immobilised on a cover glass slide,

---

[1] Dextran conjugated with tetramethylrhodamine isothiocyanate (TRITC) having bright red-orange fluorescence.

the FCS measurements were performed. Following the data acquisition, I analysed the FCS curves by fitting the single component anomalous diffusion model (as I described it previously) in self-written Phyton scripts. From the fitting procedure, I determined the diffusion coefficient of probes inside the cells. Then, using the fluctuation–dissipation theorem [87], from measurements of the probe's diffusion coefficient D, I was able to determine the effective viscosity, η_{eff} experienced by this probe:

$$\frac{\eta_{eff}}{\eta_0} = \frac{D_0}{D} \tag{4.1}$$

where D_0 stands for the diffusion coefficient of a given particle in a buffer and η_0 is the viscosity of a buffer.

The collected data are presented in Fig. 4.9. The first thing we notice in Fig. 4.9 is that the nanoviscosity is not constant but depends on the size of the probe used in the experiments, analogous as it has been reported [8, 88]. The two probes: GFP and dextran 155 kDa, follow the trend: the greater value of the hydrodynamic radius, the greater the experienced viscosity inside the cells. The nanoprobe with a 1.33 nm radius is an exception to this rule. The possible explanation is that small molecules of dextran 4.4 kDa penetrate the cellular structure (and these structures hinder their movement), which are inaccessible to larger molecules (with a radius higher than 2 nm). Compared to that experienced by GFP protein, the increased effective viscosity is observed in the case of both types of cultures.

For two probes bigger than 2 nm in radius, it can be noticed that they experienced nanoviscosity, which is a bit lower when they probed the cytoplasm of cells within spheroids than the cytoplasm of 2D-cells. This difference is the greatest for the 8.60 nm probe. Nevertheless, the determined nanoviscosity values in both types of cultures are comparable within the errors.

Unfortunately, it was not possible to investigate the nanoviscosity experienced by probes bigger than 10 nm because, so far, there is no effective method for cells loading with big nanoparticles. However, I extended the FCS analysis to confocal imaging of cellular organelles.

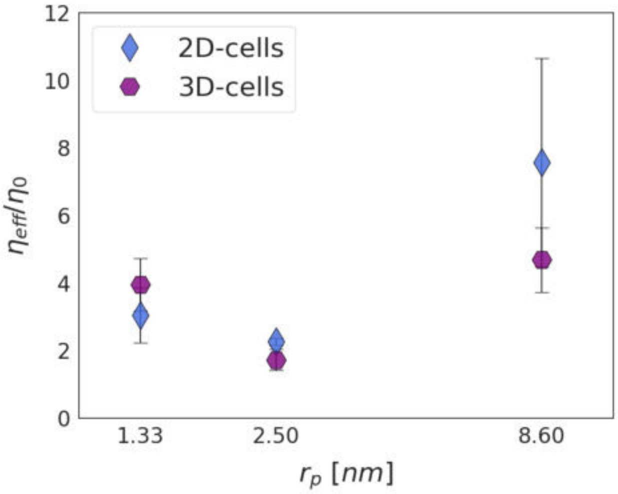

Figure 4.9: Comparison of nanoviscosity inside cells cultured as a monolayer (2D-cells) [8] and cells cultured as spheroids (3D-cells). Each point represents the average value obtained from at least 15 cells from two independent experiments. The probe with a hydrodynamic radius, r_p of 1.33 and 8.60 nm corresponds to TRITC-dextran 4.4 kDa and TRITC-dextran 155 kDa, respectively. The probe with a hydrodynamic radius of 2.50 nm is EGFP protein expressed in HeLa cells.

4.5 2D and 3D cells show differences in cytoplasm organization

Measurements of intracellular viscosity using FCS are limited to the spot in which the confocal volume is localised. The measured biomolecule mobility can produce drastically varied values depending on the chosen region inside the cytoplasm. For instance, it has been reported that diffusion of GFP molecules in intracellular compartments like endoplasmic reticulum can be 9-18 times lower than in water (and 3–6 times lower than in the cytosol) [89]. Even the increase of the number of different spots to 10 or 20 chosen to analyse within one cell can not reflect the actual, inhomogeneous structure of the cytoplasm. Furthermore, that is because the volume of a single HeLa cell is around 6900 μm^3 (determined based on the confocal imaging in NIS Elements software), while the effective detection volume in FCS measurement is approximately 0.3 μm^3 (estimated during the calibration procedure).

Hence, I extended the FCS analysis to confocal imaging and broadened the analysis region from a tiny spot to the whole organelles - microtubules and endoplasmic reticulum (Fig. 4.10) of HeLa cells cultured both in 2D and 3D condition. The imaging of chosen organelles can illustrate large cytoplasmic obstacles, which can be a source of differences in mobility studies. Moreover, imaging may reveal the potential difference in the cytoplasm structure and define the method of cell culture as an underlying factor that influences intracellular architecture.

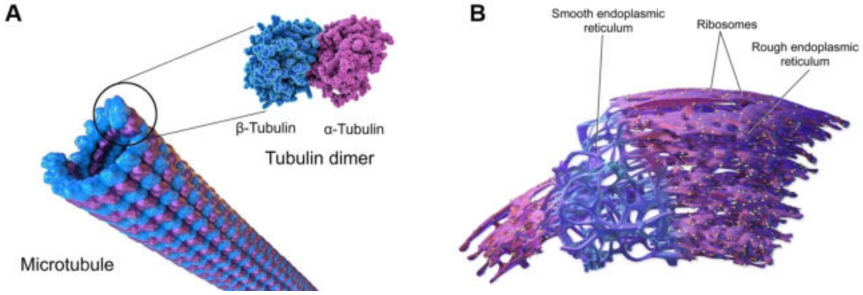

Figure 4.10: The structure illustrations of large cytoplasmic organelles: (A) microtubule [90], and (B) endoplasmic reticulum [91].

Microtubules

Microtubules are key components of the cytoskeleton. They are protein polymers that are long and tube-shaped (Fig. 4.10.A). Microtubules are crucial in intracellular transport, cell movement and, most importantly, they maintain the cell shape. As I already presented in Fig. 4.2, the method of cell culture influences their shape. So does the method of cell culture affect the organisation of the microtubule?

To address this question, I stained microtubules with Tubulin Tracker™ Deep Red - docetaxel[2] conjugated to a red fluorophore, which specifically labels polymerized tubulin, according to the protocol described in A.8. The confocal imaging of cells, both types of cultures, stained with docetaxel are presented in Fig. 4.11.

Microtubule staining revealed an extensive, well-organized microtubule network in cell cultured as a monolayer. In contrast, a cell within the spheroid had no clearly visible network of microtubule filaments, lacking a microtubule organizing centre. These observations reveal that *in vitro* culture condition of HeLa cells results in changes in the microtubule cytoskeleton arrangement.

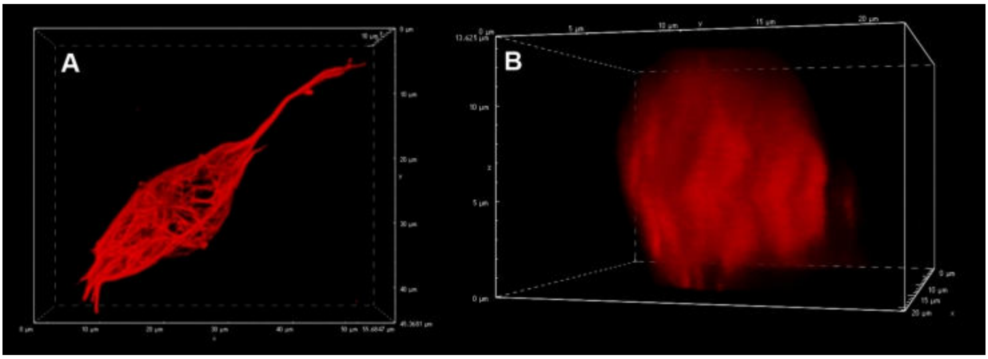

Figure 4.11: Microtubule staining in HeLa cells cultured as (A) monolayer (the image is presented from the cell bottom), and (B) spheroid. The Tubulin Tracker™ Deep Red was excited using a 635 nm laser.

Endoplasmic reticulum

The endoplasmic reticulum (ER) is an intracellular continuous membrane system (Fig. 4.10.B), which, above all, plays a crucial role in the synthesis, folding, modification, and transport of proteins. ER surrounds the nucleus

---

[2] Docetaxel is an antimicrotubule agent effective in the treatment of patients with breast cancer. The drug exerts its cytotoxic activity by promoting and stabilising microtubule assembly while simultaneously preventing microtubule depolymerisation. This results in inhibition of normal cell division [92].

and, in the form of membranous tubules, extends throughout the whole cell cytoplasm [93].
It was suggested that such a complex network of ER might be responsible for restricted nanoprobes diffusion within the cytoplasm, and, in consequence, its increased nanoviscosity [8, 94]. Interestingly, the abundance of the endoplasmic reticulum can differ between cell lines [8].

Here, I performed ER immunostaining of 2D and 3D-organized HeLa cells, in line with the procedure described in A.9. The confocal images (Fig. 4.12) revealed the distribution of ER structure within the cells. In cells cultured as a monolayer, the ER extends as a network throughout the entire cytosol. While, in cells within a spheroid, the endoplasmic reticulum is mainly localised around the nucleus (Fig. 4.12.B and Fig 4.13.A).
To support the outcome of ER distribution within 3D-cells, I presented, in Fig. 4.13, fluorescence and transmitted light images pair. The transmitted light image depicted the cell edges and enabled a conclusion that ER is not localised in the entire volume of the cell.

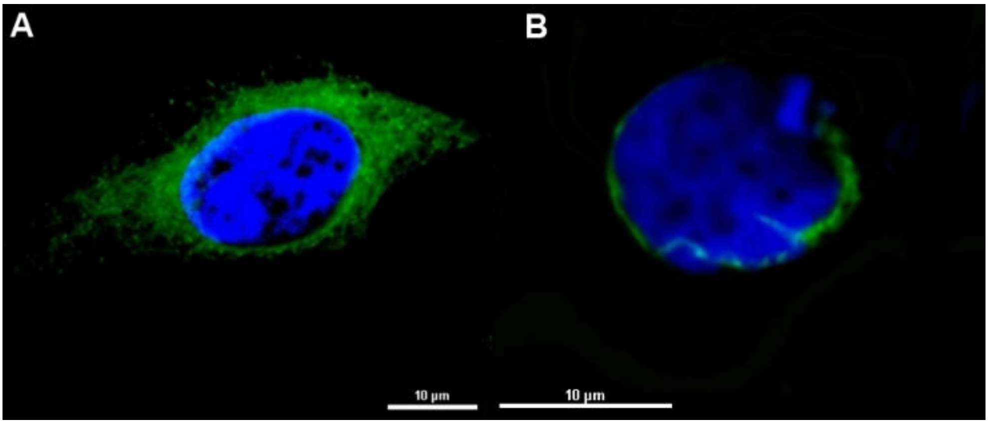

Figure 4.12: Endoplasmic reticulum immunostaining (in green) in HeLa cells cultured as (A) monolayer, and (B) spheroid. To detect the ER, I used a primary antibody directed against the ER-associated protein disulfide isomerase (PDI) and an Alexa Fluor 488 dye-labelled secondary antibody, excited using a 485 nm laser. It is also shown Hoechst 33342 nuclear counterstain (in blue), excited using a 408 nm laser.

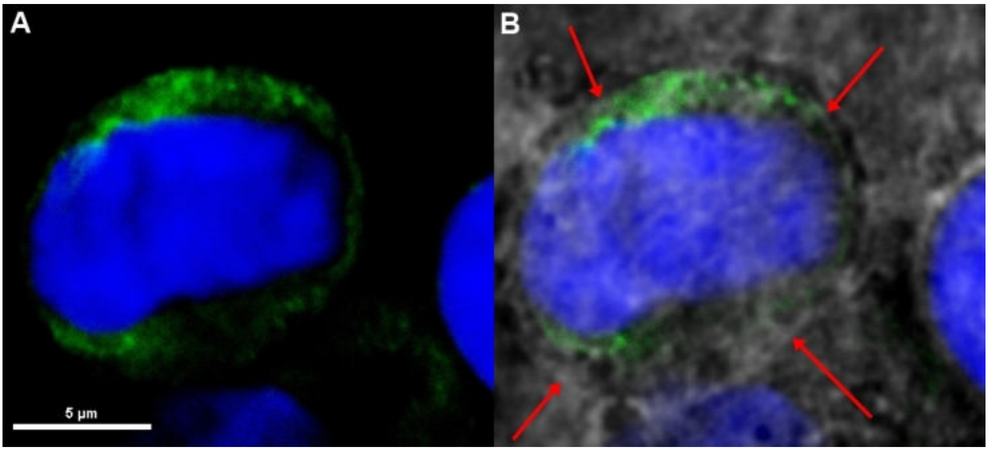

Figure 4.13: Fluorescence (A) and transmission light (B) images of a HeLa cell with stained ER (green) and nucleus (blue). The transmitted light image reveals the edges of the cell (marked with red arrows) and assists the analysis of ER distribution within the 3D-cell.

The diffusion rate, which governs intracellular reactions, is comparable between 2D and 3D organized cells. However, it seems that cells exhibit unlike internal structures depending on whether they live on a flat surface or in a tissue-like architecture. By confocal image analysis, I proved that the cell culture condition affects the difference in cytoplasm architecture - dissimilar microtubules organization and ER distribution. Such discrepancies in the intracellular organization undoubtedly affect molecular, cellular, and physiological processes [95].

4.6 2D and 3D cells show differences in PARP1 protein expression

As I already mentioned, cell culture condition have been shown to alert gene expression and protein synthesis [70, 73]. Proteomic analysis between cell culture as monolayer and multicellular spheroids [96, 97] demonstrated up/down-regulated proteins, which are mainly involved in energy metabolism, cell growth, cell structure, and cell-cell interactions.

It is perhaps not unexpected that cells grown in spheroids express more cell adhesion proteins (involved in binding cells with each other or with the extracellular matrix) than cells grown in monolayers. However, the reported changes between two types of cultures in the proteomic analysis include up-regulation of the protein involved in chemoresistance - gelsolin (GSN) [96, 98]. Gelsolin, by interacting with actin, directly influences cell migration, shape, and growth. Overexpression of gelsolin in breast cancer patients was linked to cancer stage and caused increased metastasis to lymph node [99]. The overexpression of gelsolin in 3D cell culture better reflects tumour *in vivo*. Hence, research on chemoresistance carried out with 2D cultures may lead to erroneous conclusions.

In my work, I demonstrate that fluorescence correlation spectroscopy can be successfully applied to estimate the expression level of PARP1 protein inside the monolayer-cultured cells and cells within spheroids. PARP1 - poly(ADP-ribose) polymerase - is responsible for repairing DNA single-strand breaks (SSBs) mediated via the base excision repair (BER) pathway. Inhibition of PARP1 blocks the BER pathway. Normal cells can restore DNA damages using alternative pathways, while in cancer cells (BRCA-mutated ovarian cancer cells), DNA damage accumulates, leading to cell death. Given PARP1 biological importance, it has become a promising target for cancer therapy [100].

Several PARP1 inhibitors are being studied, including olaparib (Lynparza™). Olaparib acts mainly as a selective inhibitor of the activity of PARP1 (and PARP2, member of the PARP family) by binding to the catalytic domain of PARP1 (or PARP2). As a consequence, the drug molecule inhibits the BER pathway and causes cell death (Fig. 4.14) [101, 102].

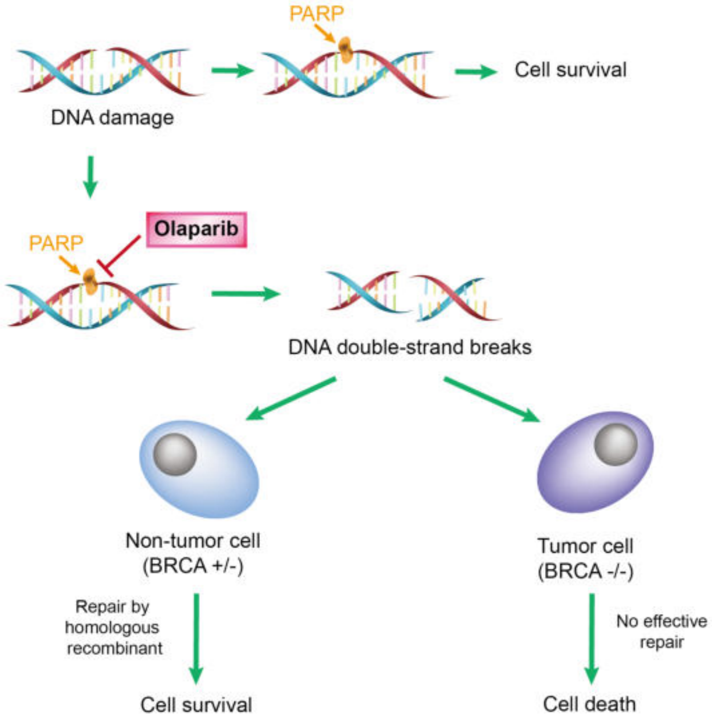

Figure 4.14: Inhibition of PARP prevents the PARP protein in cancer cells from repairing their damaged DNA, causing the cancer cells death [103].

The fluorescent analogue of olaparib - olaparib conjugated with the green fluorescent BODIPY-FL - PARPi-FL, has been synthesized [104], allowing FCS to be used in studies of olaparib interactions with PARP1 protein.

First, from the experiments in buffer, I determined the size of olaparib and the formed complex olaparib-PARP1 in a buffer (the obtained FCS curves are shown in Fig. 4.16). From the FCS experiments of the fluorescent analogue of olaparib alone, I determined its hydrodynamic radius equals $r_h = 0.65 \pm 0.03$ nm. I calculated r_h value, based on the FCS data, which I fitted using the normal diffusion model (Eq. 2.1, with $\alpha = 1$) and Stokes-Einstein relation (Eq. 2.4). Then, I performed the FCS measurements of the PARPi-FL and PARP1 mixture (in buffer). The obtained FCS curves, I fitted with the two-component normal diffusion model (Eq. 2.2). Again, from the Stokes-Einstein relation, I calculated the hydrodynamic radius of the formed olaparib-PARP1 complex, $r_h = 8.09 \pm 0.52$ nm. Having the values of hydrodynamic radius of olaparib and olaparib-PARP1 complex, we can use the cytoplasmic nanoviscosity curve [8, 17] to estimate the diffusion coefficient of the drug and olaparib-PARP1 complex in the HeLa cells. The predicted values of diffusion coefficients allow ascertaining the correctness of results obtained in the cells cytoplasm (Tab. 4.1). The experiments with the use of fluorescent analogue olaparib in cells were carried out as follows. A day before the experiments, HeLa cells were seeded on a glass-surface dish (Cellvis, USA). Then, I added the drug to the adherent cells (to a final concentration of 20 nM), incubated the cells with the drug for 30 minutes, and performed FCS measurements and confocal imaging. The confocal fluorescence images of adherent cells, as well as spheroids, incubated with olaparib, demonstrate its rapid accumulation inside the cells, regardless of the type of cell culture (Fig. 4.15).

The obtained FCS data, analysed with the three-diffusion component diffusion model [3] revealed the diffusion values of olaparib and complex of olaparib-PARP1 inside HeLa cytoplasm. The experimental values are in good agreement with those predicted from the nanoviscosity curve (Tab. 4.1).

Table 4.1: The diffusion coefficient values of olaparib and olaparib-PARP1 complex predicted from the nanoviscosity curve [8, 17] and measured inside the cytoplasm of HeLa cells.

The diffusion coefficient values of:	**olaparib**	**olaparib-PARP1**
predicted $[\mu m^2/s]$	~ 260	~ 7.60
measured $[\mu m^2/s]$	242.32 ± 40.52	6.76 ± 1.85

---

[3] I also observed the third component in FCS data, which with a strong likelihood corresponds to the big olaparib-PARP1-mRNA complex.

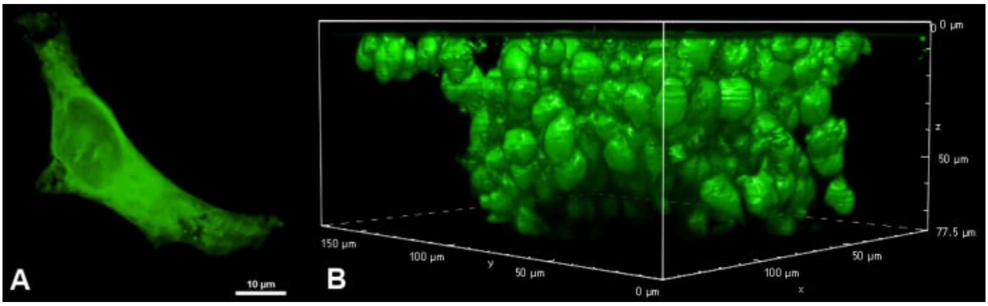

Figure 4.15: The confocal images of HeLa cells cultured as (A) monolayer and (B) spheroids after 30 minutes of incubation with PARPi-FL (green fluorescence excited with a 488 nm laser). The external concentration of the drug was around 500 nM.

In the next stage, I conducted the experiment with HeLa spheroids, generated based on the already presented procedure (Fig. 4.6). Then, I added the drug to spheroids (to a final concentration of around 20 nM), incubated the cells with the drug for 30 minutes and performed FCS measurements. I analysed the results, similarly as in the case of the adherent cells, using the three-diffusion component diffusion model. The calculation gave similar values of the diffusion coefficients (all of the three fractions) like in the case of HeLa cells cultured as a monolayer (Fig. 4.16). Since the measured diffusion coefficient of the olaparib-PARP1 complex did not differ significantly, the results support the hypothesis that cellular nanoviscosity in both methods of culture is comparable. However, what surprised me was an approximately twofold higher intracellular concentration of PARPi-FL in spheroids than in adherent cells with the same external concentration of the drug.

The relation between intracellular (c_{inside}) to extracellular drug concentration ($c_{outside}$) can be expressed as the partition coefficient, K:

$$K = \frac{c_{inside}}{c_{outside}} \tag{4.2}$$

The partition coefficient refers to the ratio of chemical distribution between two phases at equilibrium. Usually, the parameter is used to quantify the

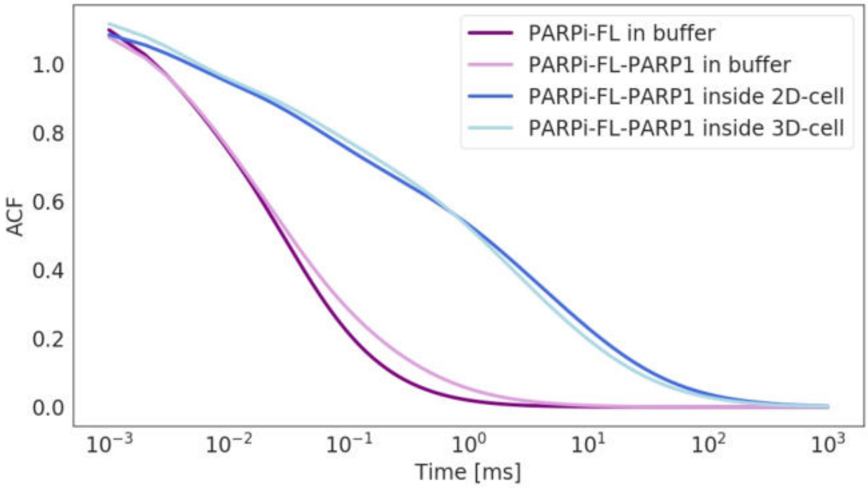

Figure 4.16: The normalized FCS curves of PARPi-FL and complex formed with PARPi-FL and PARP1 in PBS buffer and inside the cytoplasm of cells cultured in 2D and 3D conditions. The diffusion time of PARPi-FL increases upon complex formation with PARP1. The complex diffuses markedly slower inside cells than in PBS buffer.

distribution of a drug between tissues, and plasma [105, 106]. Here, the parameter reflects the extent of both intracellular binding and penetration effectiveness of a drug. The partition coefficient of a value higher than 1 indicates the accumulation of a drug inside the cell.

In my studies, I calculated the partition coefficient for olaparib by measuring the extracellular and intracellular concentrations of the drug both in adherent cells and cells within spheroids [4] for varying external concentration of the inhibitor. The results are presented in Fig. 4.17. The K values do not depend on the external concentration of the olaparib

---

[4] In purpose to avoid the increase of the effective volume by scattering of the laser beam, which can cause a higher number of molecules inside the detection volume (as I described this artefact in the section 2.5), the intracellular measurements were limited to a maximum second layer (counted from the glass, around 20 μm) of cells within spheroids. I also performed a test, by measuring the intracellular concentration in three consecutive layers of cells - the obtained values of concentrations were almost the same. Hence, we can be sure that the measured higher concentration of molecules in 3D cultures is not related to the increase in the detection volume.

(in the examined, nanomolar range of concentration) and have higher values for cells in 3D cultures, indicating higher intracellular concentration. The increased concentration of olaparib in cells cultured as spheroids is most likely due to the increased number of targets to which olaparib binds, implying PARP1 downregulation in adherent cells as compared to cells within spheroids. This observation is consistent with the results presented in the article by Kopp [107]. The demonstrated gene expression of PARP1 in MCF-7 cells was around 1.5 times higher in spheroids than in adherent cells. The reason for PARP1 overexpression in 3D cell culture is unknown. Nevertheless, it is known that levels of PARP1 differ between the cancer cell lines [108] and high expression of PARP1 is associated with a poor prognosis in early breast cancer [107].

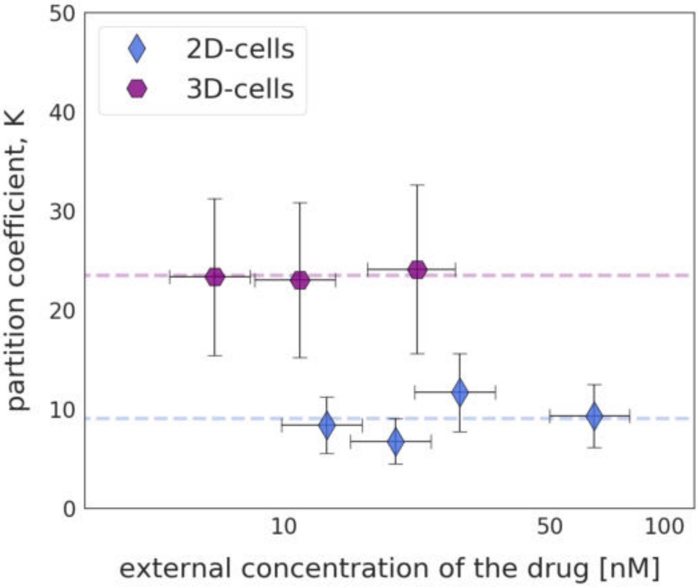

Figure 4.17: The ratio of intracellular to extracellular drug concentration (partition coefficient, K) does not change with the increase of the external drug concentration. The intracellular drug concentration is lower in cells cultured as a monolayer (2D-cells) than cells within spheroids (3D-cells).

4.7 Further directions

The differences in the intracellular structure between cells cultured on the flat surface or in the tissue-like architecture described in this chapter should prompt more research to study the potential distinct molecular and cellular behaviours. Particular attention should be taken to the research on therapeutic agents' action on a cellular level and their interactions with intracellular structures. It would provide a better knowledge of drug action and resistance mechanisms *in vivo*, allowing for the development of better therapeutic agents before starting the final stage of clinical trials.

Synthesis of the fluorescent analogue of drugs is a big step toward extending the range of methods to investigate therapeutic agents using imaging technologies or advanced fluorescent-based techniques. The example of PARPi-FL proved that in a relatively easy way, by using FCS, we can determine intracellular drug concentration with the determination of the drug fraction bounded to the target and structures of the formed complexes with the drug. Not only in adherent cells but also in cells within spheroids. The study in cells within spheroids pointed to the increased accumulation of olaparib very probably related to the higher number of drug targets.

In the case of another drug, eribulin, the quantitative analysis with the use of 2D and 3D cell cultures will most likely also give different outcomes. Eribulin is a microtubule inhibitor, which in 2010 was approved by the U.S. Food and Drug Administration as a third-line treatment of metastatic breast cancer. The drug exerts its cytotoxic effects by interfering with microtubule dynamics. It binds to the β-tubulin subunits (Fig. 4.10.A) and induces the non-functional tubulin aggregates [109]. The presented in Fig. 4.11 differences in microtubule organization between 2D and 3D cell cultures suggest a potentially different response to the drug.

The study of these possible differences across types of cell cultures using FCS can be done by employing the fluorescence derivative of eribulin -

eribulin conjugated to BODIPY fluorophore (eribulin-BFL) [110]. The eribulin-BFL is not available commercially, but its synthesis can be done using the reported procedure. In Fig. 4.18 are presented the confocal images of HeLa cells exposed to eribulin-BFL synthesised in our laboratory. The drug easily penetrated the cells and accumulated in the cytoplasm. The preliminary FCS experiments, in which I measured the diffusion time of the drug in a buffer, revealed its hydrodynamic radius equals to $r_h = 1.12 \pm 0.26$ nm.

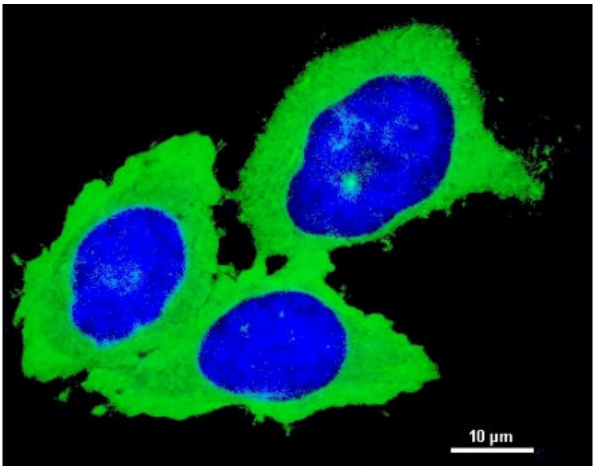

Figure 4.18: The confocal image of HeLa cells exposed to eribulin-BFL (green fluorescence excited with a 488 nm laser) was synthesised in our laboratory based on [109]. The cells nuclei were stained by Hoechst 33342 (blue fluorescence excited with a 405 nm laser).

Considerably, a lot of work will need to be done to verify the presented hypothesis about the difference in quantitative parameters describing the eribulin intracellular interactions within 2D and 3D cell cultures. However, the developed methodology will aid in data collection and analysis. Undoubtedly, it will be a fruitful area for further research.

4.8 Conclusions

Despite many studies using three-dimensional cell cultures, the measurements of the intracellular macromolecule mobility inside spheroids have not been reported yet. This indicated a need to establish a procedure for spheroids preparation that would be suitable for the FCS application. In my work, I demonstrated the methodology of spheroids usage in FCS experiments, free from the potential errors in the collected data.
The devised procedure allowed me to probe the cytoplasm of cells within spheroids and compare the results with those obtained for the adherent cells. The nanoviscosity, an important structural parameter that governs intracellular reaction rates, is comparable within the errors in both types of cultures.

The possible data deviations between 2D and 3D cultured cells result from the differences in the cytoplasm organisation, demonstrated by the staining and imaging of two big cytoplasmic organelles: microtubules and endoplasmic reticulum. The flattening of cells growing on the surface affects their internal structure. The adherent cells have an extensive, well-organised microtubule network and endoplasmic reticulum extended throughout the entire cytosol. This image is so widespread that it may be attributed to the actual internal structure of cells present *in vivo*. However, the cells in the tissue-like architecture lack a microtubule centre, and ER is mainly localised around the nucleus.

The different intracellular structures between the 2D and 3D cells, corresponding to the molecular composition of the cells, can also be noted. I found that PARP1 protein, targeted in anticancer therapy, is overexpressed in three-dimensional cell cultures. The reason for PARP1 up-regulation is unknown, but it implies a different response to the treatment and probably better reflects the expression of PARP1 in tumour *in vivo*.

Taking together, this chapter is a perfect example showing the versatility of the FCS method. The technique can be applied to living cells, also cultured as spheroids, revealing their nanoviscosity. We can examine the intracellular drug interactions with the determination of the drug fraction bound to the target and structures of the formed complex. Additionally, the size of the formed complexes with the drug can prove its selectivity. In the case of high affinity to the target, we can establish the abundance of proteins, undoubtedly affecting the cells' function and response to treatment.

5

Structure of the extracellular matrix

Contents

The therapeutic efficacy of drugs in chemotherapy depends on their ability to reach cancer cells by effective penetration into tissues. The penetration of drugs is affected by their physicochemical properties (e.g.

size and electrical charge) and the complex physiology of the tissue. Tumours consist of cancer cells and a non-cellular component - the extracellular matrix (ECM) [111, 112]. It has been demonstrated that ECM is a physical barrier hindering efficient drug penetration [113]. Despite the ECM's importance in drug delivery, there remains a lack of studies on the ECM structure and its impact on macromolecule mobility.

This chapter presents the multicellular spheroids as models providing the extracellular matrix to examine its nanostructure by means of FCS. The mobility studies allowed me to generate the length-scale dependent viscosity profiles of extracellular matrix within spheroids, which lay the foundation for modelling drug penetration through tissues.

5.1 Introduction

Therapeutic agents to reach cancer cells in a tumour must make a quite long way. Once a drug is injected into the bloodstream, it is distributed within vessels. Then, as shown in Fig. 5.1, a drug needs to pass across the microvascular wall and move through interstitial space to reach tumour cells located distal to blood vessels (in dependence on vascularization, which is a function of tumour size, the intercapillary distance is in a range from 49 μm to 304 μm [111]). The interstitial space of tumours, in general, is very extensive and encompasses 6-40 % volume of a whole tumour [114]. One type of drug movement through the interstitial spaces is diffusion [113]. The diffusion process becomes noticeably ineffective for ever-larger drug molecules and thus limits their therapeutic effectiveness. The development of big therapeutic molecules such as liposomes or nanoparticles (with a diameter of over 130 nm) indicates a need to understand how size affects their transport through the extracellular matrix. In order to describe the motion within ECM, it is crucial to identify the extracellular constituents and characterise their role in slowing down the diffusion process.

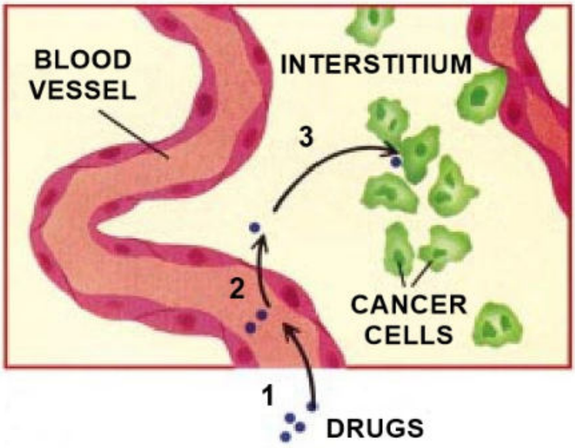

Figure 5.1: Drug delivery involves three processes: (1) Distribution of drugs via blood vessels; (2) Transport of drugs across the microvascular wall; (3) Transport of drugs through interstitial space to cancer cells [115].

5.2 The extracellular matrix

The extracellular matrix is the non-cellular component present in all tissues and organs. Beyond providing structural support, the ECM regulates a variety of functions including cell growth, migration, differentiation, survival and morphogenesis [116]. Among over hundreds of ECM macromolecules [117], we can distinguish two main classes of macromolecules: proteoglycans (PGs) and fibrous proteins.

Proteoglycans consist of a core protein linked to long carbohydrate chains. These simple definitions encompass an extensive large range of structures involving different core proteins, different classes of chains, and different numbers and lengths of individual chains. Typically, proteoglycans are components of extracellular spaces in which they form large multimolecular aggregates with collagens or hyaluronan, responsible for the compressive resilience of the tissue [118, 119].

Fibrous proteins are a major constituent of the extracellular matrix. The main fibrous ECM proteins are collagens, elastins, fibronectins and

laminins. These macromolecules are essential in the maintenance of both the structure and function of the tissues.
The most abundant fibrous protein is collagen, which constitutes up to 30% of the total protein content. Collagen type I molecule has the form of a triple helix of the length of about 300 nm and a diameter of about 1.5 nm. In the interstitium, collagen molecules bind together and form fibrils. The diameter of the fibrils is up to $\sim$500 nm. The primary function of collagen is to provide mechanical support and maintain the integrity of the tissues [120].

Collagen is associated with elastin. The elastin fibre resembles a random network of polypeptide chains infrequently crosslinked [121]. Elastin has a high degree of reversible distensibility, which means it can deform to vast extensions with very little force, allowing the tissue to be flexible [118].

Fibronectin and laminin, non-collagenous extracellular proteins, play important roles in many cell-surface interactions. These macromolecules can participate in various functions by using different specialized domains or peptide recognition sequences for binding to specific cell surface receptors or to collagens, proteoglycans, or other extracellular molecules. Fibronectin and laminin have critical roles in both cell adhesion and cell migration [118].

All mentioned extracellular components create a highly complex network, which impedes the movement of macromolecules. The mobility studies of macromolecules within the ECM-like systems found that diffusion is slower in the collagen gel with smaller mesh size (as a function of collagen concentration), which is an intuitive outcome. However, the gels of collagen and hyaluronic acid (at the same total concentration of proteins) generated a higher resistance to macromolecular diffusion than gels of collagen, or hyaluronic acid alone [122]. This outcome suggests that not only the total protein contents contribute to the diffusion of the molecules, but above all, the collagen organization and the matrix composition [123].

5.3 Models of the ECM

In cancer research, it is imperative to acquire knowledge about macromolecular anticancer agents' penetration effectiveness and their pharmacokinetics. A proper model is required to respond to this need that imitates the architecture of the tumour interstitium.

A lot of studies as a model of the ECM using the collagen gel [124–126]. Although this approach is simple and common, it does not reflect the ECM's natural complexity and composition. As I mentioned before, the diffusivity of molecules is highly dependent on the matrix composition. More precisely, it was determined that BSA (bovine serum albumin) had a diffusion coefficient of 16.4 $\mu m^2/s$ in 30 mg/ml collagen gel and 32.1 $\mu m^2/s$ in 30 mg/ml hyaluronic acid. While in the mixture of 20 mg/ml collagen and 10 mg/ml hyaluronic acid it was 14.2 $\mu m^2/s$ [122].
For this reason, a better approach seems to be applying the matrix of proteins mixture such as the commercially available Matrigel® or Cultrex®. The use of Matrigel proved that diffusion in the matrix depends not only on steric effects but also on interactions between the ECM and probes [127]. However, the problems with Matrigel are that the composition of the matrix is not precisely determined, and that there is batch-to-batch variation [128].

In my approach as a model of the ECM, I used multicellular spheroids. In the spheroids, cancer cells were found to produce extracellular matrix that is very similar to the ECM present in an *in vivo* tumours [129, 130]. To prove the presence of the ECM within spheroids, I performed immunohistochemical staining of four major extracellular matrix components: collagen type I, fibronectin, elastin, and tenascin-C. The results are presented in the next section.

5.4 Confocal imaging of the ECM

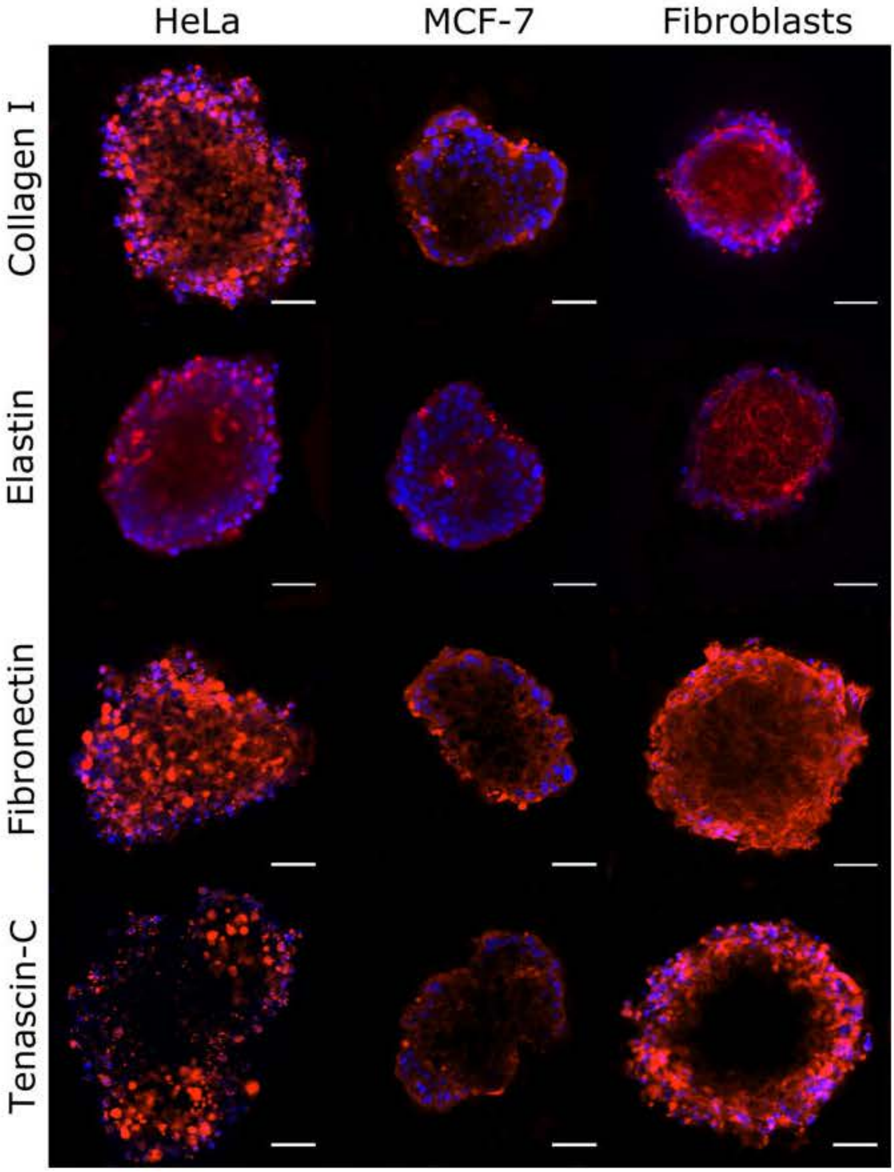

Figure 5.2: Immunochemistry analysis of the ECM molecules (in red): collagen I, elastin, fibronectin, and tenascin-C was performed on HeLa, MCF-7, and Fibroblasts spheroids. Hoechst 33342 nuclear counterstain also shown (in blue). Scale bar is 50 μm [10].

I used three types of spheroids in my studies, which were created using various cell lines: HeLa, MCF-7, and fibroblasts. The spheroids were generated following the protocol presented in Fig. 4.6. Then, using 5-day-old spheroids, I performed immunostaining (as described in A.10) to visualize the extracellular molecules: collagen type I, fibronectin, elastin, and tenascin-C. Collagen and elastin represent fibrous proteins, while fibronectin and tenascin-C constitute glycoproteins.

The immunostaining analysis, presented in Fig. 5.2, revealed that spheroids are not only aggregates of cells but contain a complex ECM. Based on the presented results, we can also notice the differences in particular protein abundance between cell lines. MCF-7 spheroids secreted significantly fewer ECM molecules than HeLa or fibroblast spheroids.

The depicted extensive structure of the ECM undoubtedly slows down diffusion of molecules in the extracellular spaces. In order to provide a quantitative description of transport within the ECM, I applied FCS.

5.5 FCS in the extracellular matrix

In the previous chapter, I successfully employed FCS to study the intracellular mobility of molecules within spheroids. Here, I used FCS to study molecules diffusion in extracellular spaces within spheroids.

The application of fluorescence correlation spectroscopy for the study of diffusion in the ECM of spheroids has already been made in two works [37, 131]. Reitan et al. [131] measured the diffusion coefficients of three probes 150 kDa IgG, 155 kDa dextran and 2 MDa dextran in solution, 5% gelatin hydrogel and OHS (human osteosarcoma cell line) multicellular spheroids. Authors demonstrated that FCS measurements provide equivalent findings to those obtained by another method - FRAP (fluorescence recovery after photobleaching) and thus confirmed the suitability of FCS for measuring diffusion of macromolecules extracellularly in spheroids.

The study conducted by Leroux [37] I already cited in section 2.5, describing the impact of complex systems on FCS experiments. The analysis demonstrated the dependence of the depth of the detection volume in spheroids on obtained FCS data, suggesting the maximum depth of measurement to 50 μm.

Strikingly, despite the importance of mobility studies in the ECM and the absence of reported contraindications to using FCS in spheroids, there remains a lack of systematic studies on diffusivity in extracellular spaces of tumour models. To address this need, I conducted research on the diffusion of nanoprobes with a radius ranging from 1 nm to over 100 nm in the ECM of spheroids made from three various cell lines (HeLa, MCF-7 and fibroblasts) [10]. The length-scale dependent viscosity model [67, 88] can be used to describe the mobility of nanoprobes in a dense network of the ECM. The model uses the already mentioned fluctuation-dissipation theorem to determine the effective viscosity η_{eff} experienced by a molecule in the ECM from the measurements of its diffusion coefficient, D:

$$\frac{\eta_{eff}}{\eta_0} = \frac{D_0}{D} \tag{5.1}$$

where D_0 stands for the diffusion coefficient of a given particle in a buffer and η_0 is the viscosity of a buffer.

The model is used to describe the changes occurring in the effective viscosity experienced by the particle diffusing in a complex system and, importantly, to characterize this system, as shown in Fig. 5.3:

$$ln\left(\frac{\eta_{eff}}{\eta_0}\right) = ln(A) + \left(\frac{\xi^2}{R_h^2} + \frac{\xi^2}{r_p^2}\right)^{-a/2} \tag{5.2}$$

where η_{eff} is the viscosity experienced by the nanosized probes in the ECM, η_0 is the viscosity of the solvent (i.e. the buffer), A is a constant of the order of 1, ξ is the correlation length – a mean half-distance between the entanglement points in a polymer matrix, R_h is the hydrodynamic radius corresponding to the size of polymer coils creating the environment, and r_p is the hydrodynamic radius of the probe. Exponent a is a constant of the order of 1.

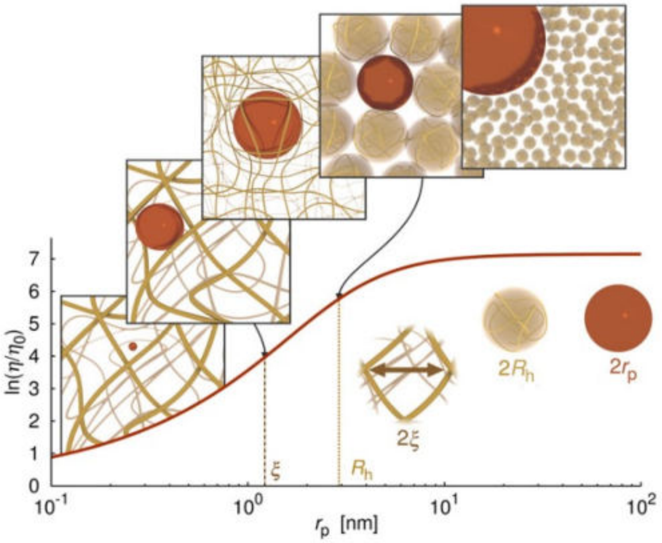

Figure 5.3: A plot illustrating the effective viscosity experienced by a probe of radius r_p diffusing through a complex system. The figures above the theoretical curve depict the mobility of a probe of different sizes (r_p) through the polymer network and relate the probe's size to the complex liquid's characteristic length-scale (ξ and R_h). Probes with $r_p \ll \xi$ experience viscosity that is quite similar to the viscosity of the solvent (a buffer). The molecules with a radius of $r_p > 4R_h$ experience the macroscopic viscosity of the system [88].

Once determined for a particular system, the length-scale dependent viscosity model may be used to predict the motion of the any-sized molecule. The procedure for determining the viscosity curve of the ECM is depicted schematically in Fig. 5.4.

For the purpose of studying the ECM structure within spheroids, I generated them in a manner similar to that described in 4.3, according to the protocol schematically depicted in Fig. 5.5. On the fourth day of culture, spheroids were carefully transferred onto the 8-chamber cover glass Lab-Tek™ (ThermoFisher Scientific, USA) slide. The nanoprobes were introduced into the ECM 24 hours before the FCS measurements

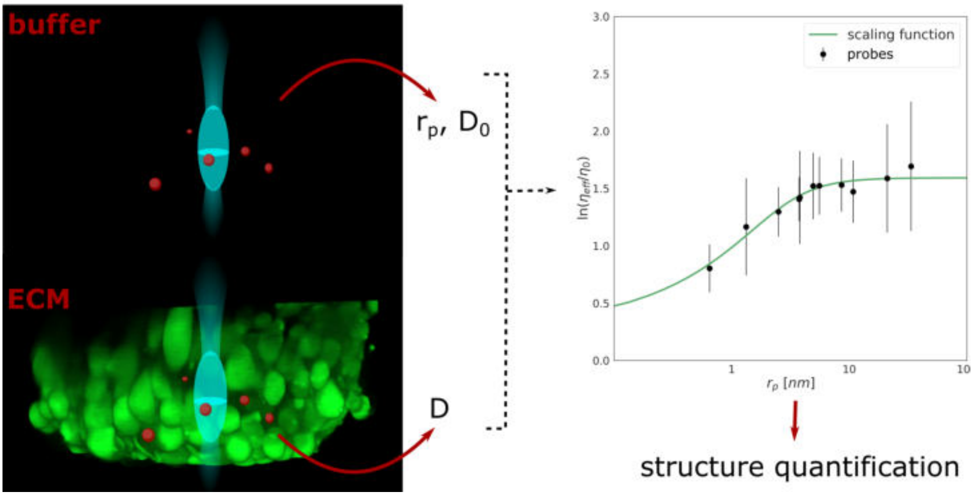

Figure 5.4: The schematic representation of the ECM structure quantification procedure. First, an FCS is used to calculate the radius and diffusion coefficient of nanoprobes in the buffer. The FCS experiments are then carried out in the ECM of spheroids utilizing the same molecules. The data are collected and fitted with the length-scale dependent viscosity model (Eq. 5.2). The model interpretation provides parameters characterizing the structure of the ECM.

by adding them to the cell culture medium to a final concentration of around 100 nM.

To conduct FCS experiments in spheroids' ECM, the detection volume must be precisely localised in extracellular regions. This is accomplished by using the microscope's imaging mode. Fig. 5.6 depicts an example image of a cross-section of a spheroid to illustrate the positioning procedure. The exclusion of cellular space was first significant. The cellular autofluorescence (excited by a 485 nm laser) facilitates cell localisation and reveals their edges. The blue laser was only utilised for cell localisation and was then turned off. Simultaneous 561 nm laser excitation of probes revealed the extracellular regions. Spheroids with well-defined extracellular and cellular areas allowed for further adjustment of the three axes.

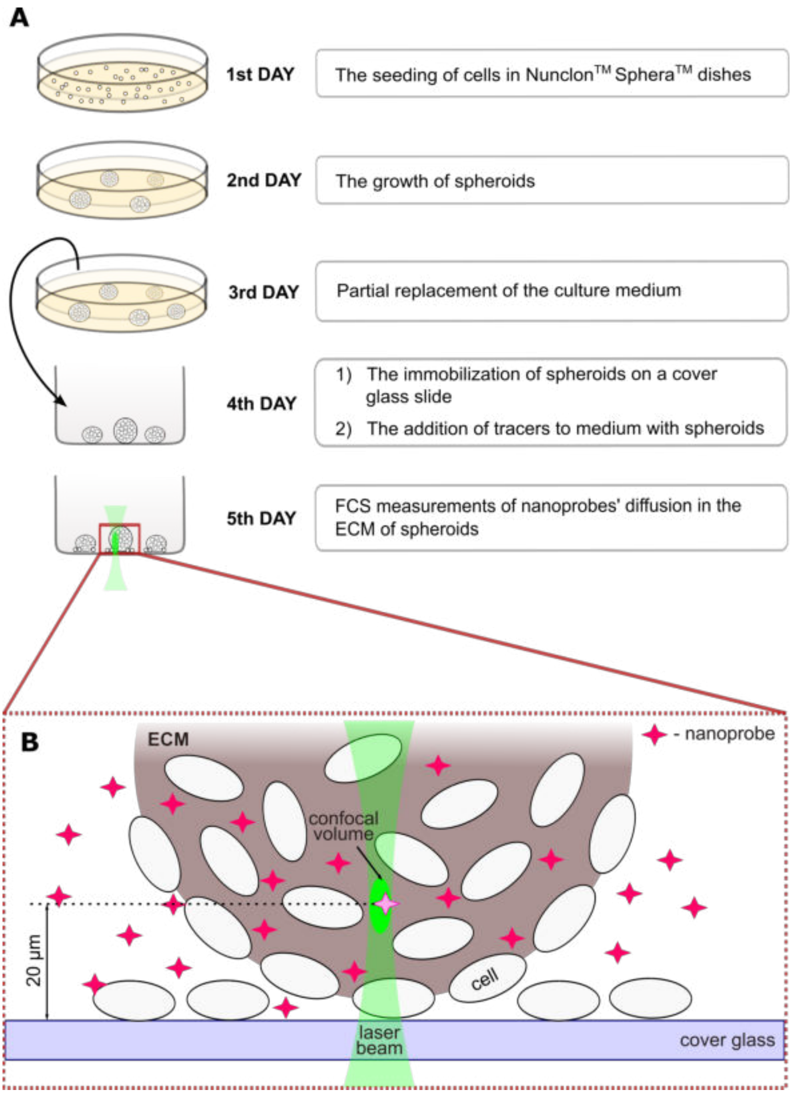

Figure 5.5: **A**. Scheme of the procedure for spheroid culture and their preparation for the measurements. Experiments were carried out with 5 day-old spheroids when they reached 400 -600 μm in diameter. **B**. The confocal volume is positioned in the ECM of a spheroid, and FCS measurements are performed [10].

Due to previously reported scattering of light by successive layers of cells within spheroids (2.5), I positioned the confocal volume at the maximum depth of 30 μm inside spheroids (corresponding to the third layer of cells). Finally, I chose the location of the detection volume from the cells' edges at 2-10 μm by moving the X-Y stage. I attempted to make this distance from the cell as little as feasible to prevent free extracellular space and as large as feasible to avoid placing the detection volume in close proximity to the cellular membranes. This procedure provided me with the assurance that the measured signal originates from nanoprobes diffusing in the extracellular matrix rather than from inside cells.

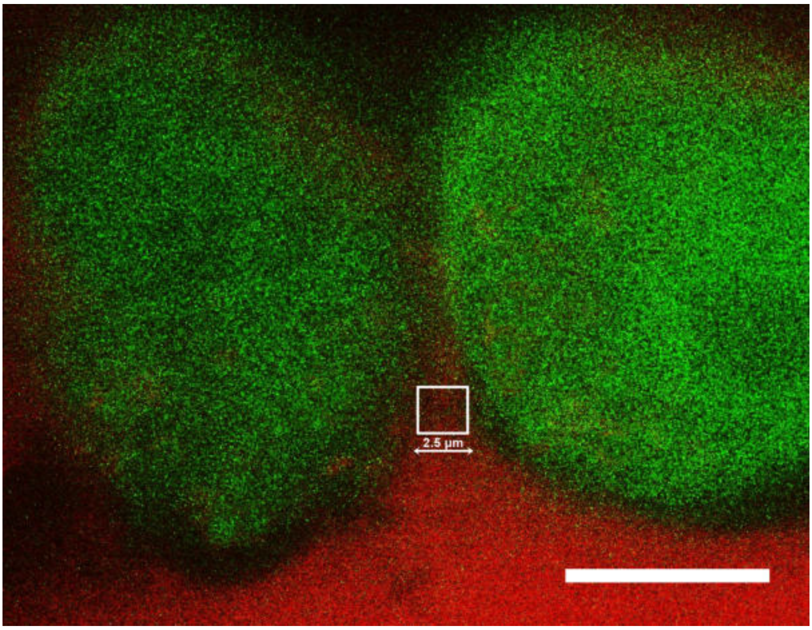

Figure 5.6: The positioning of the confocal volume within the ECM of spheroids at 30 μm depth. I employed the HeLa-EGFP cell line exclusively for the purpose of clear imaging (in proper experiments, I used cells lines without the expression of fluorescent proteins). The green fluorescence signal is emitted by HeLa cells expressing EGFP, while the red fluorescence signal comes from TRITC-dextran 155 kDa molecules in the extracellular matrix. The white box illustrates an example location of the ECM selected for FCS measurements. The focal volume was positioned at a reasonable distance from the cellular membrane. Therefore, the molecules which are inside the cells (in the case of nanoprobes uptake by cells through endocytosis or pinocytosis) do not alter the FCS measurements in the ECM. If there were any extracellular areas with bright spots (which corresponded to aggregates of molecules) present, I avoided them in the measurements. The scale bar is 10 μm [10].

After setting the appropriate site for the confocal volume in the imaging mode, I switched the detection path from directed at the confocal detector to directed at the FCS detector. The applied laser power was at the level of 15-25 μW.

5.6 Fluorescent tracers

The extracellular spaces were probed with fluorescent nanoprobes with a radius from 1 to over 100 nm, encompassing the size of most therapeutic agents used in cancer treatment. I used TRITC-dextrans and PEG-coated fluorescent silica nanoparticles filled with rhodamine B, custom-synthesised by Siliquan (Siliquan, Poland). Listed nanoparticles along with their radii are presented in Tab. 5.1.

Table 5.1: Nanoprobes used in the experiments and their values of radius.

Sample name	r_p **[nm]**
TRITC-dextran 4.4 kDa	1.3 ± 0.2
TRITC-dextran 20 kDa	3.8 ± 0.3
TRITC-dextran 40 kDa	4.9 ± 0.5
TRITC-dextran 155 kDa	8.6 ± 0.7
PEG coated S34(1) silica nanoparticles	20.6 ± 1.3
PEG coated S43(2) silica nanoparticles	66.2 ± 3.1
PEG coated S44(3) silica nanoparticles	110.7 ± 3.3

The physical properties of the nanoparticles, such as their charge and density, may have an impact on mobility measurements.

Dextrans are neutral molecules. The degree of substitution of TRITC in dextran ranges from 0.001 to 0.008. The charge contribution from the tertiary amino groups on the rhodamine moiety is negligible at these low degrees of substitution. In the case of silica nanoparticles, they are coated with neutral surface charge polyethylene glycol (PEG). The neutral charge of all used nanoprobes eliminates the possible interaction with extra- and intracellular components.

The below considerations prove that due to the low density of silica, the measured motion of the nanoparticles in the ECM of spheroids results from their Brownian motion and is not altered by the sedimentation process.

The main competing forces acting on the motion of an individual uncharged particle in a viscous fluid are gravity, buoyancy and hydrodynamic drag. For a spherical particle, sedimentation force (gravity and buoyancy) are given by:

$$\vec{F_g} = \frac{4}{3}\pi r_p^3(\rho_p - \rho_f)\vec{g} \tag{5.3}$$

where ρ_p is the density of the particle, ρ_f is the density of the fluid, r_p is the particle radius, and g is the acceleration of gravity.

The hydrodynamic drag (for small Reynolds numbers) on a spherical particle is given by:

$$\vec{F_d} = 6\pi\eta r_p\vec{v} \tag{5.4}$$

where η is the viscosity of the fluid, and v is particle velocity.

A force-balance of gravity, buoyancy and hydrodynamic drag yields the sedimentation velocity of a single particle sedimenting in the fluid of viscosity η as:

$$v = \frac{2r_p^2(\rho_p - \rho_f)}{9\eta} \tag{5.5}$$

The sedimentation speed depends on the physical properties of a particle – its size and density. In addition to motion related to settling of particles, stochastic motion occurs and is characterised by a self-diffusion coefficient, which does not depend on the density and is the same for any (i.e. carbon, silica or gold) same-sized nanoparticles:

$$D = \frac{kT}{6\pi\eta r_p} \tag{5.6}$$

Where k is the Boltzmann constant, $T(K)$ is temperature. The diffusion coefficient is defined by the mean square displacement:

$$\left\langle x^2 \right\rangle = 6Dt \tag{5.7}$$

To estimate how the density of particles affects the calculation of effective viscosity, I consider which effect dominates - the molecular displacement due to the sedimentation of particles or due to Brownian motion?

The missing parameter to estimate the exact value of sedimentation velocity is the density of the fluid ρ_f – in our case, the density of the extracellular matrix. Here, we assume the density of water, $\rho_f = 997 kg/m^3$, the actual (for sure higher) density value will increase the sedimentation velocity, since $v \sim \Delta\rho$.

If we consider silica nanoparticles ($\rho_p = 2650 kg/m^3$) with radius r_p=111 nm (the biggest nanoprobe used in experiments) moving in the ECM of HeLa cells whose viscosity I found to be $\eta_{macro} = 3.32 mPas$ (more details in the next section, 5.7), the sedimentation speed is approximately $13 nm/s$. Therefore, during the 120 seconds (the time of data acquisition) the particle will cross a distance of $L = 1.6 \mu m$ ($L = vt$). At the same time, the root mean displacement x of the same nanoprobe resulting from Brownian motion (the determined from experiment diffusion coefficient equals to $D = 0.66 \mu m^2/s$) is around 22 μm. We can clearly see that $x > L$ and the sedimentation does not influence our probes' Brownian motion.

Since carbon nanoparticles have a similar density (ρ_p=2260 kg/m^3) as silica nanoparticles, the sedimentation is also negligible. In the case of gold nanoparticles ($\rho_p = 19320 kg/m^3$) with the same radius, moving in the same environment, the sedimentation velocity is $148 nm/s$. After a time t=120 s, the molecular displacement resulting from settling equals 18 μm – it is a comparable distance with the root mean displacement resulting from diffusion, $x \sim L$.

To conclude, the physical properties of nanoparticles, such as density, may contribute to their transport properties. However, in the case of silica nanoparticles used in our experiments, diffusion was a prevailing process, and, as a consequence, the calculation of effective viscosity was done correctly [10].

Another problem that can arise in relation to nanoparticles is their cytotoxicity. All the probes used in the study can be uptaken by cells through endocytosis or pinocytosis. Nevertheless, the cellular uptake of the tracers in no way interferes with the measurements of their self-diffusion in the extracellular space. The only consequence of the penetration of nanoparticles into cells was their lower concentration in the ECM. To avoid a too low fluorescence signal, the increased concentration of nanoprobes was added to the medium with spheroids (to a final concentration 100 nM). Since FCS enables an estimate of the concentration of fluorescent particles in the sample, I additionally quantified the cellular uptake from the relation 2.5, which was around 90 nM of nanoprobes.

In the assessment of nanoprobe cytotoxicity, apart from their concentration, time of exposure is an important parameter. In the experiments, nanoprobes were added a maximum of 24 h before FCS experiments, which took another 8 h.

In order to examine the cytotoxicity of nanoprobes, I performed an MTT assay in accordance with the protocol described in A.11. The MTT (3-[4,5-dimethylthiazol-2-yl]-2,5 diphenyl tetrazolium bromide) assay is based on the conversion of MTT into chromogenic formazan crystals by living cells, which determines mitochondrial activity. Since for most cell populations, the total mitochondrial activity is related to the number of viable cells; this assay is broadly used to measure the *in vitro* cytotoxic effects of substances on cell lines. The mitochondrial activity of the cells is reflected by the conversion of the tetrazolium salt MTT into formazan crystals. Thus, any increase or decrease in viable cell number can be detected by measuring formazan concentration reflected in optical density (OD) using a plate reader at 540 nm [132].

Since the readout of the formazan concentration is based on absorbance, I was unable to use the nanoprobes with dye absorbing in the readout wavelength as this would result in erroneous results. For this reason, I used non-labelled dextran 10 kDa and two different-sized PEG-coated silica nanoparticles filled with fluorescein isothiocyanate (FITC) (Siliquan, Poland). The fluorescence properties allowed me to measure their concentration (by means of FCS), and in contrast to rhodamine B, FITC does not absorb light at 540 nm.

The cytotoxicity profiles of these three types of nanoprobes against the cell lines used in my study are shown in 5.7.

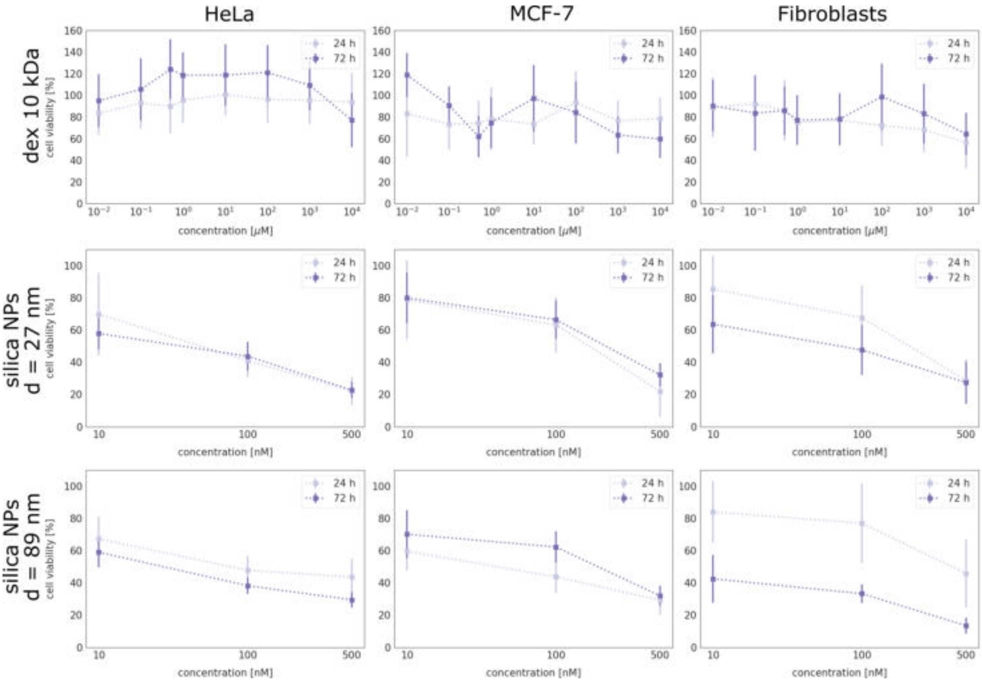

Figure 5.7: Cytotoxicity of dextran 10 kDa and two different-sized (27 and 89 nm in diameter) PEG-coated silica nanoparticles filled with FITC at different concentrations with HeLa, MCF-7 and fibroblasts cells after 24 and 72 h exposition. Results are expressed as mean ± SD. Each substance was tested in 9-fold replicates at each concentration level.

Dextran 10 kDa did not show cytotoxicity because the cell viability remains at a high level (sometimes even higher than 100%; however, with relatively large error bars) for each cell line. In contrast, the silica nanoparticles caused around a 50% decrease in cell viability, of all three cell lines, at a concentration of 100 nM and higher.

When analysing the nanoprobes cytotoxicity data, it is important to remember that the assay was performed using 2D cell cultures. The cytotoxicity is known to be lower in the case of spheroids culture [78]. Moreover, there is a lack of studies connecting the decreased cell viability with the extracellular matrix structure, as well as the degradative role of used nanoparticles on the ECM. Therefore, I assumed that the nanoparticles are relatively inert and can be used in the structural study on the ECM.

5.7 The effective viscosity of the ECM depends on the length scale

The presented fluorescent particles in the previous section were measured by FCS in HeLa, MCF-7 and fibroblast spheroids, according to the procedure described in section 5.5.

The cancerous cell lines used in this investigation were selected owing to documented variations in their invasiveness, which has been shown to correlate with the ECM stiffness [133]. HeLa cells are moderately invasive, while the MCF-7 cell line is non-invasive [134]. Fibroblasts were used for the purpose of providing the model of the non-cancerous cell line, known to synthesise the extracellular matrix.

The effective viscosity experienced by the nanoprobes (Tab. 5.1) inside each of the three kinds of spheroids is shown in Fig. 5.8. The measured mobilities data were fitted with the length-scale dependent viscosity model (Eq. 5.2) using A, ξ, R_h and a as the free parameters. The data analysis for all three spheroid types revealed that parameter a was close to unity within 7% of uncertainty, therefore I decided to fix this parameter as 1. The values of other fitting parameters are presented in Tab. 5.2.

The viscosity of the ECM, regardless of the cell line creating spheroids, is not constant but depends on the size of the probe used in the experiments, similarly as it has been reported for cytoplasm [8]. Intuitively, diffusion decreases with larger particles; however, the presented results reveal that the relationship is not linear as expected from the Stokes-Einstein relation ($D = kT/6\pi\eta r_p$). In fact, D is a stretched exponential function of the length-scale of the flow around the probe. This function describes how the motion of nanoprobes in complex liquids is altered.

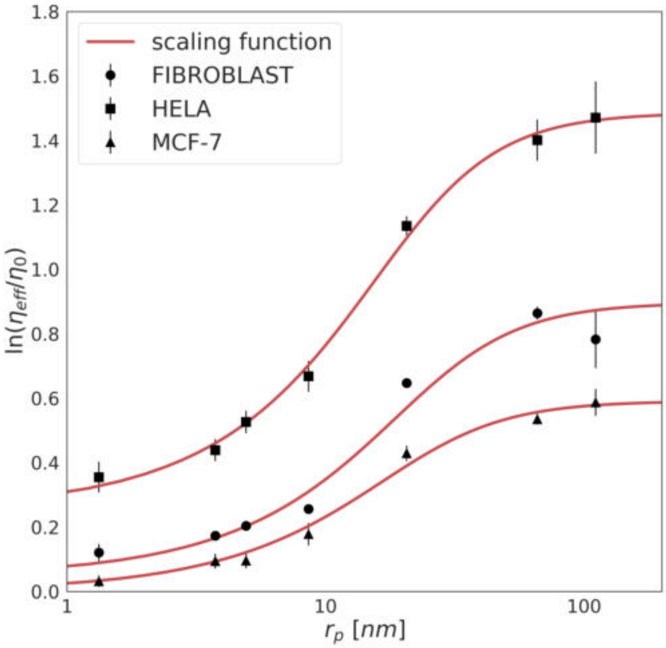

Figure 5.8: The logarithm of effective viscosity experienced by nanoprobes of radii r_p moving in the ECM of HeLa, MCF-7, and fibroblast spheroids. Error bars correspond to the standard deviations (N > 30). The fit of a length-scale dependent viscosity model (Eq. 5.2) is presented as a solid line. The fitting parameters are listed in Tab. 5.2 [10].

Firstly, the diffusion of probes of up to 10 nm in radius is almost unobstructed by the ECM. This implicates that probes whose $r_p \ll \xi$ experience effective viscosity which is similar to that of the solvent. Then, for tracers bigger than the correlation length $r_p > \xi$, we observe an exponential increase in the values of the effective viscosity experienced by the probe. In all examined spheroids, tracers bigger than $r_p \gg 90\ nm$ (i.e. $4R_h$) experience the effective viscosity corresponding to macroscopic viscosity.

Table 5.2: The determined values of parameters characterising the ECM structure within the three types of spheroids. η_0 corresponds to the viscosity of PBS, which is 0.75 $mPa{\cdot}s$. [10].

HeLa spheroids	
Nanoviscosity of the ECM, $\eta_{ECM} = A\eta_0$	$(1.29 \pm 0.04)\eta_0 = 0.97\ mPa{\cdot}s$
Correlation length, ξ	17.78 ± 1.73 nm
Hydrodynamic radius, R_h	21.93 ± 1.94 nm
Obstacle length, L	220 ± 2 nm
Macroscopic viscosity of the ECM, η_{macro}	$4.43\eta_0 \approx 3.32\ mPa{\cdot}s$
MCF-7 spheroids	
Nanoviscosity of the ECM, $\eta_{ECM} = A\eta_0$	$(1.00 \pm 0.03)\eta_0 = 0.75\ mPa{\cdot}s$
Correlation length, ξ	39.72 ± 6.98 nm
Hydrodynamic radius, R_h	23.47 ± 3.81 nm
Obstacle length, L	240 ± 18 nm
Macroscopic viscosity of the ECM, η_{macro}	$1.81\eta_0 \approx 1.36\ mPa{\cdot}s$
Fibroblasts spheroids	
Nanoviscosity of the ECM, $\eta_{ECM} = A\eta_0$	$(1.05 \pm 0.07)\eta_0 = 0.79\ mPa{\cdot}s$
Correlation length, ξ	30.94 ± 7.50 nm
Hydrodynamic radius, R_h	26.30 ± 6.30 nm
Obstacle length, L	274 ± 40 nm
Macroscopic viscosity of the ECM, η_{macro}	$2.46\eta_0 \approx 1.85\ mPa{\cdot}s$

In consequence, on the example of HeLa spheroids (Tab. 5.2), the nanoprobes (with a radius much smaller than the hydrodynamic radius introduced in our model, $r_p < R_h$) experienced nanoscopic viscosity ($\eta_{nano} = 0.97\ mPa \cdot s$), much lower than the macroscopic one ($\eta_{macro} =$

$3.32\, mPa \cdot s$). When a molecule of radius $r_p = 0.7$ nm (size of the common chemotherapeutic, doxorubicin) would experience the constant, macroscopic viscosity, its diffusion coefficient would be equal to $D = 97\, \mu m^2/s$. In fact, this molecule diffuses around 3.5 times faster (with D equals around 335 $\mu m^2/s$) since it experiences nanoscopic viscosity.

According to the length-scale dependent viscosity model, R_h corresponds to the mean value of hydrodynamic radii of obstacles creating the environment surrounding the probes. Interestingly, this parameter in all types of spheroids had approximately the same value, $R_h \approx 23$ nm, suggesting the same-sized obstacles among the examined spheroids. Type I collagen, the most abundant fibrous protein in the extracellular matrix, might be regarded as the major hindrance. Knowing that the radius of an individual collagen molecule $r_c = 0.75$ nm [120], the length of the ECM obstacles can be calculated using the relation $R_h = L/(2s - 0.19 - 8.24/s + 12s - 2)$, where $s = ln(L/r)$ and L is the filament length [135]. The estimated lengths of the obstacles have a range between 220 and 270 nm and are similar to the length of the collagen monomers (250–300 nm) previously determined using AFM [136].

The nanoviscosity of the ECM is another parameter that is nearly the same across three different types of spheroids. The probes with a radius smaller than 10 nm experience extracellular viscosity comparable to the viscosity of the solvent, irrespective of whether spheroids are made of cancerous (HeLa, MCF-7) or non-cancerous (fibroblasts) cell line. The correlation length, ξ, which affects the macroscopic viscosity value, η_{macro}, is the parameter that distinctive spheroids. η_{macro} (and the correlation length) is approximately two times higher in HeLa than in the other two tested cell lines.

I supported the quantitative analysis by the confocal imaging of ECM components, presented in Fig. 5.2 and 5.9. In addition to immunostaining, I simultaneously imaged the main fibrous proteins - collagen and elastin - which are important for the formation of the extracellular network.

The visualisation of the matrix (Fig. 5.9) was done using a fluorescent collagen-binding reagent, Col-F (Immunochemistry Technologies, USA), according to the protocol described in A.12. The major advantages of labelling and imaging of ECM fibres with Col-F are simplicity (single step procedure, without a necessity to fix the sample) and rapidity (due to the small size of Col-F, it can fast penetrate spheroids or tissues) [137].

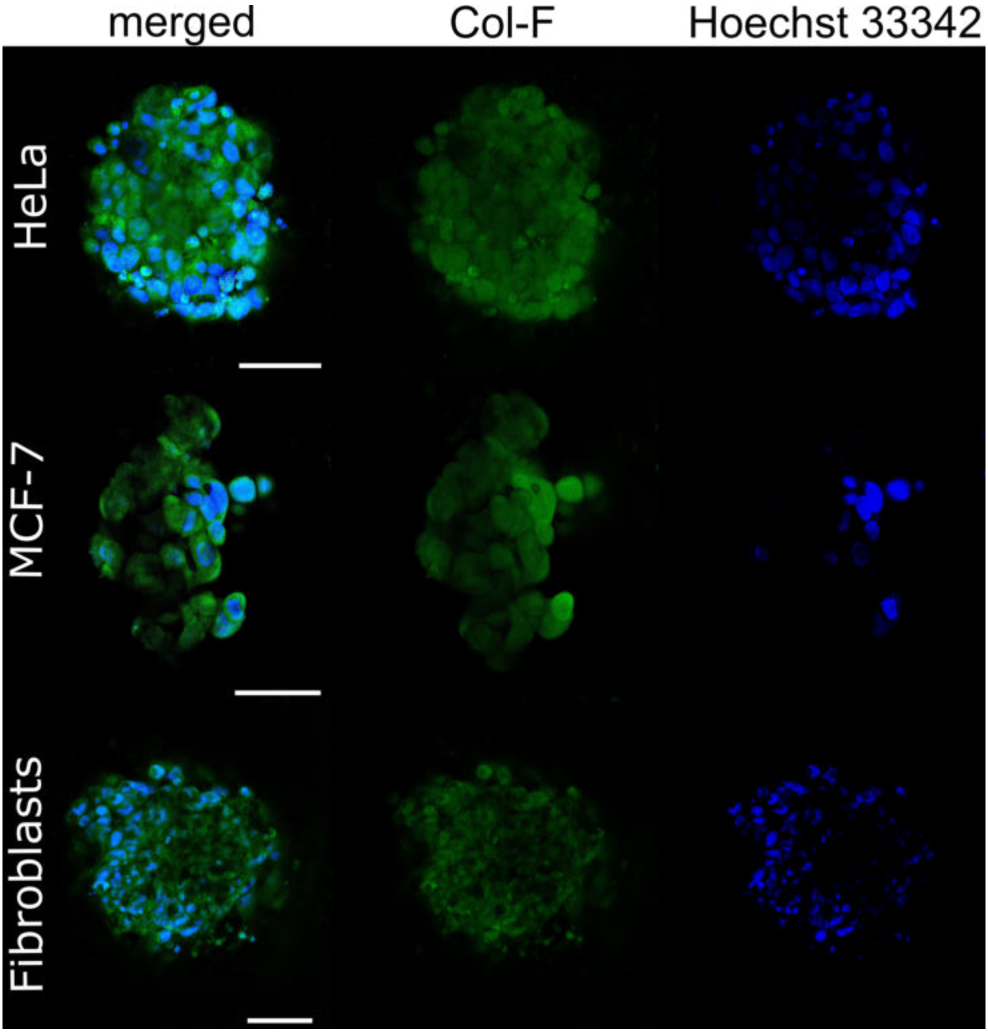

Figure 5.9: Confocal imaging of collagen and elastin (green) within HeLa, MCF-7 and fibroblast spheroids. The nuclei were counterstained with Hoechst 33342 (blue). The scale bars are 50 μm [10].

Both figures (Fig. 5.2 and 5.9) illustrate the variations in the density of the fibres among the studied cell lines, which follow the trend of changes in ξ and consequently in the macroscopic viscosity, as shown in Tab. 5.2. The observed density of fluorescent fibres in HeLa spheroids is markedly higher than in MCF-7 and fibroblasts spheroids. Moreover, I observed that MCF-7 spheroids were smaller and had a more loose structure than other types of spheroids. It is an interesting result since the study reveals that depending on cell lines, spheroids differ in morphology and structure of the extracellular matrix.

5.8 The time-related changes of the ECM structures

As I already reported (please see Fig. 4.3), spheroid formation involves three subsequent steps: initial aggregation, compaction and spheroid maturation. In order to quantify the changes occurring in the ECM structure throughout the process of spheroid formation, I measured the diffusivity of PEG-coated S34(1) nanoparticles in HeLa spheroids. I choose this probe since its size ($r_p = 20.6$ nm) is close to the correlation length of the ECM in HeLa spheroids.

I began the experiment one hour after seeding the spheroids and proceeded for the following 13 days, assessing the correlation length (ξ) at various time intervals to identify changes in the ECM mesh size. Based on Eq. 5.2, we get:

$$\xi = \frac{R_{eff}}{\left| ln\left(\frac{D_0}{D}\right) - ln(A)\right|^{1/a}} \tag{5.8}$$

where an effective radius of a probe is defined as $R_{eff}^{-2} = R_h^{-2} + r_p^{-2}$. The values for R_h and A were taken from Tab. 5.2 (HeLa spheroids), and $a = 1$.

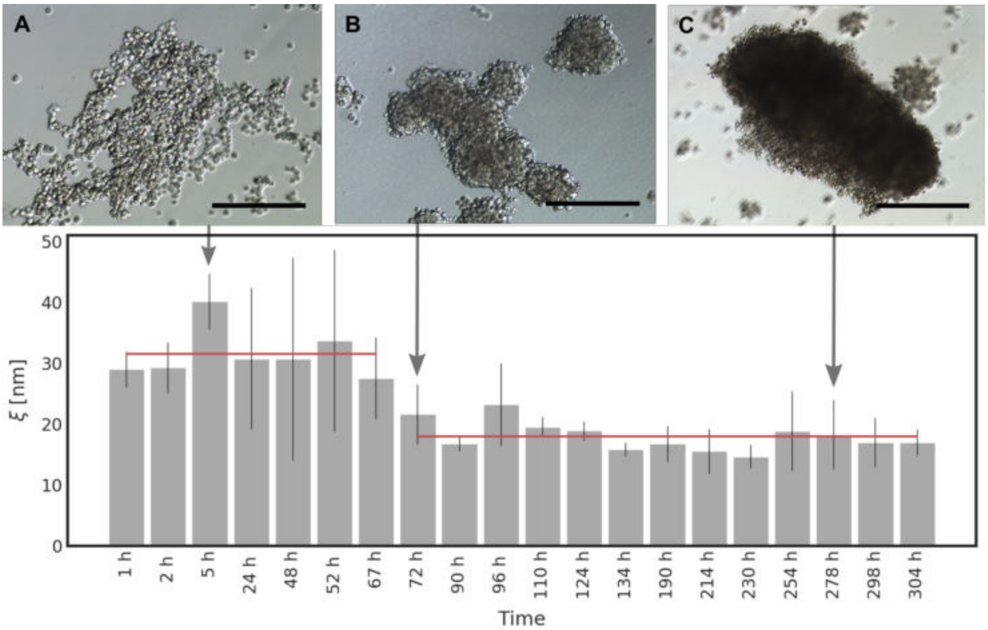

Figure 5.10: The variations in the interfibrillar spacing (characterised by ξ) of the ECM network over time during HeLa spheroid formation. Five hours after seeding, the aggregates have a loose and irregular structure, as seen in **A**. After around 3 days, aggregates became more compact, as seen in panel **B**, which corresponded to a reduction in the size of the mesh in the ECM network. The structural properties of the matrix do not alter as spheroids further mature, however the spheroid structure is more compacted, as can be noticed in panel **C**. Scale bar corresponds to 250 μm. The lower panel presents mean ξ values ± SD. Each bar was calculated based on at least 15 correlation functions that were recorded per spheroid. The measurements were performed for 3 different spheroids [10].

The changes of the correlation length, calculated based on Eq. 5.8, throughout the process of HeLa spheroid formation are shown in Fig. 5.10. According to the presented data, in the first three days of HeLa spheroid culture, the average half-distance between the points of entanglement in the ECM is $\xi = (31.59 \pm 7.86)$ nm. After one hour from seeding the spheroids, the interfibrillar spacing was unexpectedly narrow and remained at a comparable value over the following 67 hours.

The fact that ξ has quite small values in such a short period of time after cell seeding may be due to the presence of surface proteins. For instance, fibronectin is a glycoprotein present at the cell surface, which forms a fibrillar network between adjacent cells [138]. According to the formation mechanism of spheroids, dispersed cells initially are drawn closer to form loose aggregates thanks to, e.g. fibronectin that can bind tightly to the integrin on the cell membrane surface [7]. I observed that aggregates were forming immediately due to cell-cell contact. Moreover, it has been shown that procollagen is secreted with a half-life within the cell of fewer than 30 minutes [139].

After 72 h, there is around a two-fold decrease in $\xi = (17.97 \pm 6.65)$ nm, which does not change upon further maturation of spheroids. The formation of compact spheroids from loose aggregates through tight aggregates is a macroscopic process. Apparently, the change of interfibrillar spacing at the nanoscale does not decrease monotonically. Thus, it can be concluded that it takes approximately 60–70 hours for the cells in the spheroids to create the network of collagen in the ECM [10].

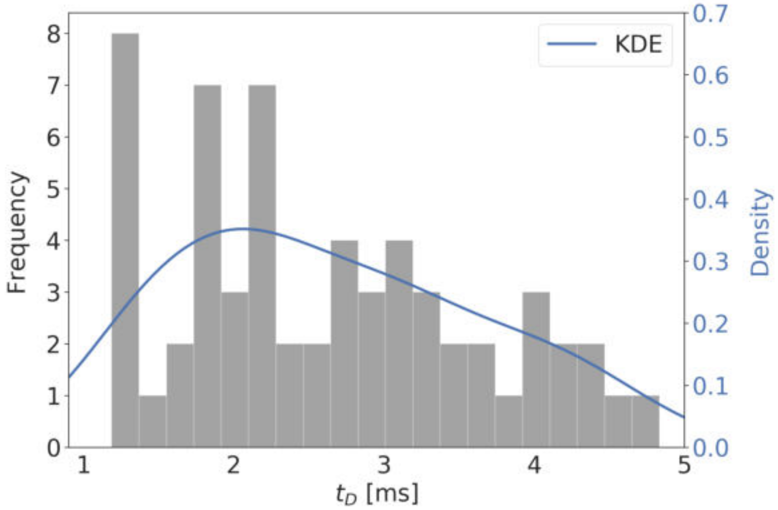

Figure 5.11: Histogram showing the distribution ($N = 60$) of a measured diffusion time for PEG-coated S34(1) silica nanoparticles within the ECM of HeLa spheroids. The solid blue line corresponds to kernel density estimation (KDE) of the histogram (right y-axis) [10].

The occurring large deviations in the results (range from 72 h to 304 h of the spheroid culture) can be related to the heterogeneity of the ECM structure. The diffusion times of the analysed probe was in the range from 1 ms up to 4 ms. The short diffusion times suggest the presence of large free extracellular spaces. On the contrary, slow-moving probes (long diffusion times) probe fibrous-rich areas. However, if there were only fibrous-rich and fibrous-free areas, the bimodal distribution would be obtained. In our case, the distribution, presented in Fig. 5.11, is wide and quite uniform, what points at the heterogeneity of the ECM structure - the presence of the different matrix pore sizes, an intrinsic disorder of the fibre network, and uneven distribution of the ECM components. The heterogeneity of the ECM structure was additionally illustrated in Fig. 5.12.

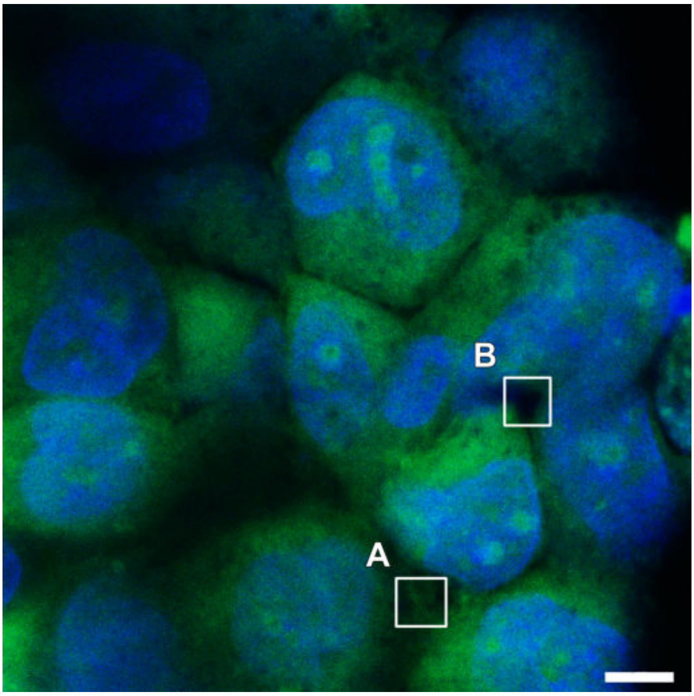

Figure 5.12: Confocal image of the ECM structure (in HeLa spheroid) after staining with Col-F (green). The nuclei were counterstained with Hoechst 33342 (blue). Panel A represents the fibrous-rich extracellular space. In contrast, panel B depicts a large free extracellular space. The scale bar is 10 μm [10].

Additionally, Fig. 5.12 indicated that the dense network of the ECM is predominantly localised around the cells. Moreover, the density of the matrix around the cell varies significantly throughout the spheroid cell population, as could be shown in Fig. 5.13.

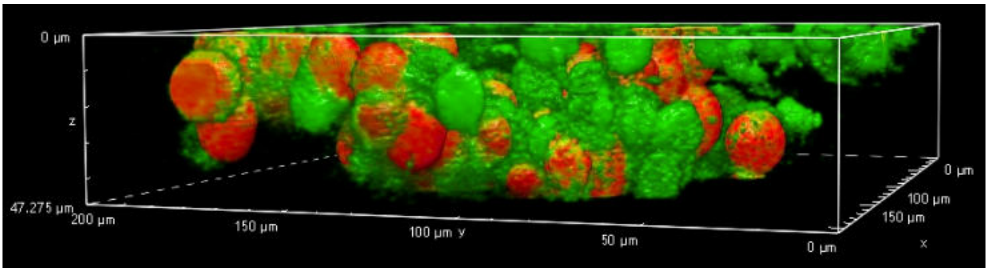

Figure 5.13: The confocal image of HeLa GFP spheroid with PEG-coated silica nanoparticles. The green fluorescence signal is from HeLa cells expressing EGFP, while the red signal corresponds to PEG-coated silica nanoparticles with a hydrodynamic radius of 22.72 nm. The dense structure of extracellular fibres can cause accumulation of the nanoprobes in their network (intense red signal around some of the cells). The imaging was performed 20 minutes after adding nanoparticles. Because of this short incubation time of spheroid with nanoparticles, they do not penetrate the cells, ensuring that the signal does not originate from the cytoplasm. $z = 0$ μm corresponds to the bottom of the glass.

5.9 Method to test factors influencing the ECM structure

As I demonstrated, the extracellular matrix acts as a transport barrier, slowing the movement of nanoparticles and so reducing their effective penetration. Therapies targeting the extracellular matrix are among the approaches that aim to overcome this obstruction [140–142]. Goodman et al. [143] assessed the effect of collagenase (enzyme that breaks the peptide bonds in collagen) treatment on nanoparticles penetration into spheroids. Collagenase treatment increased delivery efficiency for tested nanoparticles. However, since the conclusions were drawn only on the basis of the imaging analysis, nothing is known about the treatment's influence on the ECM nanostructure.

In the previous section, I demonstrated the method for measuring the interfibrillar spacing of the ECM network (Eq. 5.8). Thus, I can quantify the influence of any substance on the ECM nanostructure by performing diffusivity measurements and using the length-scale dependent model, as I reported below on the example of decorin.

Decorin, named because it "decorates" collagen fibrils, belongs to extracellular matrix proteoglycans. The known role of decorin is to regulate fibrillogenesis by inhibiting type I collagen maturation and regulating collagenase expression [144]. As a result, I anticipated that the diffusion inside the decorin-enriched spheroids would be faster than inside the control spheroids. To test our hypothesis, I cultured HeLa spheroids in decorin-enriched culture media (containing either 1% or 2% (w/v) decorin), followed by an assessment of the effective diffusion of

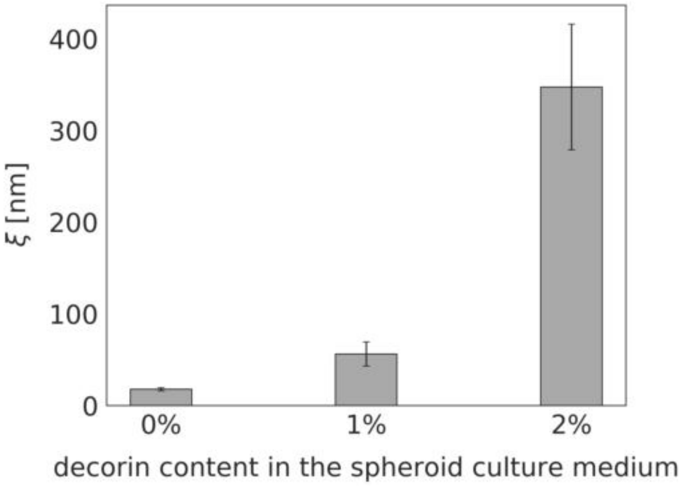

Figure 5.14: The differences in the interfibrillar spacing of the extracellular network ξ in HeLa spheroids cultured without (0%) and treated with 1% and 2% w/v of decorin. Each bar, corresponding to ξ value, was calculated based on at least 15 correlation functions that were recorded per spheroid. The measurements were performed for 3 different spheroids [10].

PEG-coated S34(1) silica nanoparticles using FCS.

In the decorin-enriched spheroids, I found an approximately 20-fold increase in the interfibrillar spacing in the ECM network, and consequently, a reduction in the effective viscosity encountered by a probe (Fig. 5.14). A probe with a radius of 100 nm would diffuse two times faster in spheroids exposed to decorin than in the non-treated HeLa spheroids.

This demonstrates that decorin indeed possesses antifibrotic properties, and its presence makes the ECM structure looser. Additionally, the acquired findings corroborate the accuracy of the measurements since we detected variations in effective diffusion in response to known changes in the ECM structure.

5.10 Further directions

Despite numerous concepts of *in vitro* tissue models, there is still a need to develop tools and methods, which simulate characteristics of solid tumours.

This chapter presented that spheroids are an excellent model in studies on the transport of probes in the extracellular matrix. Spheroids produce an extensive ECM, which provides the imitation of the native ECM, maintaining the simplicity of cell culturing.

Undoubtedly, a tumour is a much more complex system than spheroids, if only because a tumour is a mass composed of multiple cell types. To maintain the architecture and cell composition, co-culture spheroids have been developed. In co-cultures, different cell types are grown together in the same environment, offering the opportunity to create novel 3D tissue-like models [72, 73, 145].

Co-culture spheroids were used i.e. to study their response to X-irradiation [146], drugs [147], or cell-cell interactions [148]. Here, I used a co-culture composed of HeLa cell line and fibroblasts in order to assess their ECM structure. The study on the effect of spheroid cell composition on the forming ECM structure can be carried out by comparing the nanoprobe mobility within co-cultured spheroids with their mono-culture equivalents.

I generated co-culture spheroids by mixing HeLa cells with fibroblasts at a ratio of 1:1, 1:2, 1:3, and 1:5 (keeping the total cell number per wall at the same level) and seeded on NunlconSphera™ dish in a culture medium without phenol red. 24 hours post seeding, I performed imaging of HeLa spheroid and HeLa/fibroblasts co-culture spheroids, which revealed the differences in their morphological parameters (Fig. 5.15). The spheroids differ in external morphology, integrity, translucency (an indicator of spheroid compaction) and growth kinetics. HeLa spheroids were smaller, less compact and more translucent, had an irregular shape, and showed loss of integrity compared to co-culture HeLa/fibroblast spheroids in ratio of 1:2.

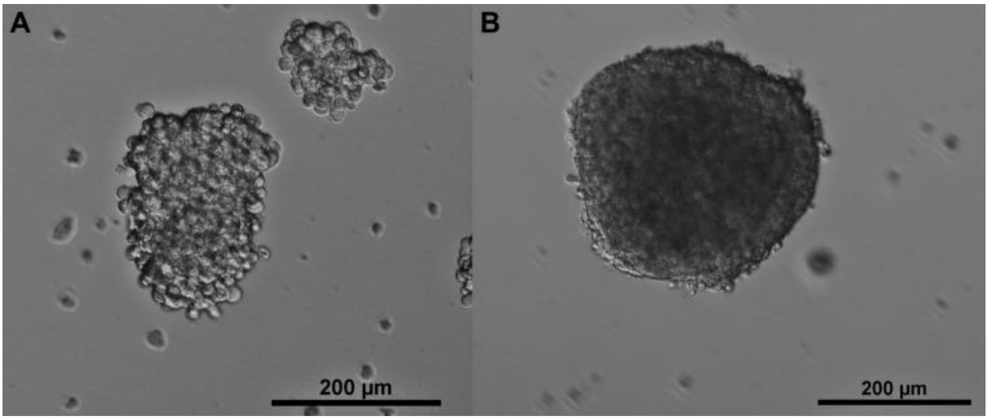

Figure 5.15: Phase contrast images of (A) HeLa spheroid and (B) co-culture HeLa/fibroblasts spheroid in 1:2 ratio. Both images were taken 24 hours post seeding.

Then, using 5-day old co-culture spheroids, I performed FCS experiments, in which I measured the diffusion of TRITC-dextran 155 kDa in the extracellular spaces of HeLa/fibroblasts spheroids. The relative values of the diffusion coefficient of the nanoprobe in a buffer and in the ECM created by various spheroids are presented in Fig. 5.16.

Interestingly, the diffusion coefficient of TRITC-dextran 155 kDa was twofold reduced in the ECM of HeLa/fibroblast spheroids produced at a 1:1 ratio, suggesting more dense ECM in co-cultures than in ECM produced by HeLa or fibroblasts alone. With the rise in the proportion of fibroblasts in co-culture spheroids, the dextran diffusion decreased even more - the nanoprobe movement in the ECM of co-culture spheroids composed of a 5:1 ratio of fibroblasts and HeLa cells is nearly four times slower than in a buffer. The impeded dextran mobility is very likely caused by the decrease in the interfibrillar spacing in co-culture spheroids.

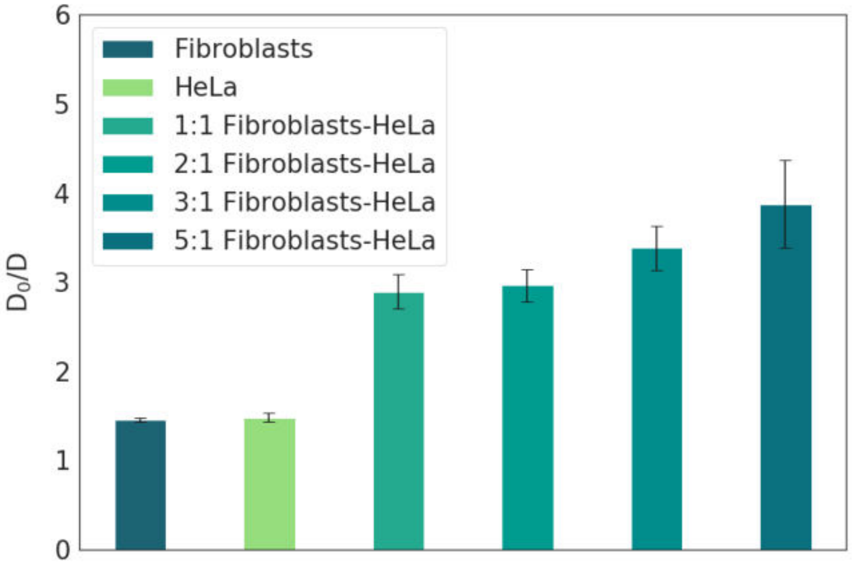

Figure 5.16: Relative values of diffusion coefficients of TRITC-dextran 155 kDa in a buffer and in the ECM created by a different type of spheroids. HeLa cells cocultured with fibroblasts (at different co-culture ratio) develop a more dense ECM than HeLa or fibroblasts alone, which effectively slows down the mobility of nanoprobe. Each bar was calculated based on at least 15 correlation functions that were recorded per spheroid. The measurements were performed for 3 different spheroids.

To my knowledge, no study has previously reported the different structures in the extracellular matrix of co-culture spheroids as compared to mono-cultures. Therefore, the mechanisms responsible for structural alterations in the extracellular network have not yet been identified. My study brings up a challenging question: why do cancer cells in the presence of stromal cells produce a more dense extracellular matrix?

5.11 Conclusions

Multicellular spheroids have been employed in many applications, but mainly they are used as *in vitro* models to mimic the complexity of the tumour [81]. For tens of years, the majority of studies have concentrated on the biochemistry, biophysics, and molecular biology of cancer cells, with just a passing mention of the extracellular environment. The presence of extracellular matrix in spheroids was demonstrated for the first time in 1984 [129], indicating that multicellular spheroids are more than just aggregates of cells; they also contain extracellular macromolecules; therefore, spheroids reflect the tissue architecture as well as its composition. Since then, there has been no detailed investigation of the ECM structure, despite its essential role in the transport of therapeutic agents to cancer cells.

To gain insight into the role of the extracellular matrix in the process of drug distribution in the tissue, I performed a study on nanoprobes mobility in the ECM of spheroids of three cell types (HeLa, MCF-7 and fibroblasts) [10]. The used nanoprobes ranged in radius from 1 to over 100 nm, encompassing the size of most therapeutic agents or their carriers used in cancer treatment. Applying vary-sizing nanoprobes led to the discovery of the length-dependent viscosity of the ECM. It means that the viscosity of the extracellular network is not constant but depends on the size of the probe used in the experiments, and the relationship between the nanoprobe size and its diffusion coefficient inside the ECM is not linear (as expected from the Stokes-Einstein relation). As a result, the probes with a radius of up to 10 nm freely diffuse in the complex network of the extracellular environment (a few times faster than it would appear from the Stokes-Einstein relation). In all examined spheroids, particles bigger than $r_p \gg 90$ nm experience the effective viscosity corresponding to macroscopic viscosity, which in the case of HeLa spheroids is almost 4.4 times higher than the viscosity of water.

Owing to the applied length-scale dependent viscosity model by determining the mobilities of the probes, for the first time, we can gain a view of the ECM nanostructure. The method appeared to be sensitive enough to identify collagen molecules as a major hindrance in the nanoprobe movement inside all types of examined spheroids. Moreover, this approach quantifies the extracellular network by characterizing the interfibrillar spacing (represented by ξ). The determined mesh size of the network differs between examined spheroids, which additionally was proved by the confocal imaging of the ECM (Fig. 5.2 and 5.9). I found that the density of the labelled fibres indeed varies among the examined cell lines and follows the trend of changes of ξ, as shown in Tab. 5.2. The interfibrillar spacing not only differs among the cell lines creating spheroids but can be modified in the process of spheroid formation. Interestingly, one hour post seeding, the determined ξ values were unexpectedly small, suggesting a very rapid process of the interaction of extracellular surface macromolecules between cells. Furthermore, after 3 days, the structure of the ECM of the compact spheroids does not change over time, which is manifested as constant interfibrillar spacing observed over the days 5.10. However, the quite constant interfibrillar spacings are not evidence of a homogenous, even distributed network in the whole extracellular spaces. In fact, the ECM is a highly heterogeneous structure, in which we can characterise fibrous-rich (predominantly localised around the cells) and fibrous-free extracellular spaces.

The methodology offering a relatively simple way to determine the nanoscopic changes in the extracellular matrix is a powerful tool in testing factors which can influence the ECM. The anti-fibrosis characteristics of any compound can be validated using diffusivity measurements and a length-scale dependent model. It has the potential to be helpful in the evaluation of new therapeutic agents which target extracellular molecules.

Moreover, I pointed out that the environment of spheroid culture has a leading role in forming the ECM structure. The co-culture spheroids made of cancer cells and stromal cells have a more dense ECM structure as compared to mono-cultures. To date, nothing is known about the molecular mechanism responsible for the structural alteration in the ECM structure in co-cultures. Further research on the ECM structure in co-cultures, undoubtedly, will lead to many valuable findings.

Presented in this work, a wealth of information gained through the application of fluorescence correlation spectroscopy to biological matter can capture the nanoscopic structure of the examined system. In Fig. 5.17 I presented an imagined 3D rendering of the inside of a spheroid modelled on the basis of the results of all FCS experiments and confocal imaging.

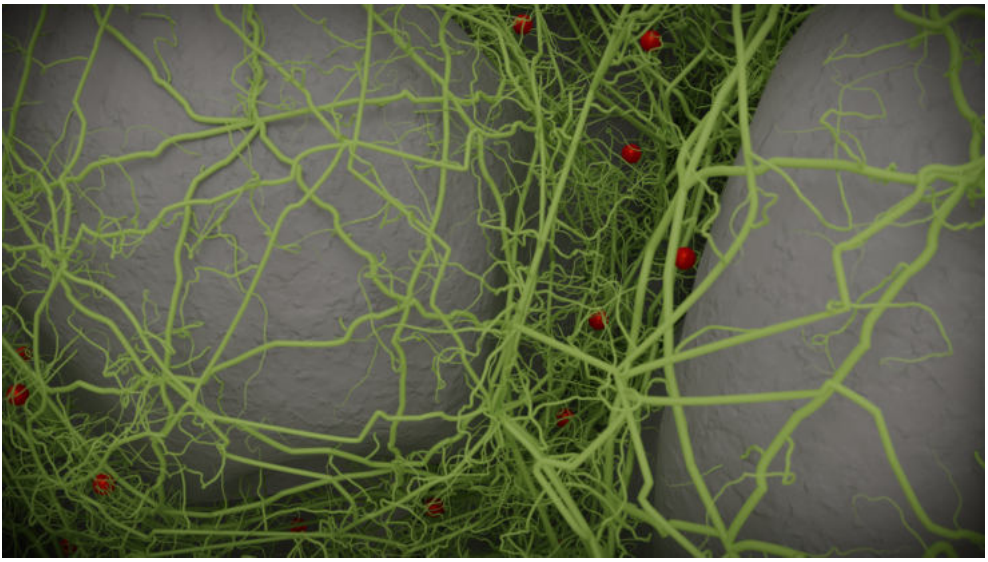

Figure 5.17: The graphical representation of the spheroid cross-section. Nanoprobes (red) diffuse between the cells (grey), which are wrapped by fibrous molecules of varying thickness (green), constituting the extracellular matrix [10].

The figure presents the cells (grey) wrapped by fibrous molecules of varying thickness (green), constituting the extracellular matrix. The structural information is gained by the mobility measurements of nanoprobes (red) diffusing in the ECM. By revealing the structure, it is possible to acquire knowledge about many aspects of biology, from understanding the cellular and extracellular processes to developing effective therapeutic agents.

6

Summary

Despite many studies carried out using fluorescence correlation spectroscopy, there are still numerous areas in the biophysical sciences to which the technique can be applied. The presented thesis has proved that with full consciousness of the method limitations, we can design FCS experiments in biosystems to determine their structure with a nanoscale resolution. First and foremost, the studied systems by an FCS may be as simple as aqueous solutions of molecules or as complex as tissue models.

By applying FCS to solutions of proteins, I revealed that trimethylamine, a metabolite that occurs naturally in humans, impaired proteins' structure irreversibly - caused their breakdown into small fragments. TMA's disruptive action depends on its concentration - the maximum tested concentration of TMA, which does not influence protein structure, even for 29 days of incubation, is 1 mM. The increase in TMA concentration, related to the rise in pH, undoubtedly negatively impacts living organisms. However, does such a high concentration of TMA occur in the tissues *in vivo*? The ongoing research on evaluating the effect of chronic administration of TMA in rats will hopefully answer the arisen question.

A breakthrough in biological research was the development of cell cultures. The ability to isolate cells and observe their behaviour under the influence of various factors is crucial in understanding the principles governing the function of living organisms. The successful application of FCS in living cells growing on the substrate resulted in many quantitative studies on dynamical processes inside a cell. FCS, above all, allowed for the determination of intracellular viscosity, a parameter influencing the rate of all biochemical reactions. The main goal of FCS application in cell biology is to perform an analysis of biomolecules (i.e. their mobility or interaction with intracellular targets) in the natural environment. However, can we assume the adherent cells as a truly native environment knowing that they do not mimic the natural, spatial organisation of tissues *in vivo*? Cells in the body are linked to form three-dimensional structures (i.e. tissues, organs), and the space between cells is filled with the extracellular matrix. The different morphology of the cells affects their function, and for this reason, we should study the cell function in systems providing a tissue-like architecture. The relative ease of obtaining three-dimensional cell cultures in the form of spheroids have made them common models with morphological features corresponding to tissues *in vivo*.

Despite many studies using 3D cell cultures, the measurements of FCS in cells within spheroids have not been reported yet. As a part of my work, I established a procedure for spheroids preparation suitable for the FCS application. Although spheroids were only probed to a depth of 30 μm, I gathered a wealth of information. Firstly, I revealed that cytoplasm nanoviscosity is comparable within the errors in both types of culture (monolayer of cells and spheroids). However, the cytoplasm organisation of large intracellular obstacles - microtubules and endoplasmic reticulum differ in 2D and 3D cultured cells (demonstrated by confocal imaging). Additionally, on the example of PARP1 protein, targeted in anticancer therapy, I proved the difference in molecular composition between 2D and 3D cells. The observed change is related to PARP1 downregulation in adherent cells as compared to cells in spheroids. Although I can not explain the mechanism behind the variation in protein expression levels, the determined upregulation of PARP1 in spheroids probably reflects its actual expression level in tumours *in vivo*.

By application of FCS inside spheroids, I also examined the nanostructure of the extracellular matrix - a main physical barrier that inhibits the penetration of anticancer drugs into the tumours and, consequently, their effectiveness. The study of vary-sizing nanoprobes mobility in the ECM has led, above all, to the discovery of the length-dependent viscosity of the extracellular network. As a result, the probes with a radius of up to 10 nm freely diffuse in the ECM - a few times faster than it would appear from the Stokes-Einstein relation, regardless of the cell line creating the spheroids.

The correctness of my methodology can be done by comparing obtained diffusion coefficients for a specific probe. Interestingly, Reitan et al. [131] measured the mobility of TRITC-dextran 155 kDa in the ECM of OHS (human osteosarcoma) spheroids. The authors reported similar values to those determined in my study. In their publication, the ratio of D_0/D for TRITC-dextran 155 kDa is about 1.5, while I got this value equals to 1.95, 1.20 and 1.29 for HeLa, MCF-7 and fibroblasts spheroids, respectively (as diffusion coefficient of dextran 155 kDa was $D_0 = 37.23\ \mu m^2/s$ in water and $D = 19.09\ \mu m^2/s$, $D = 31.15\ \mu m^2/s$ and $D = 28.82\ \mu m^2/s$ for HeLa, MCF-7 and fibroblasts, respectively).

The parameter that varies depending on the cell line used to generate spheroids is correlation length, ξ, influencing the macroscopic viscosity, η_{macro}. In HeLa spheroids, the η_{macro} of the ECM is almost two times higher than in the other two tested cell lines.

Surprisingly, the similar conclusion I made was based on the analysis of the confocal imaging of labelled elastic and collagenous fibres. The density of the extracellular network differs among the examined spheroids and follows the trend of changes of ξ.

Strikingly, the average half-distance between the points of entanglement in the ECM (ξ) after 72 h postseeding did not change upon further maturation of spheroids, suggesting that the formation of compact spheroids is a macroscopic process, not nanoscopic.

Probing spheroids by FCS supported with confocal imaging revealed that the structure of the ECM is heterogeneous - the dense network is predominantly localised around the cells. Still, large free extracellular spaces can occur as well.

To prove the applicability of my approach, I also performed experiments with decorin-treated HeLa spheroids. Decorin was chosen as a well-described agent affecting the ECM structure. The obtained results additionally confirmed that our method is fragile to changes in ECM structure.

The change in ECM structure can arise as well as from the environment of spheroids culture. Using my approach, I noted that the co-culture of spheroids made of cancer cells and stromal cells have a more dense extracellular network than mono-cultures. This observation points to the potential directions for further studies based on the presented methodology.

Appendices

A

Experimental procedures

Contents

A.1 FCS setup

The FCS set-up included the Nikon EZ-145 C1 microscope integrated with a time-correlated single-photon counting (TCSPC) data acquisition system (PicoHarp 300, PicoQuant). All measurements were carried out using a Nikon PlanApo 60x water immersion objective (NA = 1.2). Excitation was done using a laser diode emitting picosecond pulses with a duration of less than 100 ps. Depending on the excitation and emission spectrum of fluorescent probes used in the experiments, I applied a laser with a wavelength of 485 ± 3 nm or 561 ± 3 nm. The diode is controlled by the PDL 828 "Sepia II" (PicoQuant) driver, which enables the synchronization of the laser with an external electronic signal and gives the possibility of setting the repetition rate pulses in a given range. The signal was recorded by two detectors based on Single Photon Avalanche Diode (SPAD) (Micro Photon Devices and PerkinElmer Optoelectronics). The fluorescence was detected through a 488 long-pass filter or 593/46 bandpass filter (Chroma), positioned in the optical path in front of the detector.

Data acquisition was performed using Symphotime 64 software (PicoQuant). For temperature control, we used the Okolab Cage Incubation System, which stabilises the temperature with an accuracy of 0.5 ℃.

A.2 Calibration of confocal volume for FCS experiments

For the quantitative analysis of FCS measurements, perfect control over the detection volume is fundamental. The shape and dimensions of the confocal volume depend, among others, on the excitation wavelength, the glass thickness of the cover glass, the refractive index of the sample, and the adjustment of the lens correction collar [31]. Due to the above, the calibration procedure and measurements were carried out using the same laser line (with the same laser power) and the same cover glasses or dishes. In order to keep the refractive index unvaried, different calibration solutions were used, depending on the probing system (Tab. A.1) [86].

Table A.1: The choice of calibration solution is based on the examined system.

calibration solution	**the examined system**
water solution of fluorophore	water
PBS solution of fluorophore [149]	PBS buffer
fluorophore in 2.5% glucose solution [86]	the interior of cells the extracellular matrix

All experiments started with setting and stabilizing the temperature, depending on the type of experiment, at 25 ℃ or 36 ℃. Then, I measured the laser power and set it to a required value. The laser power remained unchanged during further measurements. Finally, I prepared the calibration solution - a nanomolar solution of proper fluorophore depending on the performed experiments - a solution of rhodamine 110 or rhodamine B in water, PBS or 2.5 % glucose solution (Tab. A.1).

I acquired at least twenty correlation curves during the calibration process with a duration time of 20 seconds. Collected data I analysed by using self-written Python scripts. Exemplary results of calibration measurements with fitted autocorrelation function are shown in Fig. A.1. To fit calibration data, I applied the model described in Eq. 2.1, assuming $\alpha = 1$ (the stochastic movement of dye in aqueous solution is the process of normal diffusion). Based on the fit of the function, the following parameters were determined: fraction of molecules in the triplet state, T, the lifetime of triplet, τ_T, the average number of molecules in the confocal volume, N, the translational diffusion time, τ_d, and above all, the confocal volume shape parameter, κ. Next, I averaged the obtained values from 20 measurements and calculated the semi-minor axis of the confocal volume using the transformed equation 2.3 to the form:

$$\omega_0 = \sqrt{4\tau_d D} \tag{A.1}$$

where the diffusion coefficient value, D, of the reference fluorophore is precisely characterized. I summarized the diffusion coefficient values of used fluorophores, considering their different values depending on the measurement temperature and solvent viscosity in Tab. A.2.

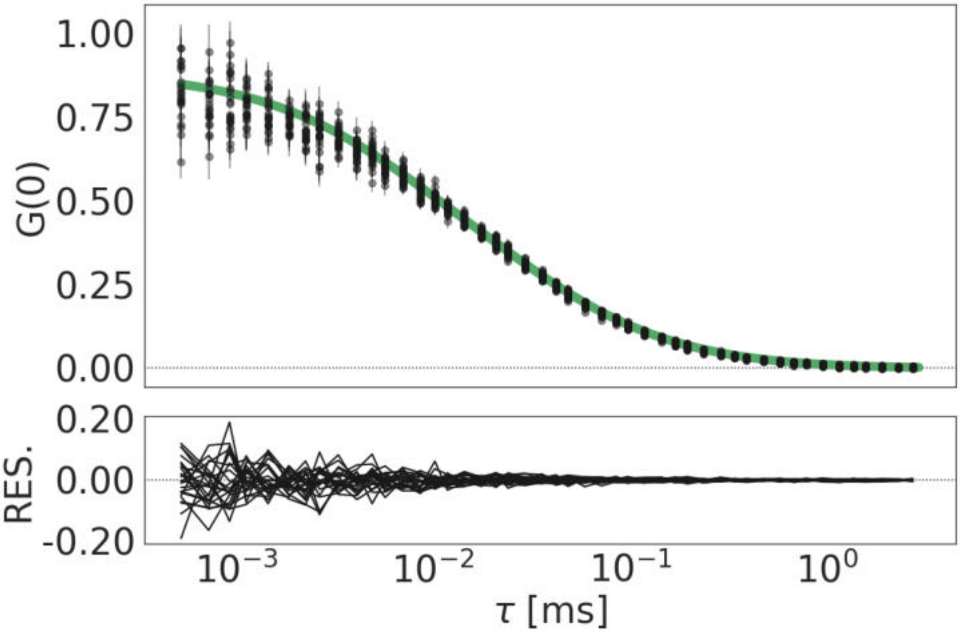

Figure A.1: Example of FCS data (black dots) obtained for rhodamine 110 in 2.5% glucose solution, at 36 °C. I fit the acquired data using a one-component model Eq. 2.1 (green line). The bottom panel shows the accuracy of the fit.

At the end of the calibration procedure, based on the ω_0 value, I calculated the effective volume, V_{eff}:

$$V_{eff} = \pi^{3/2}\kappa\omega_0^3 \tag{A.2}$$

Table A.2: Diffusion coefficient values, D, of reference dyes used for calibration purposes depending on the temperature, T, set in measurements and type of solvent.

excitation wavelength	**fluorophore**	**T**	**solution**	**D [$\mu m^2/s$]**
488 nm	rhodamine 110	25 ℃	water	470
			PBS	463
		36 ℃	water	613
			PBS	578
			2.5 % glucose solution	558
561 nm	rhodamine B	25 ℃	water	427
			PBS	420
		36 ℃	water	557
			PBS	525
			2.5 % glucose solution	507

Only after carrying out the above-described calibration process, I started the proper FCS experiments.

A.3 Measurement uncertainty analysis

The average value was taken as the result of the direct measurement:

$$\overline{x} = \frac{1}{n}\sum_{i=1}^{n} x_i \tag{A.3}$$

I calculated the uncertainty due to repeatability or a random error as the standard deviation of the mean value:

$$u(x) = \sqrt{s_{\overline{x}}^2} = \sqrt{\frac{1}{n(n-1)}\sum_{i=1}^{n}(x_i - \overline{x})^2} \tag{A.4}$$

For several independent measuring series of the same physical quantity, I calculated a weighted average to obtain the best approximation of the measured quantity:

$$\overline{x}_w = \frac{\sum_{i=1}^{n} w_i x_i}{\sum_{i=1}^{n} w_i} \tag{A.5}$$

wherein w_i are statistical weights:

$$w_i = \frac{1}{s_{\overline{x}}^2} \tag{A.6}$$

The weighted average uncertainty is equal to:

$$u(x) = \sqrt{\sum_{i=1}^{n} w_i} \tag{A.7}$$

For values derived from the measurement of other quantities (indirect measurements), it is needed to develop an equation that defines the mathematical relationship between the derived quantity of interest and the measured ones. For a case involving n measured quantities $x_1, x_2, ..., x_n$, this equation can be written $q = f(x_1, x_2, ..., x_n)$. I determined for every directly measured quantity its mean value and standard uncertainties. Then total uncertainty was calculated using the following formula:

$$u(x) = \sqrt{\left(\frac{\partial f}{\partial x_1} u(x_1)\right)^2 + \left(\frac{\partial f}{\partial x_2} u(x_2)\right)^2 + ... + \left(\frac{\partial f}{\partial x_n} u(x_n)\right)^2} \tag{A.8}$$

Hence, for instance, while determining the minor-axis of the confocal focus ω_0, its total uncertainty can be expressed as:

$$u(\omega_0) = \sqrt{\left(\frac{\partial \omega_0}{\partial \tau_D} u(\tau_D)\right)^2} \tag{A.9}$$

On the other hand, when I calculated the diffusion coefficient of a fluorescent molecule, I determined its total uncertainty using the formula:

$$u(D) = \sqrt{\left(\frac{\partial D}{\partial \tau_D} u(\tau_D)\right)^2 + \left(\frac{\partial D}{\partial \omega_0} u(\omega_0)\right)^2} \tag{A.10}$$

A.4 Protein labelling protocol

I labelled proteins with amine-reactive ATTO 488 dye in the form of NHS-estres (ATTO-TEC GmbH). NHS-estres readily react with amino groups of lysine (K) or the amine terminus, forming a chemically stable amide bond between the dye and protein [150]. The optimum pH range for NHS-ester coupling is 8.0-9.0. At this pH, amino groups of lysines are unprotonated to a high degree and highly reactive towards the dye-NHS-ester.

Conjugate preparation

1. Prepare labelling buffer - phosphate buffered saline (PBS) solution with a phosphate buffer concentration of 0.01 M and sodium chloride concentration of 0.154 M. Adjust buffer pH to 8.3 with 0.2 M sodium bicarbonate solution.
2. Under sterile conditions, dilute proteins in labelling buffer.
3. Add to the protein solution a threefold molar excess of reactive ATTO 488 dye.
4. Incubate the reaction mixture for 1 h at room temperature, protected from light.

Due to unavoidable side reaction, part of the applied ATTO 488 NHS-ester will hydrolyse during the labelling reaction and must be removed. I used Zeba™Spin desalting columns (ThermoFisher) to purify protein away from small dye molecules. The desalting procedure was carried out following the protocol suggested by the manufacturer [151].

Procedure for desalting

1. Twist off the column bottom closure and loosen cap. Place the column in a collection tube.

2. Centrifuge columns at 1000 × g for 2 minutes to remove storage solution.
3. Add PBS buffer, pH 7.3.
4. Centrifuge at 1000 × g for 2 minutes to remove buffer.
5. Repeat Steps 3 and 4 two or three additional times, discarding the buffer from the collection tube.
6. Place column in a new collection tube, remove cap and slowly apply reaction mixture of protein and dye.
7. Centrifuge at 1000 × g for 2 minutes and collect the sample. Discard column after use.

A.5 Sodium dodecyl sulfate polyacrylamide gel electrophoresis (SDS-PAGE)

Sample preparation

Firstly, I prepared reduced protein sample according to the instruction:

1. Mix 1 μl of protein with 2.5 μl of NuPAGE LDS (Invitrogen, USA) sample buffer, and 5.5 μl of deionized water.
2. Heat the samples for denaturing electrophoresis at 70 ℃for 10 minutes.
3. Add 1 μl of NuPAGE reducing agent (Invitrogen, USA)

Electrophoresis

I used mini-PROTEAN Electrophoresis System (BIO-RAD, USA) with a NuPAGE 12 % Bis-Tris gel (Invitrogen, USA).

1. Mount ready gels in the cassettes and assemble them in the electrophoresis module.

2. Fill the upper chamber with running buffer - NuPAGE MES SDS (Invitrogen, USA) with NuPAGE antioxidant (Invitrogen, USA). The buffer level must exceed the level of the wells.
3. Load 10 μl of samples onto the gel.
4. Load protein molecular weight marker. I used PageRuler^{TM} (Thermo Scientific, USA) unstained protein ladder consisting of 14 highly purified proteins (10 to 200 kDa).
5. Apply power of 180 V and run gels for around 40 minutes.

Coomassie staining

Staining of the gel was according to the Coomassie Brilliant Blue G-250 method using PageBlue^{TM} (Thermo Scientific, USA) solution.

1. Remove the gels after electrophoresis and place them into the container containing PageBlue^{TM} solution.
2. Stain gels overnight.
3. Destain gels by washing them in ultrapure water for 1 hour.

Finally, I imaged the gels using the Gel Doc XR+ System (BIO-RAD, USA) which enables their quick visualization and analysis.

A.6 Culture of cells

Cells are usually cultured as a single layer of cells on a flat surface of culture flasks in the presence of the culture medium as a source of nutrients. The culture medium consists of vitamins, cofactors, metabolic substrates, amino acids, inorganic ions, and trace elements to promote cellular functions and cell proliferation. Buffering is also needed to keep the cells in their normal pH range and reduce the effects of acidic waste products generated by the cell, especially CO_2 and lactic acid. Most media often have non-essential ingredients that aid the cell culture scientist's work, such as Phenol Red, which provides an immediate visual indication of the approximate pH of the medium. All of the above components are generally supplied by the basal medium like minimal essential medium (MEM) or Dulbecco's modified Eagle's medium (DMEM). The cultivation medium is supplemented, among others, by fetal bovine serum (FBS) (source of growth factors, proteins, and hormones), antibiotic Penicillin Streptomycin (Pen-Strep) solution to maintain sterile conditions during cell culture and essential amino acid L-glutamine or non-essential amino acids (NEAA) [71].

The actual basal medium, the type of serum and its concentration depend predominantly on the cells to be cultured. Moreover, cells may need additional nutrient supplementation, for example, insulin, for optimal cell proliferation.
In Tab. A.3 I listed cell lines used in my research and the composition of their complete growth medium.

All cell lines were cultured according to the following procedure:

1. Remove culture medium and gently rinse the cell with 2 ml of phosphate-buffered saline solution (PBS).
2. Remove PBS and add 1 ml of the trypsin-EDTA solution to the flask so that the solution covers the whole surface.
3. Incubate the flask at 37 ℃.
4. Monitor the progress of the cell detachment under an inverted microscope.
5. When cells start to be detached from the substrate, add 4 ml of fresh culture medium. Aspirate cells by gently pipetting.

6. Add appropriate aliquots of the cell suspension to new culture vessels. Add 10 ml of complete medium and place the cells to the incubator.

Table A.3: The cell lines used in my research and their complete growth medium.

cell line	**culture medium**
HeLa	The base medium is DMEM with a low concentration of glucose (1 g/L). The complete growth medium was made by adding the following components to the basal medium:10% FBS, 1% Pen-Strep, and 1% L-glutamine.
HeLa GFP	The base medium is DMEM with a high concentration of glucose (4.5 g/L). The complete growth medium was made by adding the following components to the basal medium: 10% FBS, 1% Pen-Strep, 1% L-glutamine, and 1% NEAA.
Fibroblasts	The base medium is a 1:1 mixture of DMEM with a high concentration of glucose (4.5 g/L) and MEM. The complete growth medium was made by adding the following components to the basal medium: 15% FBS, 1% Pen-Strep, and 1% L-glutamine.
MCF-7	The base medium is DMEM with a low concentration of glucose (1 g/L). The complete growth medium was made by adding the following components to the basal medium: 10% FBS, 1% Pen-Strep, 1% L-glutamine, and 10 μg/ml insulin.

A.7 Introduction of nanoprobes into cells

The nanoprobes were internalized in the cytoplasm of HeLa cells with a cell-loading technique based on the osmotic lysis of pinocytic vesicles using Influx™ reagent (ThermoFisher, USA). Influx contains an optimized mixture of sucrose and polyethylene glycol (PEG), which constitutes a hypertonic medium. The hypotonic lysis medium is made by mixing culture medium, without serum, and sterile deionized water in a 6:4 ratio. For loading cells in suspension I used the following procedure [152]:

1. Make a hypertonic solution containing at least 20 μl of Influx reagent and 2 μl of the substance to be loaded into the cells. Prewarm the solution at 37 ℃.
2. Prepare cell suspension in 5 ml of culture medium. Centrifuge the sample for 5 minutes at 3500 rpm. Remove the medium.
3. Add 1 ml of fresh medium to the cell pellet and transfer to a 1.5 ml eppendorf tube.
4. Centrifuge the sample for 1 minute at 2500 rpm.
5. Carefully discard the supernatant solution. Next, add 22 μl of the hypertonic solution to the cell pellet.
6. Incubate cells at 37 ℃for 10 minutes.
7. Add 1 ml of the hypotonic solution to the cells and transfer the suspended cells to a tube containing 2 ml of hypotonic solution.
8. Distribute the solution into three 1.5 ml eppendorf tubes, then incubate the cells for 1.5 minutes at 37 ℃. Prolonged exposure of cells to a hypotonic medium may cause cell death.
9. Centrifuge the sample for 1 minute at 2500 rpm. Remove the supernatant.
10. Add the culture medium to the cells and transfer them to the NunclonSphera dish.

A.8 Microtubules staining

I performed microtubule staining with Tubulin Tracker™ Deep Red (ThermoFisheer, USA) according to the following protocol:

1. Add Tubulin Tracker to medium containing cells to a final concentration of 1 μM.
2. Incubate cells for 30 minutes at 37 ℃ and 5% CO_2. When staining 3D cell cultures, incubate spheroids for 1 hour at 37 ℃ and 5% CO_2.
3. Rinse the cells 3 times with PBS or Live Cell Imaging Solution.
4. Image and analyse the cells.

A.9 Endoplasmic reticulum immunostaining

Immunostaining is a method that uses antibodies to identify and visualise various components of cells. Immunohistochemistry is based on the extremely sensitive interaction of a specific antibody with its antigen. There are many variations of the basic protocol. However, the constant features of immunofluorescence procedures are based on the following principal stages: (i) specific antibodies bind to the protein of interest, (ii) fluorescent dyes are coupled to these immune complexes in order to visualise the protein of interest using microscopy [153]. However, the whole procedure consists of many steps, which I described below.

1. Cell fixation

One of the most critical steps in immunostaining is fixation. The goal of fixation is to preserve cells in a life-like manner, which can be damaged during the immunostaining process. The fixation can be accomplished by either chemical or physical method. In my studies, I used a cross-linking agent - formaldehyde.

1. Seed the cells or spheroids on a glass bottom dish and incubate overnight at 37 ℃ and 5% CO_2.

2. Remove the culture media from the well and wash cells twice with PBS. In the case of spheroids, agitation or shaking should be avoided not to shear them from the bottom of the dish.
3. Add Image-iT™ Fixative Solution (ThermoFisher, USA) containing 4% of formaldehyde to cells. 2D cell culture incubate 20 minutes at room temperature, spheroids incubate overnight at 4 ℃.
4. Remove the fixative solution from the well and wash cells three times with PBS.

2. Permeabilization of cell membranes

Permeabilization provides access to intracellular antigens. The organic solvents (like non-ionic detergents), during the permeabilization step, dissolve lipids from cell membranes, making them permeable to antibodies.

1. Add Triton™ X-100 (Sigma-Aldrich, USA) to PBS with cells at a final concentration of 0.3%. Incubate 2D cell culture for 5 minutes, spheroids for 15 minutes, at room temperature.
2. Remove the solution from the well and wash cells three times with PBS.

3. Blocking step

Before using specific antibodies to detect antigens, all potential nonspecific binding sites in the cells must be blocked to prevent nonspecific antibody binding. In my work, I used goat serum (animal serum from the same species as that providing the secondary antibody):

1. Add goat serum (ThermoFisher, USA) to PBS with cells at a final concentration of 20%. Incubate 2D cell culture for 1 hour, spheroids for 4 hours, at room temperature.
2. Aspirate the blocking solution from the well and wash cells three times with PBS.

4. Antibody incubation

1. Add the primary antibody, anti-protein disulfide isomerase (PDI), mouse IgG2b (SelectFX Alexa Fluor 488 Endoplasmic Reticulum Labeling Kit, ThermoFisher, USA) to a final concentration of 0.5 μg/ml. Incubate 2D cell culture for 2 hours at room temperature. Spheroids incubate overnight at 4 ℃.
2. Wash cells three times with PBS.
3. Add Alexa Fluor 488–labelled secondary antibody to a final concentration of 2 μg/ml. Incubate 2D cell culture at room temperature for 30 minutes, spheroids for 4 hours, protected from light.
4. Wash the cells with PBS. Repeat the wash 3–4 times.
5. Counterstain the cells with Hoechst 33342 (Invitrogen, USA). Add Hoechst to cell at a final concentration of 2.5 μg/ml. Incubate 2D cell culture for 20 minutes, spheroids for up to 2 hours.
6. Visualise cells using a confocal microscope and filter sets appropriate for the label used.

A.10 Immunostaining of the ECM components

The immunostaining of the ECM components was carried out in a manner similar to that described in A.9. The protocol included the following steps.

1. Cell fixation

1. Transfer spheroids to a glass bottom dish and incubate overnight at 37 ℃ and 5% CO_2.
2. Remove the culture media from the well and wash cells twice with PBS. Agitation or shaking should be avoided not to shear spheroids from the bottom of the dish.

3. Add Image-iT™ Fixative Solution (ThermoFisher, USA) containing 4% of formaldehyde to cells. Incubate overnight at 4 °C.
4. Remove the fixative solution from the well and wash the spheroids three times with PBS.

2. Permeabilization of cell membranes

1. Add Triton™ X-100 (Sigma-Aldrich, USA) to PBS with cells at a final concentration of 0.3%. Incubate for 15 minutes, at room temperature.
2. Remove the solution from the well and wash cells three times with PBS.

3. Blocking step

1. Add goat serum (ThermoFisher, USA) to PBS with cells at a final concentration of 20%. Incubate spheroids for 4 hours, at room temperature.
2. Aspirate the blocking solution from the well and wash cells three times with PBS.

4. Antibody incubation

1. Add the primary antibodies (one type of antibody per well):
    - Fibronectin Antibody (ThermoFisher, USA) at a dilution of 1:100.
    - Collagen I Antibody (ThermoFisher, USA) at a dilution of 1:2000.
    - Tenascin C Antibody (ThermoFisher, USA) at a dilution of 1:4000.
    - Elastin Antibody (Abcam, UK) at a dilution of 1:100.

2. Incubate overnight at 4 °C.
3. Wash cells three times with PBS.
4. Add Alexa Fluor 568–labelled secondary antibody to a final concentration of 2 μg/ml. Incubate for 4 hours, protected from light.
5. Wash the cells with PBS. Repeat the wash 3–4 times.
6. Counterstain the cells with Hoechst 33342 (Invitrogen, USA). Add Hoechst to cell at a final concentration of 2.5 μg/ml. Incubate for up to 2 hours.
7. Visualise cells using a confocal microscope and filter sets appropriate for the label used.

A.11 MTT cell proliferation assay

To run an assay, select an optimal cell number and follow the MTT cell proliferation assay using your experimental system. The assay will include:

- Blank wells contain medium only
- Untreated control cells (negative control) – healthy cells with 100% viability
- Dead control cells – treated with 1% Triton X (positive control) – no cells with 0% viability
- Test cells treated with the substance to be assayed

MTT solution

1. Dissolve MTT (5 mg) in (1 ml) PBS to 5 mg/ml (Vybrant MTT Cell Proliferation Assay Kit, ThermoFisher).
2. Mix by vortexing or sonication until dissolved.
3. Filter-sterilize the MTT solution through a 0.2 µm filter into a sterile, light protected container.

4. Once prepared, the MTT solution can be stored for four weeks at 4 °C protected from light.

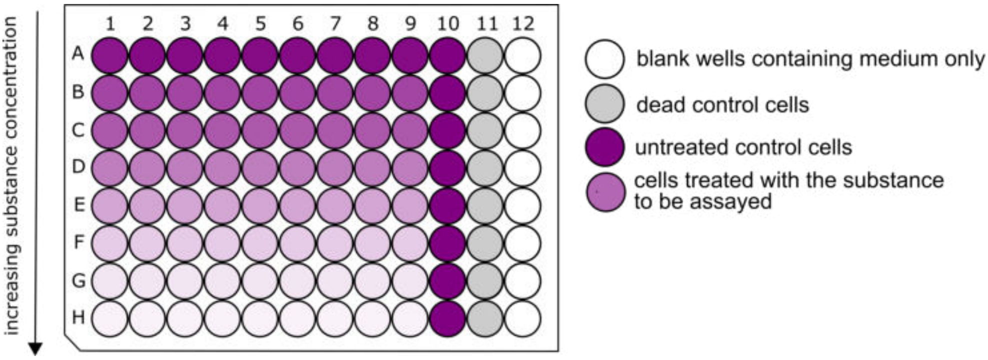

Figure A.2: Arrangement of samples in a 96 well plate for MTT assay.

MTT assay protocol

1. Trypsynize a monolayer culture and collect the cells in growth medium.
2. Centrifuge the suspension (5 min at 200 g) to pellet the cells. Resuspend the cells in growth medium and count them.
3. Seed cells at a concentration of $5{\times}10^4$ ($5{\times}10^3$ for 72 h incubation) cells per well in 100 µl culture medium (medium free of phenol red) in microplates.
4. Incubate for 24 h (cells should be in exponential growth).
5. Prepare a serial dilution of the substance to be assayed in growth medium.
6. Remove the medium and replace it with a medium containing various amounts of a compound of interest into microplates.
7. Incubate for the desired period of exposure (24 h, 48 h or 72 h).

8. After incubation at the defined time-period, remove the medium and wash the walls three times with PBS.
9. Add 100 µl of fresh culture medium.
10. Add 10 µl of the MTT stock solution to each well. Include a negative control of 10 µl of the MTT stock solution added to 100 µl of medium alone.
11. Incubate at 37 ℃ for 4 hours. At high cell densities (>100,000 cells per well), the incubation time can be shortened to 2 hours.
12. When purple precipitate is clearly visible under the microscope, remove all the medium from the wells.
13. Add 75 µl of DMSO to each well and mix thoroughly with the pipette to dissolve formazan crystals.
14. Incubate at 37 ℃ for 10 minutes.
15. Transfer supernatant from treated cells into a new multiwell plate.
16. Remove the plate cover and measure the absorbance in each well, including the blanks, at 540 nm in a plate reader. (Absorbance can be read with any filter in the range of 500 – 600 nm. The reference wavelength – corresponding to the impurities - should be 630 nm. The blanks should give values close to zero ± 0.1).

Data interpretation

Each substance is tested in 9-fold replicates at each concentration level; the negative, positive and blank control in 8-fold replicates.

The blank is subtracted from each sample before further calculation. The mean of n replicates is calculated using the formula:

$$\overline{x} = \frac{1}{n}\sum_{i=0}^{n} x_i \tag{A.11}$$

Cell viability is calculated by considering the signal from nontreated cells as the 100% viability and is determined using the following equation:

$$cell\ viability\ (\%) = \frac{A_{sample} - A_{blank}}{A_{negative} - A_{blank}} \tag{A.12}$$

where A_{sample}, $A_{negative}$, and $A_{positive}$ denotes the absorbance of sample, negative, and positive controls, respectively.

Absorbance values that are lower than the control cells indicate a reduction in the rate of cell proliferation. Conversely, a higher absorbance rate indicates an increase in cell proliferation.

A.12 Imaging of collagen and elastin in spheroids

1. Transfer carefully generated spheroids on the 8-chamber cover glass Lab-Tek slide in a dedicated culture medium without phenol red.
2. Add Col-F (Immunochemistry Technologies, USA) to a final concentration of 10 μM in the cell culture medium. Incubate for 1 h at 37 °C.
3. Wash the samples three times with prewarmed PBS.
4. Add Hoechst 33342 to a final concentration of 15 μM. Incubate for 2 h at 37 °C.
5. Image the samples. Excitation of Hoechst 33342 is done using a 408 nm laser, while the excitation of Col-F is done using a 488 nm laser. Collect the fluorescence at the range of 425–475 nm (Hoechst 33342) and 500–550 nm (Col-F).

References

[1] Zeneng Wang et al. “Gut flora metabolism of phosphatidylcholine promotes cardiovascular disease”. In: *Nature* 472.7341 (2011), pp. 57–65.

[2] W.H. Wilson Tang et al. “Intestinal Microbial Metabolism of Phosphatidylcholine and Cardiovascular Risk”. In: *New England Journal of Medicine* 368.17 (2013), pp. 1575–1584.

[3] M. Trøseid et al. “Microbiota-dependent metabolite trimethylamine-N-oxide is associated with disease severity and survival of patients with chronic heart failure”. In: *Journal of Internal Medicine* 277.6 (2015), pp. 717–726.

[4] W. H.Wilson Tang et al. “Intestinal microbiota-dependent phosphatidylcholine metabolites, diastolic dysfunction, and adverse clinical outcomes in chronic systolic heart failure”. In: *Journal of Cardiac Failure* 21.2 (2015), pp. 91–96.

[5] K. Jaworska et al. “TMA, a forgotten uremic toxin, but not TMAO, is involved in cardiovascular pathology”. In: *Toxins* 11.9 (2019).

[6] Maddaly Ravi et al. “3D cell culture systems: Advantages and applications”. In: *Journal of Cellular Physiology* 230.1 (2015), pp. 16–26.

[7] X. Cui, Y. Hartanto, and H. Zhang. “Advances in multicellular spheroids formation”. In: *Journal of the Royal Society Interface* 14.127 (2017).

[8] Karina Kwapiszewska et al. “Nanoscale Viscosity of Cytoplasm Is Conserved in Human Cell Lines”. In: *Journal of Physical Chemistry Letters* 11.16 (2020), pp. 6914–6920.

[9] Paolo A. Netti et al. “Role of extracellular matrix assembly in interstitial transport in solid tumors”. In: *Cancer Research* 60.9 (2000), pp. 2497–2503.

[10] M. Pilz et al. “Transport of nanoprobes in multicellular spheroids”. In: *Nanoscale* 12.38 (2020).

[11] Jeff W. Lichtman and Conchello José-Angel. “Fluorescence microscopy”. In: *Nature Methods* 2.12 (2005), pp. 910–919.

[12] Joseph R. Lakowicz. *Principles of Fluorescence Spectroscopy.* 3rd ed. Springer, 2006.

[13] Kapusta P., Wahl M., and Erdmann R. *Advanced Photon Counting. Applications, Methods, Instrumentation.* 1st ed. Springer, 2015.

[14] Ulrich Kubitscheck. *Fluorescence Microscopy. From Principles to Biological Applications.* 1st ed. Wiley-Blackwell, 2013.

[15] Stephen W. Paddock, Thomas J. Fellers, and Michael W. Davidson. *Introductory Confocal Concepts.* URL: `https://www.microscopyu.com/techniques/confocal/introductory-confocal-concepts` (visited on 04/22/2021).

[16] Enderlein J. “Fluorescence correlation spectroscopy (IUPAC Technical Report)”. In: *Pure and Applied Chemistry* 85.5 (2013), pp. 999–1016.

[17] Kwapiszewska K. et al. “Determination of oligomerization state of Drp1 protein in living cells at nanomolar concentrations”. In: *Scientific Reports* 9.1 (2019), pp. 1–9.

[18] A. Giudice et al. “High-rate photon counting and picosecond timing with silicon-SPAD based compact detector modules”. In: *Journal of Modern Optics* 2-3 (), pp. 225–237.

[19] Sally A. Kim, Katrin G. Heinze, and Petra Schwille. “Fluorescence correlation spectroscopy in living cells”. In: *Nature Methods* 4.11 (2007), pp. 963–973.

[20] Jonas Ries and Petra Schwille. “Fluorescence correlation spectroscopy”. In: *BioEssays* 34.5 (2012), pp. 361–368.

[21] A. Einstein. “Über die von der molekularkinetischen Theorie der Wärme geforderte Bewegung von in ruhenden Flüssigkeiten suspendierten Teilchen”. In: *Annalen der Physik* 17 (1905), pp. 549–560.

[22] Petra Schwille. “Fluorescence Correlation Spectroscopy and Its Potential for Intracellular Applications”. In: *Cell Biochemistry and Biophysics* 34 (2001), pp. 383–408.

[23] Radek Macháň and Thorsten Wohland. “Recent applications of fluorescence correlation spectroscopy in live systems”. In: *FEBS Letters* 588.19 (2014), pp. 3571–3584.

[24] Krishnananda Chattopadhyay et al. “Measurement of microsecond dynamic motion in the intestinal fatty acid binding protein by using fluorescence correlation spectroscopy”. In: *Proceedings of the National Academy of Sciences of the United States of America* 99.22 (2002), pp. 14171–14176.

[25] Krishnananda Chattopadhyay et al. “Measuring unfolding of proteins in the presence of denaturant using fluorescence correlation spectroscopy”. In: *Biophysical Journal* 88.2 (2005), pp. 1413–1422.

[26] Ranendu Ghosh, Sunny Sharma, and Krishnananda Chattopadhyay. “Effect of arginine on protein aggregation studied by fluorescence correlation spectroscopy and other biophysical methods”. In: *Biochemistry* 48.5 (2009), pp. 1135–1143.

[27] N. O. Petersen. “Diffusion and aggregation in biological membranes”. In: *Canadian Journal of Biochemistry and Cell Biology* 62.11 (1984), pp. 1158–1166.

[28] Grzegorz Bubak et al. “Quantifying Nanoscale Viscosity and Structures of Living Cells Nucleus from Mobility Measurements”. In: *Journal of Physical Chemistry Letters* 12.1 (2021), pp. 294–301.

[29] Allison Paradise et al. “Significant Proportions of Nuclear Transport Proteins with Reduced Intracellular Mobilities Resolved by Fluorescence Correlation Spectroscopy”. In: *Journal of Molecular Biology* 365.1 (2007), pp. 50–65.

[30] E. L. Elson. “Fluorescence correlation spectroscopy measures molecular transport in cells”. In: 2.11 (2001), pp. 789–796.

[31] Jörg Enderlein et al. “Performance of fluorescence correlation spectroscopy for measuring diffusion and concentration”. In: *ChemPhysChem* 6.11 (2005), pp. 2324–2336.

[32] Jonas Ries et al. “Automated suppression of sample-related artifacts in Fluorescence Correlation Spectroscopy”. In: *Optics Express* 18.11 (2010), p. 11073.

[33] Jeong I. Lee et al. “Measurement of diffusion in articular cartilage using fluorescence correlation spectroscopy”. In: *BMC Biotechnology* 11 (2011).

[34] A. Michelman-Ribeiro et al. “Structural Changes in Polymer Gels Probed by Fluorescence Correlation Spectroscopy”. In: *Macromolecules* 37 (2004), pp. 10212–10214.

[35] R. Briandet et al. “Fluorescence correlation spectroscopy to study diffusion and reaction of bacteriophages inside biofilms”. In: *Applied and Environmental Microbiology* 74.7 (2008), pp. 2135–2143.

[36] Silviya Zustiak et al. “Effects of multiple scattering on fluorescence correlation spectroscopy measurements of particles moving within optically dense media”. In: *Journal of Biomedical Optics* 17.12 (2012), p. 125004.

[37] Charles-Edouard Leroux et al. “Fluorescent correlation spectroscopy measurements with adaptive optics in the intercellular space of spheroids”. In: *Biomedical Optics Express* 5.10 (2014), p. 3730.

[38] Ashok Pabbathi, Satyajit Patra, and Anunay Samanta. “Structural transformation of bovine serum albumin induced by dimethyl sulfoxide and probed by fluorescence correlation spectroscopy and additional methods”. In: *ChemPhysChem* 14.11 (2013), pp. 2441–2449.

[39] Eilon Sherman et al. “Using fluorescence correlation spectroscopy to study conformational changes in denatured proteins”. In: *Biophysical Journal* 94.12 (2008), pp. 4819–4827.

[40] J. Mark Brown and Stanley L. Hazen. “Microbial modulation of cardiovascular disease”. In: *Nature Reviews Microbiology* 16.3 (2018), pp. 171–181.

[41] Manuel T. Velasquez et al. “Trimethylamine N-oxide: The good, the bad and the unknown”. In: *Toxins* 8.11 (2016).

[42] Thomas C. Gluick and Sushma Yadav. “Trimethylamine N-oxide stabilizes RNA tertiary structure and attenuates the denaturating effects of urea”. In: *Journal of the American Chemical Society* 125.15 (2003), pp. 4418–4419.

[43] Prashant N. Jethva and Jayant B. Udgaonkar. “The Osmolyte TMAO Modulates Protein Folding Cooperativity by Altering Global Protein Stability”. In: *Biochemistry* 57.40 (2018), pp. 5851–5863.

[44] Marcin Ufnal, Anna Zadlo, and Ryszard Ostaszewski. “TMAO: A small molecule of great expectations”. In: *Nutrition* 31.11-12 (2015), pp. 1317–1323.

[45] Marta Gawrys-Kopczynska et al. “TMAO, a seafood-derived molecule, produces diuresis and reduces mortality in heart failure rats”. In: *eLife* 9 (2020), pp. 1–31.

[46] Vera A. Borzova et al. “Kinetics of thermal denaturation and aggregation of bovine serum albumin”. In: *PLoS ONE* 11.4 (2016), pp. 1–29.

[47] Roy M. Daniel, Mark Dines, and Helen H. Petach. “The denaturation and degradation of stable enzymes at high temperatures”. In: *Biochemical Journal* 317.1 (1996), pp. 1–11.

[48] Myron L. Wagner and Harold A. Scheraga. “Gouy diffusion studies of bovine serum albumin”. In: *Journal of Physical Chemistry* 60.8 (1956), pp. 1066–1076.

[49] Pawel J. Zuk, Bogdan Cichocki, and Piotr Szymczak. “GRPY: An Accurate Bead Method for Calculation of Hydrodynamic Properties of Rigid Biomacromolecules”. In: *Biophysical Journal* 115.5 (2018), pp. 782–800.

[50] Anna Michnik et al. “Comparative DSC study of human and bovine serum albumin”. In: *Journal of Thermal Analysis and Calorimetry* 84.1 (2006), pp. 113–117.

[51] Deborah K. Wilkins et al. “Hydrodynamic radii of native and denatured proteins measured by pulse field gradient NMR techniques”. In: *Biochemistry* 38.50 (1999), pp. 16424–16431.

[52] Daniel C. Carter et al. “Three-dimensional structure of human serum albumin”. In: *Science* 244.4909 (1989), pp. 1195–1198.

[53] Christine Blancher and Adam Jones. “SDS -PAGE and Western Blotting Techniques”. In: *Metastasis Research Protocols: Volume I: Analysis of Cells and Tissues*. Ed. by Susan A. Brooks and Udo Schumacher. Totowa, NJ: Humana Press, 2001, pp. 145–162.

[54] Joanne M. Manns. “SDS-polyacrylamide gel electrophoresis (SDS-PAGE) of proteins”. In: *Current Protocols in Microbiology* SUPPL. 22 (2011), pp. 1–13.

[55] A. A. Sadeghi et al. “Protein degradation kinetics of untreated and treated soybean meal using SDS-PAGE”. In: *Animal Feed Science and Technology* 126.1-2 (2006), pp. 121–133.

[56] Warner Robert C. “the Alkaline Hydrolysis of Egg Albumin”. In: *Journal of Biological Chemistry* 142.2 (1942), pp. 741–756.

[57] P. M. Nottingham. “The alkaline hydrolysis of haddock actomyosin. I. —Ammonia formation”. In: *Journal of the Science of Food and Agriculture* 6.2 (1955), pp. 82–86.

[58] Smith R. M. and Hansen D. E. “The pH-Rate Profile for the Hydrolysis of a Peptide Bond”. In: *Journal of the American Chemical Society* 120 (1998), pp. 8910–8913.

[59] E. Tarelli and P. H. Corran. “Ammonia cleaves polypeptides at asparagine proline bonds”. In: *Journal of Peptide Research* 62.6 (2003), pp. 245–251.

[60] A. Dugaiczyk, S. W. Law, and O. E. Dennison. “Nucleotide sequence and the encoded amino acids of human serum albumin mRNA”. In: *Proceedings of the National Academy of Sciences of the United States of America* 79.1 (1982), pp. 71–75.

[61] Charles J. Chamberlain. “Comparative Morphology of Cytoplasm and Chromatin”. In: *Botanical Gazette* 80.2 (1925), pp. 203–212.

[62] F H C Crick and A F W Hughes. “Physical properties of cytoplasm. A study by means of the magnetic particle method”. In: *Experimental cell research* 1 (1949), pp. 37–80.

[63] Pollard Thomas D. et al. *Cell Biology*. 3rd ed. Elsevier, 2017.

[64] J. Marx. “Organizing the cytoplasm:An intricate, interconnected array of filaments in the cytoplasm gives this part of the cell more order and complexity than was once thought”. In: *Science* 222.4628 (1983), pp. 1109–1111.

[65] Tianyu Liu et al. “Quantitatively mapping cellular viscosity with detailed organelle information via a designed PET fluorescent probe”. In: *Scientific Reports* 4 (2014), pp. 1–7.

[66] Martijn Tros et al. “Picosecond orientational dynamics of water in living cells”. In: *Nature Communications* 8.1 (2017), pp. 1–7.

[67] Tomasz Kalwarczyk et al. “Comparitive Analysis of viscosity of complex fliquids and cytoplasm of mammalian cell at the nanoscale”. In: (2011), pp. 2157–2163.

[68] Krzysztof Szczepański, Karina Kwapiszewska, and Robert Hołyst. “Stability of cytoplasmic nanoviscosity during cell cycle of HeLa cells synchronized with Aphidicolin”. In: *Scientific Reports* 9.1 (2019), pp. 1–8.

[69] Evan Ingersoll and Gael McGill. *Cellular landscape.* URL: `https://gaelmcgill.artstation.com/projects/Pm0JL1` (visited on 05/20/2021).

[70] Carolina Pontes Soares et al. “2D and 3D-organized cardiac cells shows differences in cellular morphology, adhesion junctions, presence of myofibrils and protein expression”. In: *PLoS ONE* 7.5 (2012).

[71] John M. Davis. *Animal Cell Culture. Essential Methods.* 1st ed. Wiley-Blackwell, 2011.

[72] Marta Kapałczyńska et al. “2D and 3D cell cultures – a comparison of different”. In: *Archives of Medical Science* 14.4 (2016), pp. 910–919.

[73] Eleanor Knight and Stefan Przyborski. “Advances in 3D cell culture technologies enabling tissue-like structures to be created in vitro”. In: *Journal of Anatomy* 227.6 (2015), pp. 746–756.

[74] Tao Sun et al. “Culture of skin cells in 3D rather than 2D improves their ability to survive exposure to cytotoxic agents”. In: *Journal of Biotechnology* 122.3 (2006), pp. 372–381.

[75] Eelco Fennema et al. “Spheroid culture as a tool for creating 3D complex tissues”. In: *Trends in Biotechnology* 31.2 (2013), pp. 108–115.

[76] Kamila Białkowska et al. “Spheroids as a type of three-dimensional cell cultures—examples of methods of preparation and the most important application”. In: *International Journal of Molecular Sciences* 21.17 (2020), pp. 1–17.

[77] Leoni A. Kunz-Schughart, Marina Kreutz, and Ruth Knuechel. “Multicellular spheroids: A three-dimensional in vitro culture system to study tumour biology”. In: *International Journal of Experimental Pathology* 79.1 (1998), pp. 1–23.

[78] Ana S. Nunes et al. “3D tumor spheroids as in vitro models to mimic in vivo human solid tumors resistance to therapeutic drugs”. In: *Biotechnology and Bioengineering* 116.1 (2019), pp. 206–226.

[79] Ruei Zhen Lin and Hwan You Chang. “Recent advances in three-dimensional multicellular spheroid culture for biomedical research”. In: *Biotechnology Journal* 3.9-10 (2008), pp. 1172–1184.

[80] X. Cui, Y. Hartanto, and H. Zhang. “Advances in multicellular spheroids formation”. In: *Journal of the Royal Society Interface* 14.127 (2017).

[81] Toni-Marie Achilli, Julia Meyer, and Jeffrey R Morgan. "Advances in the formation, use and understanding of multicellular spheroids". In: *Expert Opinion on Biological Therapy* 12.10 (2012), pp. 1347–1360.

[82] Ruei Zeng Lin et al. "Dynamic analysis of hepatoma spheroid formation: Roles of E-cadherin and β1-integrin". In: *Cell and Tissue Research* 324.3 (2006), pp. 411–422.

[83] Anthony P. Napolitano et al. "Dynamics of the self-assembly of complex cellular aggregates on micromolded nonadhesive hydrogels". In: *Tissue Engineering* 13.8 (2007), pp. 2087–2094.

[84] George Poste, Demetrios Papahadjopoulos, and William J. Vail. "Lipid Vesicles as Carriers for Introducing Biologically Active Materials into Cells". In: *Methods in Cell Biology* 14.C (1976), pp. 33–71.

[85] Craig Y. Okada and Martin Rechsteiner. "Introduction of macromolecules into cultured mammalian cells by osmotic lysis of pinocytic vesicles". In: *Cell* 29.1 (1982), pp. 33–41.

[86] Tomasz Kalwarczyk et al. "Apparent Anomalous Diffusion in the Cytoplasm of Human Cells: The Effect of Probes' Polydispersity". In: *Journal of Physical Chemistry B* 121.42 (2017), pp. 9831–9837.

[87] Kubo R. "The fluctuation-dissipation theorem". In: *Reports on Progress in Physics* 255 (1966).

[88] Tomasz Kalwarczyk et al. "Motion of nanoprobes in complex liquids within the framework of the length-scale dependent viscosity model". In: *Advances in Colloid and Interface Science* 223 (2015), pp. 55–63.

[89] Mark J Dayel, Erik F Y Hom, and A S Verkman. "Diffusion of Green Fluorescent Protein in the Aqueous-Phase Lumen of Endoplasmic Reticulum". In: *Biophysical Journal* 76 (1999), pp. 2843–2851.

[90] Kateryna Kon. *Structure of a microtubule, illustration.* URL: `https://www.sciencephoto.com/media/887510/view` (visited on 05/27/2021).

[91] Inc. Blausen Medical Communications. *3D rendering of endoplasmic reticulum.* URL: `https://en.wikiversity.org/wiki/WikiJournal_of_Medicine/Medical_gallery_of_Blausen_Medical_2014` (visited on 05/27/2021).

[92] Katherine A. Lyseng-Williamson and Caroline Fenton. "Docetaxel. A Review of its Use in Metastatic Breast Cancer." In: *Drugs* 65 (2005), pp. 2513–2531.

[93] Gia K. Voeltz, Melissa M. Rolls, and Tom A. Rapoport. “Structural organization of the endoplasmic reticulum”. In: *EMBO Reports* 3.10 (2002), pp. 944–950.

[94] Hui Li et al. “Mapping intracellular diffusion distribution using single quantum dot tracking: Compartmentalized diffusion defined by endoplasmic reticulum”. In: *Journal of the American Chemical Society* 137.1 (2015), pp. 436–444.

[95] Philip R. LeDuc and Robert M. Bellin. “Nanoscale intracellular organization and functional architecture mediating cellular behavior”. In: *Annals of Biomedical Engineering* 34.1 (2006), pp. 102–113.

[96] Young Eun Kim et al. “Quantitative Proteomic Analysis of 2D and 3D Cultured Colorectal Cancer Cells: Profiling of Tankyrase Inhibitor XAV939-Induced Proteome”. In: *Scientific Reports* 8.1 (2018), pp. 1–12.

[97] Hari R. Kumar et al. “Three-dimensional neuroblastoma cell culture: Proteomic analysis between monolayer and multicellular tumor spheroids”. In: *Pediatric Surgery International* 24.11 (2008), pp. 1229–1234.

[98] Mohammad R. Abedini et al. “Cell fate regulation by gelsolin in human gynecologic cancers”. In: *Proceedings of the National Academy of Sciences of the United States of America* 111.49 (2014), p. 17684.

[99] Jaya Aseervatham. “Cytoskeletal remodeling in cancer”. In: *Biology* 9.11 (2020), pp. 1–40.

[100] Jacob O. Spiegel, Bennett Van Houten, and Jacob D. Durrant. “PARP1: Structural insights and pharmacological targets for inhibition”. In: *DNA Repair* 103 (2021), p. 103125.

[101] Mark Robson et al. “ Olaparib for Metastatic Breast Cancer in Patients with a Germline BRCA Mutation ”. In: *New England Journal of Medicine* 377.6 (2017), pp. 523–533.

[102] M. William Audeh et al. “Oral poly(ADP-ribose) polymerase inhibitor olaparib in patients with BRCA1 or BRCA2 mutations and recurrent ovarian cancer: A proof-of-concept trial”. In: *The Lancet* 376.9737 (2010), pp. 245–251.

[103] *Olaparib, Mechanism of Action.* URL: `https://www.pharmacodia.com/yaodu/html/v1/chemicals/a0205b87490c847182672e8d371e9948.html` (visited on 06/04/2021).

[104] Christopher P. Irwin et al. “PARPi-FL - A Fluorescent PARP1 Inhibitor for Glioblastoma Imaging”. In: *Neoplasia (United States)* 16.5 (2014), pp. 432–440.

[105] Patrick Poulin and Frank Peter Theil. “A priori prediction of tissue: Plasma partition coefficients of drugs to facilitate the use of physiologically-based pharmacokinetic models in drug discovery”. In: *Journal of Pharmaceutical Sciences* 89.1 (2000), pp. 16–35.

[106] Patrick Poulin and Kannan Krishnan. “Molecular Structure-Based Prediction of the Partition Coefficients of Organic Chemicals for Physiological Pharmacokinetic Models”. In: *Toxicology Methods* 6.3 (1996), pp. 117–137.

[107] Sascha Kopp et al. “The role of NFκB in spheroid formation of human breast cancer cells cultured on the Random Positioning Machine”. In: *Scientific Reports* 8.1 (2018), pp. 1–17.

[108] T. Zaremba et al. “Poly(ADP-ribose) polymerase-1 polymorphisms, expression and activity in selected human tumour cell lines”. In: *British Journal of Cancer* 101.2 (2009), pp. 256–262.

[109] Ashley M. Laughney et al. “Single-cell pharmacokinetic imaging reveals a therapeutic strategy to overcome drug resistance to the microtubule inhibitor eribulin”. In: *Science Translational Medicine* 6.261 (2014), pp. 1–12.

[110] Ashley M. Laughney et al. “Single-cell pharmacokinetic imaging reveals a therapeutic strategy to overcome drug resistance to the microtubule inhibitor eribulin”. In: *Science Translational Medicine* 6.261 (2014), pp. 1–12.

[111] Seong Hoon Jang et al. “Drug delivery and transport to solid tumors”. In: *Pharmaceutical Research* 20.9 (2003), pp. 1337–1350.

[112] Alain Pluen et al. “Role of tumor-host interactions in interstitial diffusion of macromolecules: Cranial vs. subcutaneous tumors”. In: *Proceedings of the National Academy of Sciences of the United States of America* 98.8 (2001), pp. 4628–4633.

[113] Andrew W. Holle, Jennifer L. Young, and Joachim P. Spatz. “In vitro cancer cell-ECM interactions inform in vivo cancer treatment”. In: *Advanced Drug Delivery Reviews* 97 (2016), pp. 270–279.

[114] Rakesh K. Jain. “Transport of Molecules in the Tumor Interstitium: A Review”. In: *Cancer Research* 47.12 (1987), pp. 3039–3051.

[115] Rakesh K. Jain. "Barriers to drug delivery in solid tumors". In: *Scientific American* 271 (1994), pp. 58–65.

[116] Achilleas D. Theocharis et al. "Extracellular matrix structure". In: *Advanced Drug Delivery Reviews* 97 (2016), pp. 4–27.

[117] Richard O Hynes. "The Extracellular Matrix: Not Just Pretty Fibrils". In: *Science* 326.5957 (2009), pp. 1216–1219.

[118] Elizabeth D. Hay. *Cell Biology of Extracellular Matrix.* 2nd ed. Springer, 1991.

[119] D. A. Rees Struther Arnott and E. R. Morris. *Molecular Biophysics of the Extracellular Matrix.* 1st ed. Humana Press, 1984.

[120] Matthew D. Shoulders and Ronald T. Raines. "Collagen structure and stability". In: *Annual Review of Biochemistry* 78 (2009), pp. 929–958.

[121] Lawrence B. Sandberg, Norman T. Soskel, and John G. Leslie. "Elastin Structure, Biosynthesis, and Relation to Disease States". In: *New England Journal of Medicine* 304.10 (1981), pp. 566–579.

[122] V. Shenoy and J. Rosenblatt. "Diffusion of Macromolecules in Collagen and Hyaluronic Acid, Rigid-Rod-Flexible Polymer, Composite Matrices". In: *Macromolecules* 28.26 (1995), pp. 8751–8758.

[123] Paolo A. Netti et al. "Role of extracellular matrix assembly in interstitial transport in solid tumors". In: *Cancer Research* 60.9 (2000), pp. 2497–2503.

[124] Toshiro Kobori et al. "Biopolymers Volume 85 / Number 4 295". In: *Biopolymers* 85.4 (2007), pp. 392–406.

[125] Saroja Ramanujan et al. "Diffusion and convection in collagen gels: Implications for transport in the tumor interstitium". In: *Biophysical Journal* 83.3 (2002), pp. 1650–1660.

[126] Takanori Kihara, Junri Ito, and Jun Miyake. "Measurement of biomolecular diffusion in extracellular matrix condensed by fibroblasts using fluorescence correlation spectroscopy". In: *PLoS ONE* 8.11 (2013).

[127] Marine Le Goas et al. "How Do Surface Properties of Nanoparticles Influence Their Diffusion in the Extracellular Matrix? A Model Study in Matrigel Using Polymer-Grafted Nanoparticles". In: *Langmuir* 36.35 (2020), pp. 10460–10470.

[128] Gabriel Benton et al. “Matrigel: From discovery and ECM mimicry to assays and models for cancer research”. In: *Advanced Drug Delivery Reviews* 79 (2014), pp. 3–18.

[129] Thore Nederman et al. “Demonstration of an Extracellular Matrix in Multicellular Tumor Spheroids”. In: *Cancer Research* 44.7 (1984), pp. 3090–3097.

[130] Gerhard Hamilton. “Multicellular spheroids as an in vitro tumor model”. In: *Cancer Letters* 131.1 (1998), pp. 29–34.

[131] Nina Kristine Reitan et al. “Macromolecular diffusion in the extracellular matrix measured by fluorescence correlation spectroscopy”. In: *Journal of Biomedical Optics* 13 (2008), p. 054040.

[132] Ian A. Cree. *Cancer Cell Culture. Methods and Protocols.* 2nd ed. Humana Press, 2011.

[133] M. Gale et al. “Sequential assembly of collagen revealed by atomic force microscopy”. In: *Biophysical Journal* 68.5 (1995), pp. 2124–2128.

[134] A. H. Baker et al. “Inhibition of invasion and induction of apoptotic cell death of cancer cell lines by overexpression of TIMP-3”. In: *British Journal of Cancer* 79.9-10 (1999), pp. 1347–1355.

[135] W. Van De Sande and A. Persoons. “The size and shape of macromolecular structures: Determination of the radius, the length, and the persistence length of rodlike micelles of dodecyldimethylammonium chloride and bromide”. In: *Journal of Physical Chemistry* 89.3 (1985), pp. 404–406.

[136] M. Gale et al. “Sequential assembly of collagen revealed by atomic force microscopy”. In: *Biophysical Journal* 68.5 (1995), pp. 2124–2128.

[137] Ewa Biela et al. “Col-F, a fluorescent probe for ex vivo confocal imaging of collagen and elastin in animal tissues”. In: *Cytometry Part A* 83 A.6 (2013), pp. 533–539.

[138] R. O. Hynes et al. “Cell surface fibronectin and oncogenic transformation.” In: *Journal of supramolecular structure* 11.1 (1979), pp. 95–104.

[139] W. W. Kao, D. J. Prockop, and R. A. Berg. “Kinetics for the secretion of nonhelical procollagen by freshly isolated tendon cells.” In: *Journal of Biological Chemistry* 254.7 (1979), pp. 2234–2243.

[140] Bo Zhang et al. “Targeting fibronectins of glioma extracellular matrix by CLT1 peptide-conjugated nanoparticles”. In: *Biomaterials* 35.13 (2014), pp. 4088–4098.

[141] Andrew W. Holle, Jennifer L. Young, and Joachim P. Spatz. “In vitro cancer cell-ECM interactions inform in vivo cancer treatment”. In: *Advanced Drug Delivery Reviews* 97 (2016), pp. 270–279.

[142] René Raavé, Toin H. van Kuppevelt, and Willeke F. Daamen. “Chemotherapeutic drug delivery by tumoral extracellular matrix targeting”. In: *Journal of Controlled Release* 274.January (2018), pp. 1–8.

[143] Thomas T Goodman, Peggy L Olive, and Suzie H Pun. “Increased nanoparticle penetration in collagenase-treated multicellular spheroids.” In: *International journal of nanomedicine* 2.2 (2007), pp. 265–74.

[144] Wen Zhang et al. “Decorin is a pivotal effector in the extracellular matrix and tumour microenvironment”. In: *Oncotarget* 9.4 (2018), pp. 5480–5491.

[145] Yasuhiro Miki et al. “The advantages of co-culture over mono cell culture in simulating in vivo environment”. In: *Journal of Steroid Biochemistry and Molecular Biology* 131.3-5 (2012), pp. 68–75.

[146] Takehito Sasaki et al. “Development of Multicellular Spheroids of HeLa Cells Cocultured with Fibroblasts and Their Response to X-lrradiation”. In: *Cancer Research* 44.1 (1984), pp. 345–351.

[147] Oliver Ingo Hoffmann et al. “Impact of the spheroid model complexity on drug response”. In: *Journal of Biotechnology* 205 (2015), pp. 14–23.

[148] Roman Akasov et al. “3D in vitro co-culture models based on normal cells and tumor spheroids formed by cyclic RGD-peptide induced cell self-assembly”. In: *Biotechnology Letters* 39.1 (2017), pp. 45–53.

[149] Van Thuy Hoang et al. “Optical properties of buffers and cell culture media for optofluidic and sensing applications”. In: *Applied Sciences (Switzerland)* 9.6 (2019), pp. 1–11.

[150] *Recommended Procedures for Labeling.* Application Note. ATTO-TEC GmbH.

[151] *Zeba™ Spin Desalting Columns.* Application Note. Thermo Scientific.

[152] *Influx™ Pinocytic Cell-Loading Reagent.* Application Note. Molecular Probes, Inc.

[153] Constance Oliver and Maria Célia Jamur. *Immunocytochemical Methods and Protocols.* 3rd ed. Humana Press, 2010.

IChF
Institute of Physical Chemistry PAS

Cover design: Tomasz Kalwarczyk, Marta Pilz